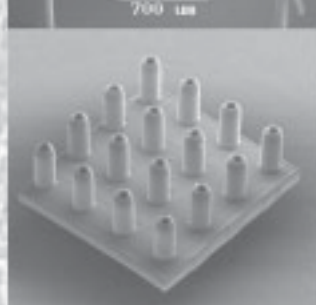
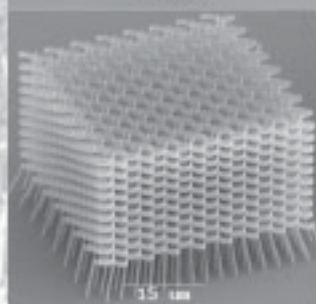
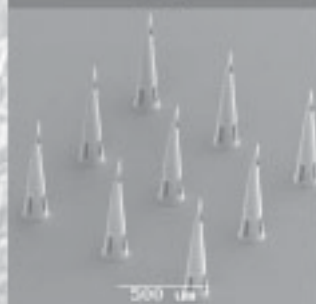
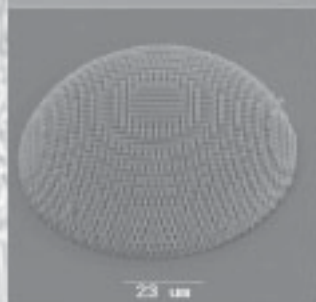


Aleksandr Ovsianikov

Investigation of Two-Photon Polymerization Technique for Applications in Photonics and Biomedicine



HANNOVER  **CHAPEL HILL**  **HERAKLION**

Investigation of Two-Photon Polymerization Technique for Applications in Photonics and Biomedicine

Von der Fakultät für Mathematik und Physik der Gottfried Wilhelm Leibniz Universität
Hannover
zur Erlangung des Grades eines

Doktors der Naturwissenschaften
- Dr. rer. nat. -

genehmigte Dissertation
von

Dipl.-Phys. Aleksandr Ovsianikov
geboren am 12. Oktober 1978, in Klaipeda (Litauen)

Bibliografische Information der Deutschen Nationalbibliothek

Die Deutsche Nationalbibliothek verzeichnet diese Publikation in der Deutschen Nationalbibliografie; detaillierte bibliografische Daten sind im Internet über <http://dnb.ddb.de> abrufbar.

1. Aufl. - Göttingen : Cuvillier, 2009

Zugl.: Hannover, Univ., Diss., 2008

978-3-86727-916-1

Referent: Prof. Dr. B. N. Chichkov

Korreferent: Prof. Dr. W. Ertmer

Tag der Promotion: 18. Dezember 2008

© CUVILLIER VERLAG, Göttingen 2009

Nonnenstieg 8, 37075 Göttingen

Telefon: 0551-54724-0

Telefax: 0551-54724-21

www.cuvillier.de

Alle Rechte vorbehalten. Ohne ausdrückliche Genehmigung des Verlages ist es nicht gestattet, das Buch oder Teile daraus auf fotomechanischem Weg (Fotokopie, Mikrokopie) zu vervielfältigen.

1. Auflage, 2009

Gedruckt auf säurefreiem Papier

978-3-86727-916-1

Kurzzusammenfassung

Aleksandr Ovsianikov

Untersuchung zur Zwei-Photonen Polymerisations Technik für Anwendungen in der Photonik und Biomedizintechnik

Ein entscheidender Faktor für Fortschritte in der Nanotechnologie ist die Entwicklung von Nano- und Mikrofabrikationstechniken mit höchster Genauigkeit.

Femtosekundenlasertechnologien, welche auf nichtlinearer Licht-Materie-Wechselwirkung basieren, schaffen die Möglichkeit einer kosteneffizienten Strukturherstellung mit hoher Auflösung sowie herausragender Flexibilität. Diese Technologien sind seitens der Industrie durch die aktuellen Fortschritte in der Entwicklung von industrietauglichen Ultrakurzpuls-Lasersystemen verstärkt in den Fokus gerückt.

Zwei-Photonen Polymerisation (2PP) ist ein neuartiges direktes Laserschreibverfahren welches auf Zweiphotonenabsorption der Laserstrahlung in photosensitiven Materialien beruht. Hierbei wird eine lokal stark eingeschränkte chemische Reaktion durch Mehrphotonenabsorption von Femtosekundenlaserpulsen im Fokus induziert, welche zu einer Modifikation des Materials führt. Dieses kann beispielsweise ein Umwandlungsprozess von flüssigem zu festem Material während der Polymerisation sein. Durch das dreidimensionale (3D) Führen des Laserfokus wird eine Spur modifizierten Materials erzeugt. Im nächsten Schritt wird das nicht modifizierte Material durch ein geeignetes Lösungsmittel entfernt, und die gefertigte Struktur wird sichtbar.

Im Gegensatz zu konventionellen laserbasierten Mikrofabrikationstechniken, die Strukturen via Materialabtrag erzeugen, erlaubt 2PP die Herstellung von komplexen 3D-Strukturen. Eine minimale Auflösung von unter 100nm und die Möglichkeit 3D-Strukturen direkt aus einer CAD-Datei generieren zu können, machen 2PP zu einer einzigartigen Herstellungstechnik. Ein großer Vorteil der 2PP-Technik ist, dass konventionelle UV-Photopolymerisation bereits umfangreich erforscht wurde und in vielen technischen Applikationen eingesetzt wird. Die Vielseitigkeit sowie die große Anzahl verwendbarer Materialien trägt maßgeblich dazu bei, dass es eine Vielzahl unterschiedlicher Anwendungen für diese Technik gibt.

Diese Arbeit präsentiert die Ergebnisse der Entwicklung der fundamentalen 2PP-Technik und die Untersuchung verschiedener Einsatzgebiete dieses Verfahrens. Es wurden kommerziell erhältliche sowie neuartige photosensitive Materialien, die sich durch radikalische Polymerisation verarbeiten lassen, im Hinblick auf die minimale Auflösung, Reproduzierbarkeit und Bearbeitungsgenauigkeit untersucht.

Ein wichtiges Anwendungsgebiet, in dem Hybridmaterialien besondere Vorteile infolge ihrer hohen optischen Qualität aufweisen, ist die mikrooptische Photonik. Mittels 2PP konnten refraktive mikrooptische Elemente mit hoher Präzision hergestellt werden. Die hohe Flexibilität erlaubt schnelle Design-Änderungen einzelner Elemente in unterschiedlichen Variationen. Sie ist damit ein einzigartiges Rapid-Prototyping-Verfahren für die Herstellung von Mikrooptiken.

Ein weiteres Anwendungsgebiet ist die Herstellung dreidimensionaler photonischer Kristalle. Diese periodischen Strukturen werden als optisches Äquivalent zu elektrischen Halbleitern betrachtet. Photonische Kristalle besitzen das Potential, die Informationsübertragung zu revolutionieren, indem sie die Realisierung von rein optischen Schaltkreisen ermöglichen.

Mittels der 2PP-Technik wurden systematische Untersuchungen zur Herstellung von Woodpile- sowie spiralbasierten photonischen Kristallen durchgeführt. Ihre optischen Charakteristika wurden optimiert. Biomedizinische Applikationen von mittels 2PP hergestellten Strukturen stehen im Fokus jüngster Untersuchungen. Im Rahmen dieser Arbeit wurden drei solcher Anwendungen untersucht: die 2PP-Herstellung von Mikrostrukturen für das subkutane Drug Delivery, Mikroimplantate sowie Stützgerüste (Scaffolds) für das Tissue Engineering.

Ein Überblick über die jüngsten Veröffentlichungen im Bereich der 2PP-Technik zeigt, dass diese Methode weltweit von einer steigenden Anzahl wissenschaftlicher Arbeitsgruppen verwendet wird.

Aktuell sind im Verlauf dieser Arbeit fünfzehn Peer-review-Publikationen, zahlreiche Beiträge auf Fachkonferenzen sowie drei Buchkapitel entstanden.

Schlagworte: Nanostrukturierung, Zwei-Photonen Polymerisation, Ultrakurze Laserpulse

Abstract

Aleksandr Ovsianikov

Investigation of Two-Photon Polymerization Technique for Applications in Photonics and Biomedicine

An essential factor for the progress of nanotechnology and its driving power is the development of high fidelity nano- and micro-fabrication techniques. Femtosecond laser technologies based on nonlinear light-matter interactions, provide a possibility of cost-efficient manufacturing with high resolution and unprecedented flexibility. Increased attention to these technologies from industry representatives is stimulated by the recent development of compact turnkey ultrashort-pulse laser systems.

Two-photon polymerization (2PP) is a novel direct laser writing technique based on the two-photon absorption of laser radiation in photosensitive resins. In this approach, the multiphoton absorption of femtosecond laser pulses in the waist of the focused laser beam induces a highly localised chemical reaction leading to a local modification of the material. This can be, for example, polymerization process, transforming a material from liquid into the solid state. By moving the laser focus in 3D the trace of modified material is created. In the next step, the unmodified material is removed by an appropriate developer, and the fabricated structure is revealed.

In contrast to conventional laser microfabrication techniques based on material ablation, two-photon polymerization (2PP) allows the fabrication of true 3D structures in accordance to provided CAD design. A minimal resolution below 100nm, in the age when a 3rd dimension becomes an extremely important criterion for success, makes 2PP a one-of-a-kind technology. The fact that conventional UV photopolymerization is a well-studied subject, having a long industrial application history, provides additional advantages for 2PP microfabrication approach. The versatility of the 2PP technology and the large number of applicable materials contribute to the wide range of applications of this technology which are rapidly growing.

This thesis presents results of work on the development of 2PP technique and exploration of applications of this technique. Commercially available as well as novel photosensitive materials processed via free-radical polymerization are studied with respect to their minimal resolution and microstructuring fidelity by 2PP.

Important application areas, where hybrid materials provide particular advantages due to their high optical quality, are microoptics and photonics. Using 2PP technique, refractive microoptical elements have been fabricated with high precision. The flexibility of 2PP allows fast variation of individual element design and, therefore, provides a unique approach for rapid prototyping of modern microoptics. A soft lithography method, based on UV-micromolding, is demonstrated as a possible high fidelity high throughput technique for replication of a large series of produced microstructures. Another important application of 2PP technique in photonics is fabrication of 3D photonic crystals. Photonic crystals are considered to be the optical equivalent of semiconductors. They have potential to revolutionise information technologies by enabling all-optical circuits. Using 2PP technique, systematic investigations on woodpile and spiral photonic crystal fabrication, and subsequent characterisation of their optical properties has been performed.

Recently, biomedical applications of 2PP technique have been pioneered by our group. Three important directions thoroughly studied and presented in this thesis are application of 2PP fabricated microstructures for transdermal drug delivery, microimplants and as scaffolds for guided cell growth in tissue engineering.

An overview of reports on 2PP indicates that this technique is constantly gaining wider acceptance and popularity among scientists worldwide. To date, work performed in the framework of this thesis has resulted in more than 15 peer reviewed publications, numerous conference contributions and three book chapters.

Key words: Nanostructuring, Two-photon polymerization, ultrashort laser pulses

Thesis Outline

This thesis presents results of work on the development of two-photon polymerization (2PP) technique and exploration of applications of this technique. The following chapters provide some overview of the processes underlying the 2PP microfabrication and present current applications of this technique. Chapter 1 opens with the basic introduction into the two-photon absorption process and describes its characteristics relevant for 2PP microfabrication. It is followed by a comparative discussion on different types of photopolymerization with a focus on light-induced free-radical polymerization. In section 1.3, a detailed description of 2PP technique, its advantages for 3D processing, structural resolution dependencies and limitations are discussed. Section 1.4 describes materials used for 2PP by different scientific groups in the world and discusses their target applications. Also here an introduction to inorganic-organic hybrid materials used by our group at the LZH is given. A literature overview on the current development status and studied application areas of the 2PP technique is the subject of section 1.5. A prominent application area of this technique, and one of the central experimental topics of this thesis, is the fabrication of 3D photonic crystal structures. Section 1.6 is devoted to this intensively studied topic. A basic introduction to 3D photonic crystal concepts and a comparative description of alternative microfabrication approaches applied for their realisation is given here.

Chapter 2 provides insights on the experimental realisation of the 2PP technique, it lists out relevant materials and associated sample processing methods. In addition, details on the chemical synthesis of formulations prepared at the LZH are provided. Finally a method for microstructure replication by UV-micromolding is presented.

Chapter 3 opens with results on fundamental investigations of the 2PP. Such issues as influence of material composition, resolution limits, and material shrinkage are addressed here. Section 2.3 describes application of 2PP for the fabrication of microoptical elements and 3D photonic crystals. It includes results on theoretical investigations on properties of 3D photonic crystals with respect to 2PP microfabrication peculiarities, as well as thorough analysis and characterisation of the 3D photonic crystals obtained experimentally. Finally some realised biomedical applications of 2PP microfabrication are presented. Use of microneedles for transdermal drug delivery is a novel area relying on microstructuring technologies. Fabrication and characterisation of such microneedles with respect to skin penetration and subcutaneous injection is the subject of section 3.3.1. 2PP can be applied for rapid prototyping of patient-specific microimplants. Ossicular replacement prosthesis realised by 2PP and results of characterisation of its mechanical properties as well as *in vitro* implantation are presented in section 3.3.2. The capability of 2PP to fabricate arbitrary 3D structures has a great potential in tissue engineering. Section 3.3.3 discusses results of application of 2PP technique for the fabrication of scaffolds for guided cell proliferation. The final chapter is dedicated to the summary and concluding remarks. Also, an outlook on perspectives of further development of 2PP technique is given here.

List of Abbreviations Used Within This Work

2D, 3D.....	Two- ,Three-dimensional
2PP.....	Two-photon polymerization (2PP)
AOM.....	Acousto-optic modulator
CAD.....	Computer aided design
CAM.....	Computer aided manufacturing
DBTDL.....	Dibutyltin dialurate
DR1.....	Disperse red 1
fcc.....	face-centered-cubic
fct.....	face-centered-tetragonal
fs.....	femtosecond
FTIR.....	Fourier-Transformations-InfraRed-Spectroscopy
ITO.....	Indium tin oxide
MAA.....	Methacrylic acid
MAPTMS.....	Methacryloxypropyltrimethoxysilane
MPA.....	Multiphoton absorption
NA.....	Numerical aperture
NLO.....	Nonlinear optical
PBG.....	Photonic bandgap
PDMS.....	Polydimethylsiloxane
PEG.....	Poly(ethylene glycol)
PI.....	Photoinitiator
SEM.....	Scanning Electron Microscope
TORP.....	Total ossicular replacement prosthesis
TPA.....	Two-photon absorption
UV.....	Ultra violet
voxel.....	volume pixel
ZPO.....	Zirconium n-propoxide
Φ	dielectric filling fraction

Contents

Kurzzusammenfassung	i
Abstract	ii
Thesis Outline	iii
List of Abbreviations Used Within This Work.	iv
1 Introduction	
1.1 Multiphoton Absorption	1
1.2 Principles of Photopolymerization	3
1.3 Two-photon Polymerization (2PP) Technique.	5
1.4 Materials for 2PP Processing.	10
1.5 Current Development Status and Applications of 2PP Technique	15
1.6 Photonic Crystals – Engineering the Propagation of Light.	18
2 Materials and methods	
2.1 Experimental Setup for 2PP Processing	22
2.2 Materials Applied for 2PP Processing.	23
2.3 3D Structure Replication by UV-micromolding	27
3 Results and discussions	
<u>3.1 Investigations of 2PP Process</u>	
3.1.1 Hybrid Organic-Inorganic Materials for 2PP Processing.	31
3.1.2 Shrinkage of Materials Processed by 2PP technique.	34
3.1.3 Structuring of Acrylated Poly(Ethylene Glycol)s with 2PP	38
<u>3.2 Applications of 2PP in Microphotonics</u>	
3.2.1 Fabrication of Microoptical Elements	41
3.2.2 Realisation of 3D Photonic Crystals	
Theoretical Investigations of Properties of 3D Photonic Crystals	45
Results of Experimental Realisation of 3D Photonic Crystals:	52
Fabrication of 3D Photonic Crystals Containing NLO Chromophore	60
Fabrication of Shaped 3D Photonic Crystals	62
<u>3.3 Biomedical applications of 2PP Technique</u>	
3.3.1 Microneedles for Transdermal Drug Delivery	65
3.3.2 Fabrication of Microprosthesis.	71
3.3.3 Scaffolds for Tissue Engineering	75
4 Summary and Outlook	79
References	85
List of own Publications.	95

1 Introduction

1.1 Multiphoton Absorption

Multiphoton absorption (MPA) is a quantum mechanical process, where an atom/molecule absorbs few photons simultaneously and can therefore surmount the energy gap, which is exceeds the energy of a single photon, in a single excitation event [Boy92, She84]. Multiphoton absorption was predicted in 1929 by Maria Göppert-Meyer [MGP29]. Three decades prior to the experimental observation of this process, her work described theoretical model gathering the principles of multiphoton interaction between light and matter. The publications main thesis was that an atom might absorb two or more photons, this way allowing electron transition to states which cannot be acquired by single photon absorption. Furthermore the probability of n -photon absorption is proportional to the n^{th} power of the photon flux density; consequently high photon flux densities are required in order to observe this phenomenon. In fact, MPA was one of the first effects demonstrated with the help of lasers, since intensities much higher than provided by other light sources could be achieved [KG61].

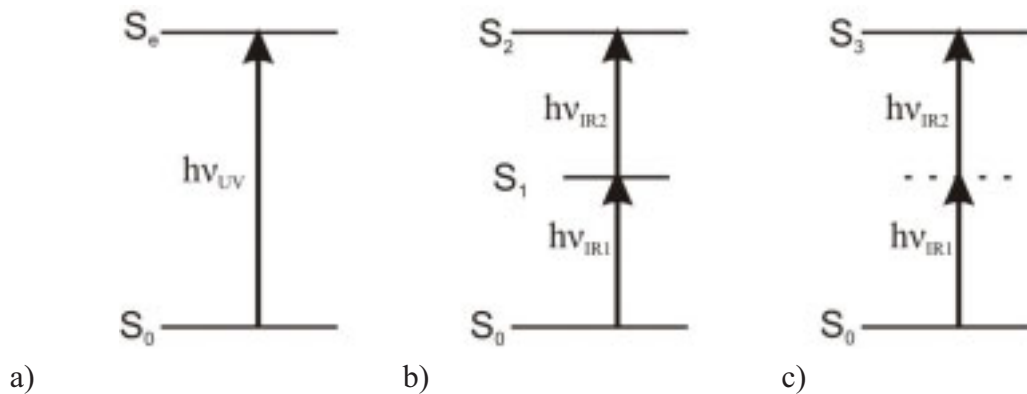


Figure 1.1 Schematic illustration of an atom excitation process with: a) single-photon absorption; b) stepwise absorption of two photons; c) two-photon absorption (TPA).

Figure 1.1 illustrates atom excitation processes through single-photon absorption, stepwise absorption of two photons and two-photon absorption (TPA). In conventional linear absorption process, an atom is excited via single photon absorption process. An excitation of an atom through absorption of single UV photon is illustrated in figure 1.1a. The excited state is characterized by the energy level S_e , the absorption rate scales linearly with the light intensity [Sve98]. An atom can also be excited by absorption of two photons. If a real intermediate state is present, the atom is excited through sequential absorption of photons. After the first photon ($h\nu_{IR1}$) is absorbed, the atom in the excited state can be characterised by a relaxation time or a certain lifetime of the energy level (S_1 in figure 1.1b). Before the decay of this excited state such atom can be promoted to another excited state (S_2 in figure 1.1b) by absorption of a further photon ($h\nu_{IR2}$). Therefore, the absorption of two photons here is

stepwise and is mediated by a “real” energy level. The energies of both photons do not have to be equal and depend on the position of the intermediate level (S_I). The important fact is that the energy level of this intermediate state, and therefore the energy of both photons ($h\nu_{IRI}$ and $h\nu_{IRI}$) are well defined. TPA is in turn mediated by a so called “virtual” state (dashed line in figure 1.1c). TPA is only possible if a second photon is absorbed before the decay of this virtual state. In analogue to sequential absorption, an equivalent description of this process, defining the lifetime of such excited state or virtual energy level, exists. In accordance to Heisenberg’s uncertainty principle a lifetime of such virtual state is on the order of a few femtoseconds (fs), which is very short when compared to lifetime of real energy level. A further important difference here is that the energy level of such excited state is not defined. Therefore any two photons, whose energy sum equals to the gap between the atoms ground and the excited state can participate in the process. In contrast to stepwise absorption of two photons, for TPA process coherence of the incident light is required.

The excited energy levels S_e and S_3 , shown in figure 1a and c are not exactly the same, since the selection rules for single photon and two-photon absorption are different [She84]. This fact implies that MPA can reveal information about transitions not accessible by single photon processes. The first applications of MPA process were as spectroscopic tool, for identifying the energy states which are not linked to the ground state via single photon absorption [HWP63].

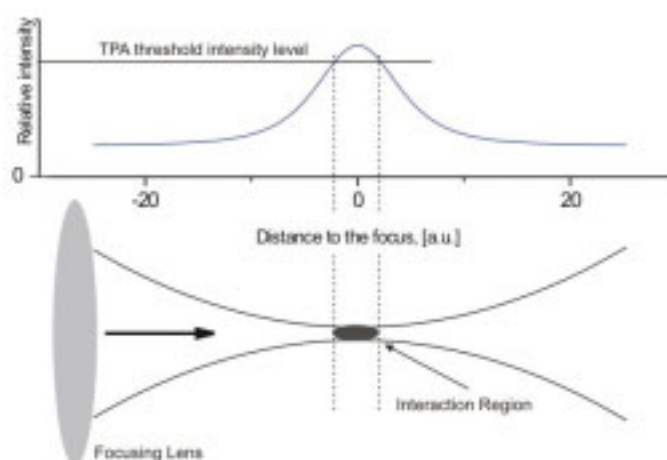


Figure 1.2 Schematic illustration to TPA interaction confinement. Top image shows intensity distribution along a focused laser beam. Lower image shows according interaction TPA region (dark ellipsoid), whose size is defined by the TPA threshold intensity.

Since the probability of the TPA is proportional to the square of the intensity of the laser radiation, favourable conditions for TPA in the first place are created in the waist of the focused laser beam (see figure 1.2). Thus, the multiphoton interaction region is strongly confined. This advantage, widely applied in multi-photon microscopy, leads to high spatial resolution and the ability to selectively excite specific molecules [DSW90]. Using multi-photon microscopy one can, for example, observe the spatial distribution of one specific molecule inside a living cell, and create 3D images with submicrometer resolution. Since the

availability of fs laser systems, multiphoton microscopy gained widespread popularity and currently presents a “must have” tool of any life science laboratory.

1.2 Principles of Photopolymerization

Currently photopolymerization presents an indispensable part of industrial processing for our everyday products. The demand of raw materials for radiation curing in a segment of specialty chemicals market is a constantly growing. Recent findings show that photopolymerization of resins has been applied in mummification procedure in ancient Egypt as early as 1900 BC [BE01]. Nevertheless, the history of modern applications of photopolymerization on the industrial scale is comparatively short. First commercial applications of this technique in coatings started in early 1960s. By the end of 1960s many new material systems, fitting a wide variety of possible industrial applications, were developed. Appropriate equipment allowing fast curing and providing control over the process on the industrial scale was developed. Photopolymerization for industrial applications is very competitive and presents many advantages over many conventional approaches, it allows reducing energy consumption, it is ecological, and finally it is economical due to its high productivity at lower costs. Combination of these factors made photopolymerization a choice of process for evermore new applications areas in the industry throughout the years, this growth continues to present days.

In mid 1980s knowledge gained in this field and its wide acceptance in the industry paved way for rapid prototyping technologies based photopolymerization. Stereolithography, also known as 3D printing, solid free-form fabrication or solid imaging, is a technique allowing to create complex 3D models from photosensitive materials in accordance to provided CAD design. Since this method is very economic for prototype manufacturing it is now widely applied in automotive, aerospace, and many other major industries. By looking at the history and fields of application of radiation-curing it becomes clear that the main driving force is its high potential for innovation.

In general, polymerization is defined as a process of reacting monomer molecules together in a chemical reaction to form three-dimensional networks or polymer chains [You87]. In case of photopolymerization this process is initiated by light. Most often addition polymerization is meant when talking about photopolymerization. Here, photopolymerization is defined as the light-induced chemical reaction of monomers or oligomers that results in a solid polymeric network [Dec94]. Modern materials systems for photopolymerization contain at least two main components a photoinitiator and a monomer or an oligomer. Apart from that, additives, whose function is to impart desired material properties, are often used. Photoinitiators - molecules which have low photo dissociation energy – are added in order to increase the material photosensitivity and so to improve the efficiency of the process.

Photopolymerization reactions that form a cross-linked network follow the characteristic steps of any chain polymerization mechanism: photoinitiation, propagation and termination. Figure 1.3 provides a detailed illustration of a free-radical photopolymerization

reaction on the example of methacryloxypropyltrimethoxysilane (MAPTMS) and photoinitiator 2-benzyl-2-dimethylamino-4'-morpholinobutyro-phenone (Irgacure 369). In the first step, two free-radicals are produced through light-induced bond cleavage in the photoinitiator molecule (photolysis), as a result of absorption of a UV photon (figure 1.3a). By definition radicals are atomic or molecular species having unpaired electrons on an otherwise open shell configuration, and therefore exhibiting extremely high reactivity [Dec98]. When produced radical comes into close proximity with an oligomer molecule (MAPTMS in this case) they can react by breaking a methacrylic bond (an arrow in figure 1.3b indicates which bond radical is able to break). As a result of this reaction a larger radical molecule is created (figure 1.3c). If this newly formed radical appears in proximity of another oligomer molecule it can react by once again breaking the methacrylic bond (figure 1.3d) and forming an even larger radical (figure 1.3e). Hence produced radicals serve as propagating active centers of a chain reaction. Reaction continues in this manner until it is terminated by a reaction between two radicals, which can be either photoinitiator fragments or larger radicals.

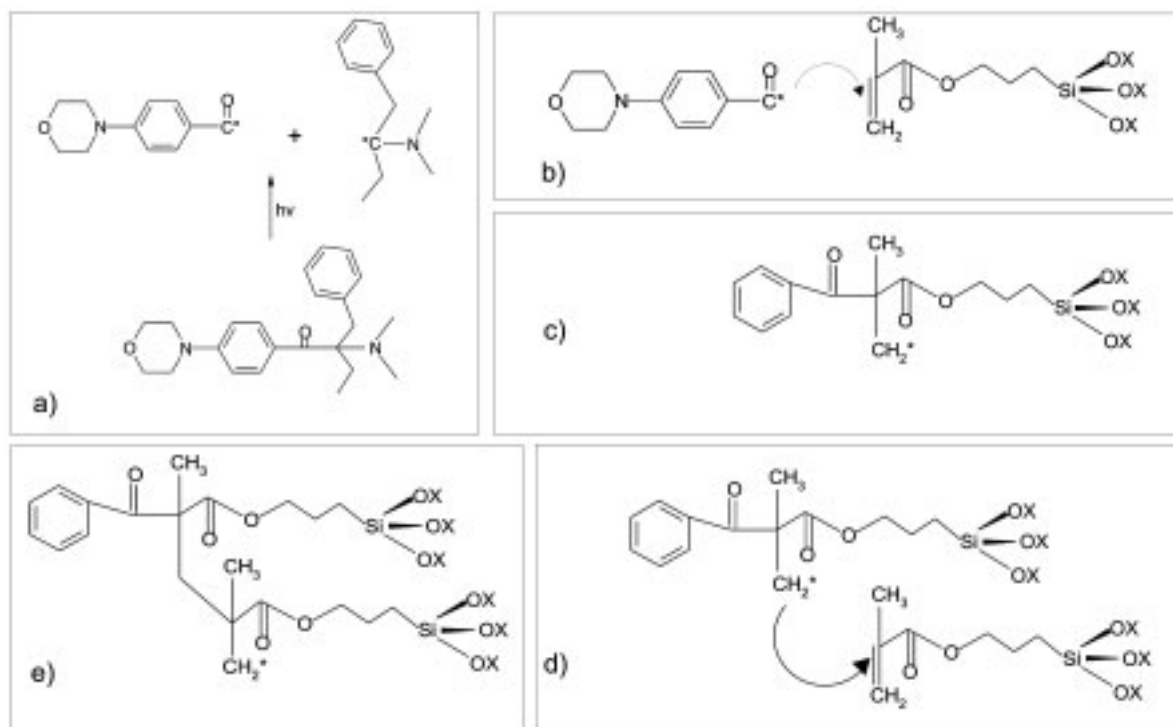


Figure 1.3 Illustration to photoinduced free-radical polymerization process on the example of MAPTMS: a) absorption of a UV photon by photoinitiator Irgacure 369 results in bond-cleavage and production of two radicals; b) radical reacts with MAPTMS molecule by breaking a methacrylic bond (indicated by arrow); c) a larger radical molecule is created as a result of this reaction; d) it can further react with another MAPTMS molecule by breaking a methacrylic bond (indicated by arrow); e) an even larger radical molecule is created as a result of this reaction.

Compared to other initiation routes, e.g. thermal in which heat is used to produce active centers, light-induced polymerization offers certain advantages. Most importantly in the context of this thesis, it provides both spatial and temporal control of the initiation reaction through control of illumination conditions. Linear polymer chains are obtained by

reacting monomer species that contain a single double bond, while a cross-linked network of polymer chains can be formed using multifunctional monomers. The resulting solid polymers are used in many applications due to their insolubility in organic solvents and resistance to heat and mechanical treatments [Rof82].

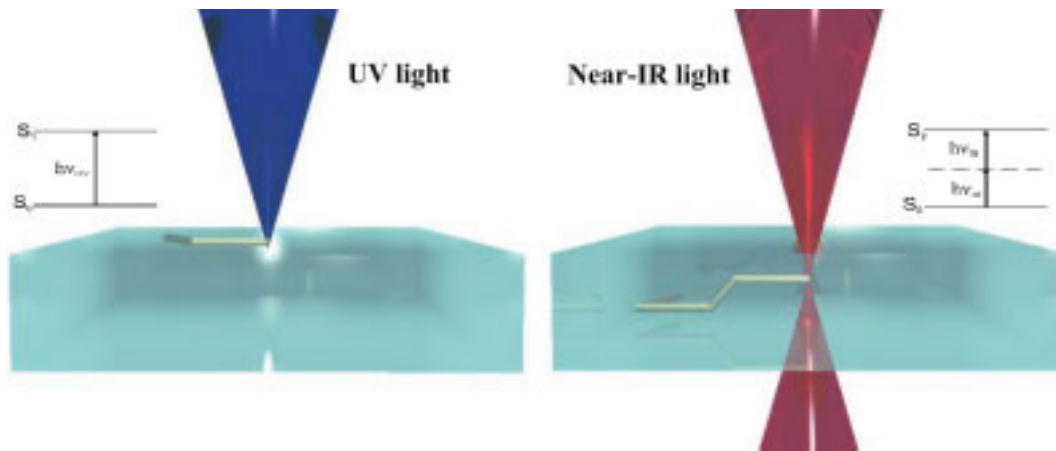
Main drawbacks of free-radical polymerization are oxygen quenching and polymer shrinkage [FR93, KS02]. At normal conditions some atmospheric oxygen is always dissolved in the material. During free-radical polymerization it can deactivate the intermediate states by producing oxygenated radicals and so slowing down or disturbing the polymerization reaction. In thick films oxygen quenching is mostly expressed in the upper layers of the material, which are in direct contact with the atmosphere. Shrinkage is a result of increased density of the final polymer state compared to the density of original material formulation before polymerization. Since the amount of material before and after polymerization does not change, this density change will result in volume reduction i.e. shrinkage. Recent efforts in the material synthesis field brought about some novel materials that exhibit very little shrinkage even when polymerized via free-radical route.

An alternative material system often applied in photopolymerization is based on ionic polymerization. Here ions play role of active propagating centers. The advantages of ionic polymerization are the absence of oxygen quenching and substantially lesser shrinkage. A prominent example of such material is commercially available SU8, also widely applied in multiphoton processing. Here, photoacid generators can be interpreted as photoinitiators, since acid, generated during light exposure, acts as polymerization reaction catalyst and spacially defines the produced pattern. Polymerization reaction itself is induced by cations, and requires addition of heat, i.e. sample postbaking. This implies that in contrast to free-radical polymerization mechanism, here the exposure and the polymerization steps are separated. Compared to free-radical route, disadvantages of cationic material systems are longer sample processing time and often less temporal and spatial control over the reaction.

1.3 Two-photon Polymerization Technique

Two-photon polymerization (2PP) is a novel direct laser writing technique based on the two-photon absorption (TPA) of laser radiation in photosensitive polymers. The mechanism of this technique is best explained in comparison to another widely known rapid prototyping technique - stereolithography. In stereolithography UV laser radiation is applied to scan the surface of the photosensitive material (in the UV range). This radiation induces photopolymerization through single photon absorption, and is therefore confined to the surface of the material. Single surface irradiation step is producing 2D patterns of polymerized material (Figure 1.4a). Another liquid photopolymer layer is then deposited/flown onto such pattern in order to create a new surface. The steps are repeated until the complete 3D structure is produced. Finally, in a so-called developing step, the unpolymerized material is washed out and the fabricated structure is revealed. Due to linear absorption nature of the process, with stereolithography it is only possible to fabricate 3D

structures using a layer-by-layer approach. The liquid polymer reflow step requires high precision, it is relatively slow and constitutes the largest part of the fabrication duration.



a) b)
 Figure 1.4 Photosensitive material processing by: a) a single photon absorption with UV light. Light is absorbed at the surface of the photosensitive material. 2D patterns can be produced by photopolymerization; b) two-photon absorption with near-infrared light. TPA and following chemical reactions are confined in the focal volume, and the rest of the laser radiation is passing through the material without interaction. According to insets in the figures illustrate: a) single photon absorption; b) two-photon absorption processes.

Majority of available photosensitive materials are designed to be structured using UV radiation sources. They are transparent in the near-infrared and highly absorptive in the UV spectral range. 2PP approach is based on the nonlinear interaction between the materials and laser radiation through TPA. One can initiate two-photon polymerization with near-infrared laser pulses within the small volume of UV-sensitive material using tightly focused femtosecond laser pulses. Figure 1.4 provides a simplified illustration of the difference between single photon and two-photon activated processing. In 2PP most of the laser light focused into the sample from the top is passing through the material without interaction and exits at the bottom. The laser-material interaction is strictly limited to the waist of the focused laser beam, where the intensity is high enough to induce the TPA (see Figure 1.2 in section 1.1). The material is polymerized along the trace of the moving laser focus. This way fabrication of any desired polymeric 3D pattern by direct “recording” into the volume of photosensitive material is possible (figure 1.4 b). In a subsequent processing step the material, which was not exposed to the laser radiation, and therefore, stayed unpolymerized, is removed by an appropriate solvent and the fabricated structure is revealed. The material sensitive in the UV range (λ_{UV}) can be polymerized by irradiation with the near-infrared laser light at approximately double wavelength ($\lambda_{IR}=2\lambda_{UV}$), under the condition that the intensity of the radiation is high enough to initiate TPA. Since femtosecond lasers provide very high peak intensities at the moderate average laser power, they present a very suitable light source creating favourable conditions for TPA and are commonly used in 2PP microfabrication.

In stereolithography the structural resolution depends on the size of the focal spot and is limited by diffraction, thus the minimum feature size can not be smaller than the half of the applied laser wavelength. In reality, due to the technical reasons, inherent to this technology,

the best lateral resolution of stereolithography is in the range of a few micrometers [BJB⁺03]. Since 2PP is a nonlinear process displaying threshold behaviour, the structural resolution beyond the diffraction limit can be realized. Structures with feature size less than 100 nm have been realised experimentally, which is almost an order of magnitude smaller than the laser wavelength used for microstructuring (usually a Ti:Sapphire laser at 800 nm).

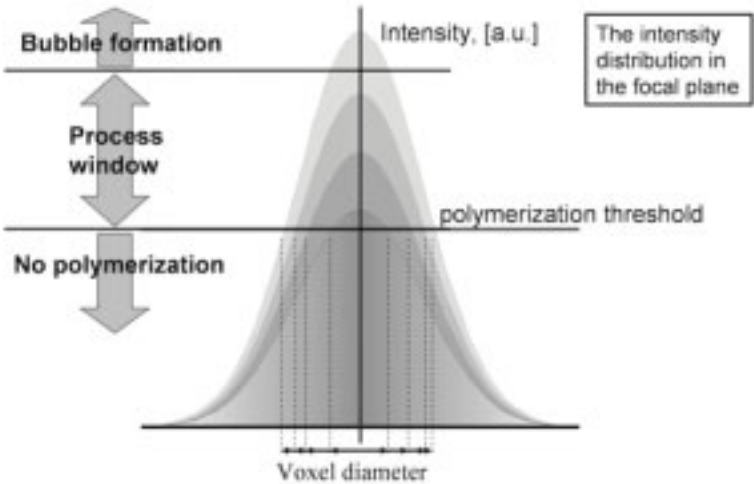


Figure 1.5 Effect of intensity on the volume pixel (voxel) size i.e. structural resolution of 2PP process.

For all photosensitive materials, a threshold irradiation fluence (and/or irradiation time) exists which has to be overcome to initiate polymerization. Due to this well-defined polymerization threshold, one can reach a resolution far beyond the diffraction limit as is schematically illustrated in figure 1.5 for a Gaussian intensity distribution in the laser focus plane. Precise control over the applied irradiation dose is used to tune the obtained structure size.

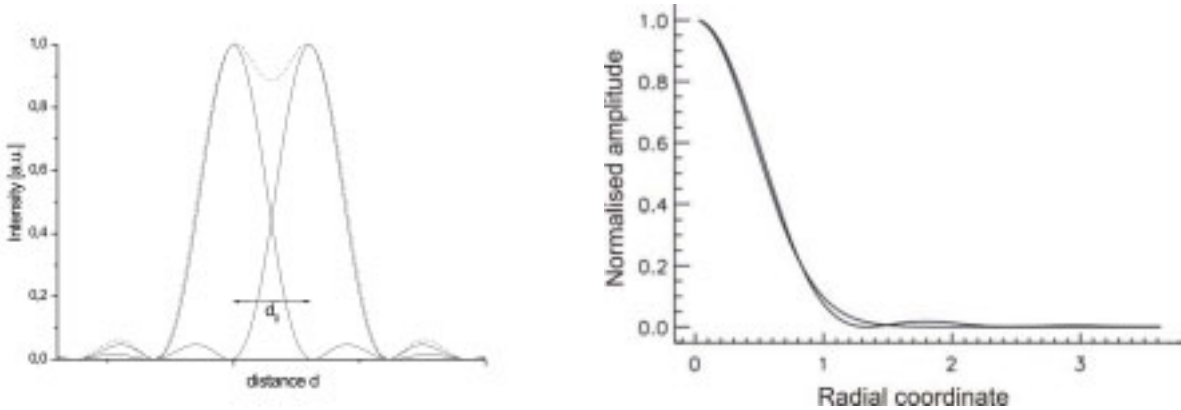


Figure 1.6 a) Rayleigh criterion for resolution of an optical system; b) Airy pattern approximation by a Gaussian distribution.

There are several factors determining the structural resolution limits of 2PP microfabrication. In general for multiphoton processing, the higher the order of process nonlinearity, the better the spatial resolution. For a fixed process order, for example 2PP, two further factors are of great importance. One is set by the material composition, i.e. the lowest limit for the structure size for a certain material is set by the size of the molecules composing this material. Another factor is related to how close one can approach the 2PP process threshold. Here both laser characteristic and material composition play an important role. Finally, the classical resolution limit is set by the intensity distribution in the waist of the diffracted laser beam, which is in direct relation with the wavelength of the laser and the numerical aperture (NA) of the imaging optics.

Intensity distribution in the focal plane of a microscope objective is governed by the theory of Fraunhofer diffraction. For a microscope objective with a round aperture a point source forms a so-called Airy pattern in the image plane. The intensity distribution here is given by a Bessel function of the first order. The central peak exhibits a maximum intensity, the amplitude oscillates and gradually decreases away from the centre. In accordance to the Rayleigh criterion two equally bright point sources can be resolved by a microscope if in the image plain the intensity maximum of the Airy pattern formed by one source coincides with the first minimum of an Airy pattern formed by the second source (see figure 1.6a). Therefore, in accordance to this criterion, the lateral and axial values of diffraction-limited resolution of a microscope objective are given accordingly by [Ino95]:

$$D_{xy} = 0.61 \frac{\lambda}{NA} \quad \text{and} \quad D_z = 2 \frac{\lambda n}{NA^2} \quad (1)$$

where λ is the exposure wavelength, NA is the numerical aperture of the objective ($NA \cong r/f$ where r is the radius of the lens and f is the focal length), and ' n ' is the refractive index of the sample material.

The amplitudes of side peaks of this intensity distribution are small compared to the amplitude of the central peak. Due to the threshold behaviour of a TPA interaction, in most cases side peaks do not contribute to the 2PP microstructuring process. The central peak of intensity distribution in turn can be well approximated by a Gaussian distribution (see figure 1.6 b). In order to deduce relation for a volume pixel (voxel) width and height one has to find isophotes of light intensity. In accordance to (1) for intensity drop to $1/e=0.37$ times the peak intensity the Gaussian beam width in the focal plane is given by $d_{xy}=0.21\lambda/NA$. According size along the axial direction is given by $d_z=0.66 \lambda n/NA^2$ [TRS⁺02]. The size of the interaction region or polymerized volume (volume pixel or voxel) depends on the polymerization threshold. The spatial intensity distribution of a Gaussian beam as a function of the axial and radial distances ' z ' and ' r ' is described by a following function:

$$I(r, z) = I_0 \frac{\omega_0^2}{\omega(z)^2} e^{-2\left(\frac{r}{\omega(z)}\right)^2}$$

here ' ω_0 ' and ' $\omega(z)$ ' are the size of the beam waist ($z=0$) and the beam radius in the plane at distance ' z ' from the waist position. I_0 is photon flux at the center of the beam waist ($r=0$, $z=0$). By solving this equation for a fixed threshold intensity ' I_{th} ', one can obtain the width ' ω ' and the height ' h ' of the polymerized voxel. For a second order process following relations are obtained:

$$\omega = \omega_0 \sqrt{\ln\left(\frac{I}{I_{th}}\right)} \quad \text{and} \quad h = 2z_R \sqrt{\left(\frac{I}{I_{th}}\right)^{\frac{1}{2}} - 1} \quad (2)$$

here z_R and ' I ' represent the Rayleigh range and the applied intensity accordingly. The calculated dependency of these parameters on the applied laser intensity for objective with NA=1.4 is shown in the figure 1.7a. Presented relation does not take any material influence on a molecular level or polymerization kinetics into account. Nevertheless, it provides a general idea about the voxel size dependencies in 2PP microstructuring. According to these calculations, for ideal material system, if the intensity is set at 2% above the threshold value voxel width and length of around $\omega = 33$ nm and $h = 80$ nm are obtained. At 5% over the threshold level these values are already $\omega = 52$ nm; $h=125$ nm. For 8% the values are doubled.

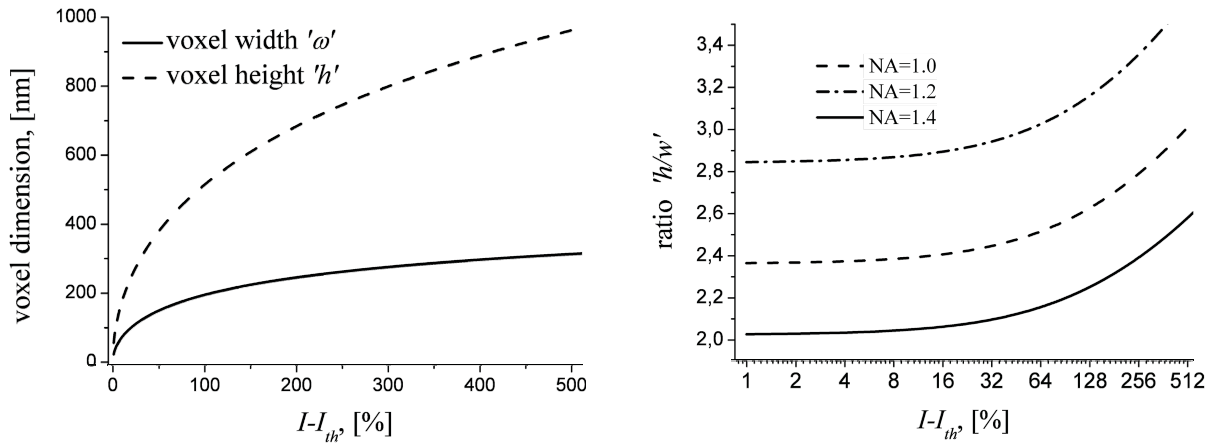


Figure 1.7 Voxel dimension dependence on applied laser intensity: a) voxel width ' ω ' and height ' h ' for a NA=1.4; b) voxel ' h/ω ' aspect ratio for different objective NA values, presented on a logarithmic scale.

It is therefore important to provide precise control over the intensity level of applied laser radiation. In a realistic system the pointing stability and the energy stability of the laser have biggest influence. For many practical applications, relying on the high structural resolution of the 2PP technique, it is important to know the form of the structures primitive building block - the voxel. Figure 1.7b presents voxel aspect ratio ' h/ω ' dependence on applied laser intensity for different NA values. It is observed that with increasing intensity the voxel becomes elongated along the axial direction. For objectives with higher NA not only the

better lateral resolution, but generally smaller aspect ratios can be realised. The NA of the objective used in work presented here is 1.4. Therefore, diffraction in the optical system sets a lower limit on the values of aspect ratios of voxel dimensions.

1.4 Materials for 2PP Processing

Early reports on 2PP microstructuring employed commercially available photoresists originally developed for UV lithography [MNK97, CAB⁺99]. Over the years a lot of effort has been devoted towards development of specialised photoinitiators (see next section for details), which are used with available materials or material blends. From the polymer side, little has been done. While the applied material spectrum has been significantly expanded, still mostly standard lithographic resins are currently used for 2PP microfabrication.

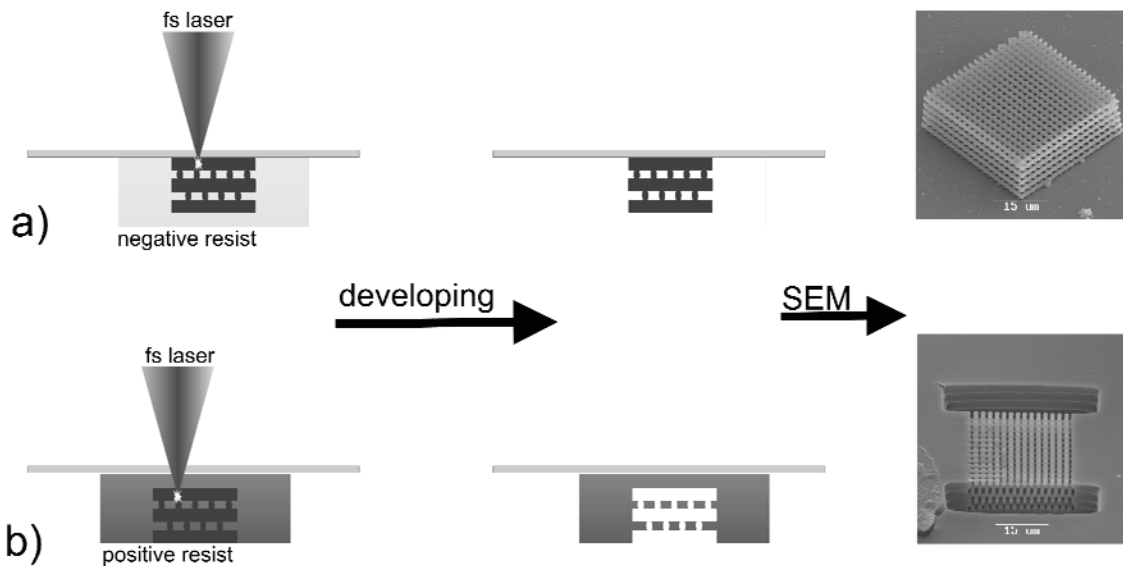


Figure 1.8 Schematics of two-photon activated (a) negative and (b) positive tone resist processing. According insets on the right show the SEM images of fabricated woodpile structures.

Conventionally, photosensitive resist materials are divided in two classes - negative and positive tone. The illuminated volume of negative resists undergoes cross-linking or polymerization, and becomes insoluble in developer. Unexposed material is removed during the sample development step (figure 1.8a), revealing the inscribed pattern/structure. In positive resists situation is exactly inverse - light induces dissociation of the molecules in the irradiated area. Here exposed material is removed during the development step (figure 1.8b), while the rest stays [ZKB⁺02]. Therefore, one obtains a hollow pattern. Most positive resists are developed for the fabrication of integrated circuits by photolithography, where they are patterned in 2D and are used as a sacrificial layer in a lift-off process. Therefore, these resists are designed for an easy chemical or thermal removal. By applying femtosecond laser pulses one can write 3D structures in positive resists, in this case we are talking about two-photon activated processing, since no polymerization is actually taking place. Conventional negative resists are most often acrylate- or epoxy-based resins, i.e. pure organic materials. Although

many of these materials have good processability, they are often chemically unstable against solvents typically applied in multi-layer processing, and their thermal and mechanical stability is often quite poor.

A prominent example of negative tone organic photoresist applied for 2PP microfabrication is SU8 [DFW⁺04, SJJ⁺06]. It was originally developed for the microelectronics industry to provide high-resolution 2D patterns. The SU8 is supplied as a liquid consisting of an epoxy resin, a solvent (gammabutyrolactone or cyclopentanone depending on formulation) and a photo-acid generator. Conventionally SU8 is applied in the form of thin layer onto the substrate by spincoating. The thickness of the resulting layer is controlled by the spinning velocity. In a subsequent prebaking step, the excess solvent is removed from the layer. Here it is important to achieve a uniformly dry layer, since inhomogeneities will lead to undesirable variations of photopolymerization threshold. Prebaking conditions have to be adjusted in accordance to the layer thickness. In 2PP microfabrication, where comparatively thick layers and high resolution are required, the prebaking procedure is especially critical. SU8 is photosensitive in the spectral range 300-400nm, suitable for lithography and LIGA applications. It is polymerised by cationic route, where a strong acid is generated in the irradiated areas. Cross-linking occurs during the postbaking step, when a temperature is raised above a certain threshold value. Since no polymerization is induced during the photoirradiation, there is no immediate refractive index change. This fact implies that, in contrast to free-radical polymerized materials, the produced pattern is not visible online during the fabrication. Finally, the unpolymerized material is removed to reveal a fabricated structure. Due to its high transparency in the near UV, SU8 is a popular material for fabrication of structures with high aspect ratio. Currently, formulations resulting in spincoated layer thicknesses up to 200 μ m are made available. A great advantage of SU8 material for multiphoton processing is comparatively low shrinkage. Also SU8 material is processed in a solid form, and the produced pattern is immobilised throughout fabrication step. Therefore highly complex interconnected/interlocking structures can be produced without fear of material reflow during the fabrication. This is particularly advantageous for fabrication of moving micromechanical components. A certain disadvantage is that SU8 requires a multistep preparation and processing. The sample production times are longer, compared to materials processed by free-radical polymerization. SU8 can also provide quite high spatial resolution. Suspended rods with lateral size down to 30nm have been produced in SU8 by 2PP microfabrication [JMS⁺05]. However, no 3D structure consisting fully/mostly of elements with 30nm feature size has been demonstrated.

A large variety of acrylate- and methacrylate-based materials, which are polymerized via free-radical route, were tested with 2PP microfabrication. Among most popular, one can list SCR500 [MNK97] (Japan Synthetic Rubber Company), Nopocure 800 [SMX⁺01] (Sannopco, Japan), PDMS (Dow Corning), SR368 and SR9008 [CAB⁺99] (both SR by Sartomer Corporation). A blend of both latter materials was successfully used by Haske et al. to fabricate woodpile structures with features sizes as small as 65 nm [HCH⁺07]. In general these materials are marked by straightforward preparation and processing. Since the

polymerization occurs immediately after irradiation, the produced patterns can be observed online and so substantially simplify the fabrication procedure. The sample processing times are greatly reduced in comparison to epoxy-based materials processed by ionic polymerization. A majority of acrylic resins is processed liquid form, and material reflow during the fabrication can be an issue.

Another example of purely organic photopolymers are Poly(ethylene glycol) (PEG) based formulations. PEG molecules can be functionalised with acrylic or methacrylic groups in order to produce photosensitive resin, processable by free-radical polymerization. Recently our group at the Laser Zentrum Hannover has explored these materials in combination with 2PP microfabrication (see section 3.2). Use of PEG-based materials has a few great advantages for biomedical applications. It has proven to be non-toxic, and use of some of its derivatives is approved by the FDA and other governmental organisations for the variety of commercial products. The properties of PEG and PEG-based materials have been well studied with respect to use in a number of biomedical applications. PEG actually includes a whole class of materials, most commonly used for biomedical applications are grades between PEG 600 and PEG 9000. It has been demonstrated that aqueous solutions of acrylated PEG can be photopolymerized in direct contact with cells and tissues [LB02]. The degradation rate of PEG materials depends on the molecular weight and material content. Furthermore, the PEG polymers can be functionalized using various biomolecules and proteins in order to influence specific cell adhesion [VVH03, HVP⁺02]. This is a great advantage for application in medical implants, where it is extremely important to achieve control over material-cell interaction, by either preventing or promoting specific cell adhesion.

More recently, photosensitive inorganic-organic hybrid materials have been used for 2PP microfabrication by our group at the Laser Zentrum Hannover [SEO⁺03]. The concept of hybrid materials is that they combine properties of organic polymers (toughness, functionalization, and processing at low temperatures) with those of glass-like materials (hardness, chemical and thermal stability, and transparency) [Haa00].

Hybrid materials, presented in this work, are synthesised by sol-gel process [BS90], where inorganic-oxidic units are connected to organic moieties on a molecular level [KP05]. This approach allows one to achieve material properties which are not accessible with composite or polymer materials. During synthesis, a Si-O-Si network is established via hydrolysis/polycondensation reactions of alkoxysilanes, which yields organically modified nanoscaled inorganic-oxidic units, present in a prepolymer sol. Their size (typically 1 to 10 nm) is dependent on the choice of alkoxysilane precursors and the reaction conditions, such as catalyst, concentration, or reaction temperature. The organic polymerizable units are chosen depending on the requirements of the application. For the photosensitive materials presented in this thesis, (oligo-) methacryl or acryl functionalities are used as organic moieties (see section 2.2 for detailed description of ORMOSIL synthesis). Finally, an organic cross-linking is achieved by photopolymerization. Hybrid photosensitive materials are multifunctional polymers. During photopolymerization they are cross-linked and form a dense 3D network,

the final product is similar to glass. For the photochemical patterning, radical initiation is a most popular route.

The physical and chemical properties of the end-material can be tailored by choosing appropriate precursors and synthesis conditions. The mechanical properties and thermal stability can be increased by increasing the inorganic content in the hybrid network. Furthermore, sol-gel materials provide the possibility of the incorporation of various functional groups by using a guest–host or a side-chain–main-chain strategy. One example is the incorporation of a nonlinear optical chromophore to produce an electro-optically active sol-gel processable by 2PP technique (see section 2.2 for details).

Therefore, these hybrid sol-gel materials can be employed in many devices for a large variety of applications, enabling novel properties from micro- down to the nanometre scale. Due to their enhanced chemical, thermal, and mechanical stability and – simultaneously – very good processability, they can overcome the restrictions of purely organic polymers for most applications.

Two different kinds of hybrid materials are applied in the presented work: commercially available ORMOCER® (organically modified ceramics, Trademark of the Fraunhofer-Gesellschaft zur Förderung der Angewandten Forschung e.V., Munich, Germany) and ORMOSILs (organically modified silica) synthesised in our group at the LZH. In both materials, methacrylate functional groups are responsible for cross-linking of monomers during photopolymerization.

Ormocers are optically transparent over the 400–1600 nm wavelength range [BKP⁺01]. These materials demonstrate low optical losses in the near infrared range, with losses less than 0.06 dB/cm at 830 nm, and less than 0.6 dB/cm at 1550 nm. The refractive index of Ormocer materials may be adjusted in the 1.47-1.56 range. Due to their superior optical properties and ease of processability Ormocer are now widely applied for optical interconnects and multi-chip module assembly. They are conventionally patterned by UV lithography or nanoimprinting [www.MR].

Ormocers as a material class have recently received significant interest from the medical device community. Several biological studies, including the ISO 10933-5 cytotoxicity (elution) assay, have shown that Ormocer materials are nontoxic and biologically inert [ADM05, JRK⁺04]. Ormocer- based matrix components (Definite™) and Ormocer-based light-curable dental composites (Admira™) have been commercially available for use in restorative dentistry since 1988. Also in the present work Ormocers have been mostly studied with respect to biomedical applications.

Ormosil also designates a class of hybrid materials. From practical point of view synthesis of materials directly at our laboratory at the LZH provides many advantages. Most importantly the properties of the synthesised materials can be modified in accordance to the demands of 2PP technique. By adjusting the synthesis conditions materials exhibiting ultra-low shrinkage during 2PP were realised. Materials containing Zr, Al, Ti, or combination of these have been synthesised. Also hybrids containing active ions such as Erbium and Ytterbium were synthesised and successfully structured by 2PP technique. Furthermore, in

this work, the sol-gel process has been used to prepare photosensitive composites containing nonlinear optical chromophores (see section 2.2 for details). Ormosils are processed in a solid form, and so they combine advantages of epoxy materials with processability of acrylic formulations.

An important component of any material processed by photopolymerization is the photoinitiator (see section 1.2). Due to wide use in industrial applications, currently a large variety of photoinitiators for free-radical polymerization are commercially available (e.g. from Ciba Specialties, Sigma-Aldrich). Naturally, the most important characteristic of a photoinitiator is sensitivity at the applied irradiation wavelength. The absorption spectra of two typical photoinitiators developed UV curing and applied in 2PP microfabrication are shown in figure 1.9. Spectra of 2-Benzyl-2-dimethylamino-1-(4-morpholinophenyl)-butanone-1 (Irgacure 369, Ciba Specialties) is recorded for photoinitiator solutions in acetonitrile. Irgacure 369 is a standard photoinitiator supplied with Ormocer materials. Its absorption extends up to 400nm and exhibits a peak at 320nm. For 2PP microfabrication this corresponds to approximately the double wavelength, i.e. up to 800nm with an optimum at 640nm. Typically not more than 2wt% of Irgacure is added to photocurable material formulations.

The spectra of 4,4'-bis(diethylamino)benzophenone (Milchers Ketone, Sigma-Aldrich) is recorded for different concentration solutions in methyl alcohol. This photoinitiator has an optimum absorption at 380 nm, which would correspond to approximately 760 nm for two-photon absorption. Therefore, due to absorption at the longer wavelength this molecule appears to be more suitable for 2PP processing with Ti:Sapphire lasers.

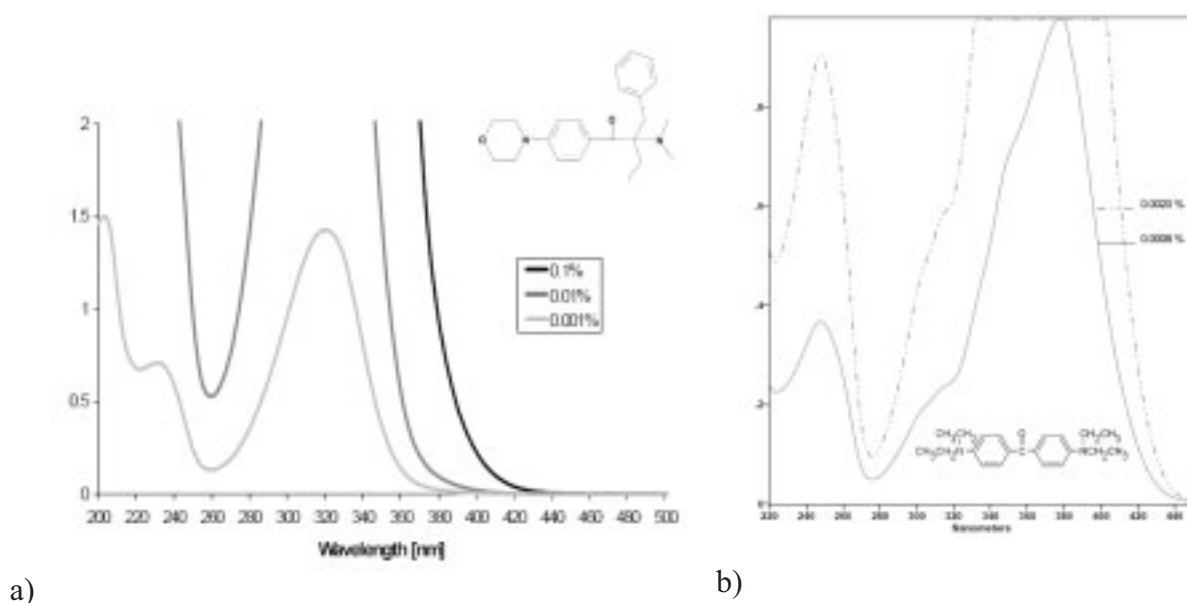


Figure 1.9 Absorption spectra of typical photoinitiators for UV curing: a) Irgacure 369; b) 4,4'-bis(diethylamino)benzophenone.

Most photoinitiators are characterised by measuring their absorption in solutions. Our recent findings show that absorption characteristic can change, when the photoinitiator is

introduced into a realistic photopolymer formulation. E.g. for the case of 4,4'-bis(diethylamino)benzophenone in Ormosil the absorption peak is shifted towards longer wavelength and peaks around 470nm (see section 3.1). Therefore when choosing an appropriate photoinitiator, it is important to consider its characteristics in combination with a material in question. Among other important photoinitiator characteristics are high rate of photodissociation (i.e. short excited state lifetimes) and efficient reactivity of produced radicals with material molecules.

1.5 Current Development Status and Applications of 2PP Technique

Since first experimental demonstration of 2PP microstructuring [MNK97] to nowadays it has experienced rapid development. Unique capability of this technique to create complex 3D structures with resolution, reproducibility and speed superior to other approaches paved its way to applications in many areas. Figure 1.10 shows some SEM images of structures fabricated by means of 2PP technique for demonstrational purposes in the framework of this doctoral thesis at the Laser Zentrum Hannover. Microvenus statues fabricated from the SU8 material are presented in comparison to the human hair. Each statue is about 50 μm tall and 20 μm wide, the overall fabrication time is just few minutes. Figure 1.10b shows an array of microspiders fabricated on a glass slide. Each structure is about 50 μm wide, the spiders body is lifted above the glass supported by eight 2 μm thick legs. Finally, a fragment of a windmill array (figure 1.10c), produced by 2PP ofOrmocore material is shown. Fabricated in a single step, the structure consists of two physically separate parts - windmill body and propeller, which are interlocked in such way that propeller can be rotated around the shaft. Therefore, using 2PP microfabrication it is possible to produce functional micromechanical components in a single step, without the necessity of tedious assembly procedure. Looking at these images one can see the strength of 2PP technology and envision many potential applications. Naturally, the research in this field can be roughly subdivided into topics related to investigations of fundamental processes underlying the mechanism of 2PP technique itself and topics oriented to applications of this approach and investigation of related phenomena.

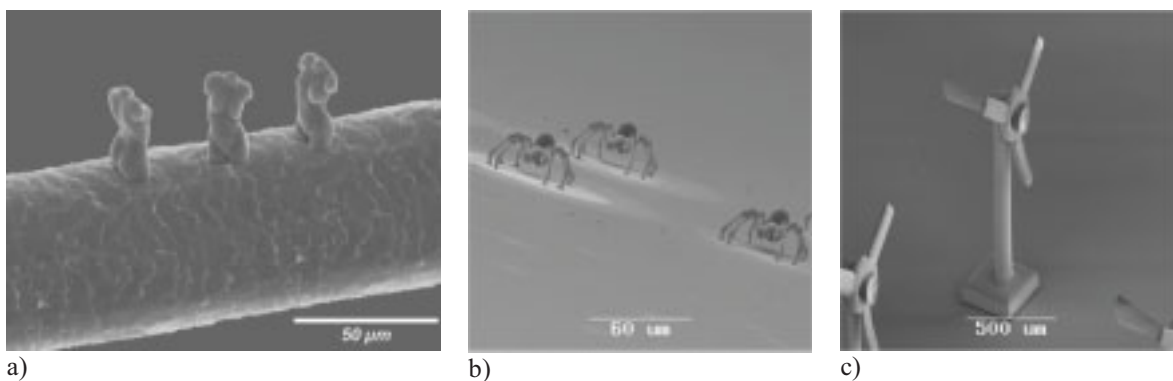


Figure 1.10 SEM images of demo structures fabricated by 2PP technique: a) microvenus statue shown in comparison to a human hair; b) microspider array; c) functional microwindmill.

Most of the materials and photoinitiators applied for 2PP are originally developed for the lithographic applications. A lot of efforts have been dedicated to improvement of the efficiency of 2PP initiation. It is conventionally done by application of novel specially developed photoinitiators exhibiting large two-photon absorption cross-sections. Commercially available photoinitiators used in photolithography exhibit maximum two-photon absorption cross-section values in the range of 4-40 GM units [SHB⁺04]. The extensive work in this field and acquired knowledge allowed to synthesise molecules with two-photon absorption cross-sections as large as 100-7000 GM [SHB⁺04, JPS⁺99, CAB⁺99]. It has been demonstrated that the structural resolution of the 2PP process is improved in materials with higher sensitivity [XCD⁺07]. In addition, introduction of radical quenchers to the material has been investigated, using this approach a minimal structural resolution of 100nm has been demonstrated [TSK05]. Recently, 80nm wide lines, suspended on a massive structure, could be obtained in the SU8 material using conventional fs laser system emitting at 800nm [SJJ⁺06]. Using fs laser radiation at 520nm, 3D woodpile structure with lateral feature size of 65nm was achieved by 2PP of acrylate based material [HCH⁺07]. Two-photon activated processing has also been applied for microstructuring of so-called positive tone photoresists [ZKB⁺02]. Here the effect of irradiation is the material dissociation in the focal volume. In the later development step, only the material from the exposed area is removed and therefore an inverse pattern is obtained.

Despite the fact that the 2PP is a relatively new technology it has been successfully established as microprocessing tool and its application area has been rapidly expanding in the recent years. Most prominent example is fabrication of 3D photonic crystals. For this purpose 2PP technique has been first demonstrated in 1999 [SMM99, CAB⁺99] and by now is applied by different groups in the world. Submicrometer structural resolution of 2PP microfabrication allowed realisation of 3D photonic crystals operating in the near-IR spectral range [DFW⁺04, SNF⁺04, SMM⁺05]. Most importantly, in contrast to most rival methods, 2PP has capability to create arbitrary structures and therefore to introduce defects at any desired location of a 3D photonic crystal. 2PP microfabrication has also been applied for fabrication of less demanding microoptical components such as waveguides [KBL⁺05], diffractive optics [GXZ⁺06] and refractive microoptical elements [WRZ⁺06]. Distributed feedback microlaser has been demonstrated by 2PP of optical gain medium by Yokoyama et. al [Yok03]. Apart from that, 2PP is also used for the fabrication of micromechanical systems [SKX⁺00], plasmonic components [RPC⁺06], biomedical devices [DJN⁺06] and scaffolds for tissue engineering [SNO⁺07]. One of the most exciting application examples for the field of biotechnology is direct structuring of biomolecules. Group of Campagnola experimentally demonstrated cross-linking of proteins by use of fs lasers [PCE⁺00, BC04]. Functionalization of surfaces with biomolecules via photoinduced process using fs lasers has also been considered and recently demonstrated [DKC⁺08]. Optically actuated micromechanical devices fabricated by 2PP have been extensively investigated for applications in microfluidic systems and cell manipulation [MIK03, Mar06]. Photosensitive materials currently applied for 2PP microfabrication are intrinsically dielectric. Few recent reports demonstrated various approaches for metallization

of 2PP produced structures [FTT⁺06, FTC⁺06, CTT⁺06, MJT⁺07]. Microelectrical components such as microinductor coils have been created this way [FLP⁺06].

Throughput is an important factor for the long-term success of any technology. With the availability of positioning systems providing high translation velocity and high-resolution at the same time, structures at scanning speeds up to 10 mm/s could be produced with 2PP microfabrication [AEH⁺07]. Just as any other direct laser writing technique, 2PP microfabrication is inherently a serial process. It is advantageous when samples with varying parameters or small series of identical samples are required. However, for many applications, especially in perspective to applications in mass production, it is necessary to obtain large series of identical samples. At the same time, when it comes to structural resolution and flexibility, 2PP technology represents a unique approach. Therefore, upgrading it to parallel processing capability would create a great advantage and provide new opportunities. A possible solution, combining advantages of 2PP microfabrication and increasing throughput, is multibeam or multispot processing. Here, the same positioning system can be used for obtaining multiple structures in parallel. It has been realised by application of microlens arrays producing few hundred focal spots simultaneously [KTA+05, MJM05]. A more flexible approach is usage of spatial light modulators (SLM), since here number of spots, their positions and laser intensity for each spot can be adjusted [OPO⁺07]. Common for these methods is that throughput is in direct relation to the number of applied beams/foci. The requirements for the minimal laser system output have to be adjusted accordingly. Furthermore, alignment of the optical system becomes critical for the quality of each produced structure.

Alternative solution is replication of produced structures by UV-micromolding. This method is closely related to well-known soft lithography [GXL⁺04]. Here the structures, produced 2PP microfabrication, are used as a master for soft elastomeric mold preparation. In further steps this mold is used to produce replica in a UV-sensitive material [LBF⁺04]. The detailed description of this process can be found in section 2.4. In contrast to multibeam fabrication here only certain geometries and not any desired complex 3D structure can be reproduced. The restrictions are mostly related to the possibility of mold release. Recently, replication of 3D structures containing closed loops has been demonstrated [LLF06]. Using this approach the throughput can be increased manifold independently of the 2PP microfabrication system capacity. A further advantage of UV-micromolding is the freedom of material choice. The material used for replication has to be photosensitive, but it is not necessary the same material as used for 2PP microfabrication of original structures. Therefore, the microstructures can be reproduced from a material photosensitive in a different spectral range, or from materials containing additives, such as for example nanoparticles, and from materials that cannot be structured well by 2PP technique (see section 2.4 for details).

In the age when third dimension becomes critical issue in many applications, 2PP technology will continue to expand and provide solutions to the new areas. In pace with technology development, the number of materials applied for 2PP microfabrication is constantly increasing and materials designed for specific applications are developed.

Although most of the novel photoinitiating systems are not commercially available, the progress in this field is tremendous. The demand will naturally create offer for novel specialised materials. It is clear that further downscaling of the resolution limit is still possible and 2PP technique has not faced its limits yet. With the dawn of turnkey ultra-short pulsed laser systems and high scanning velocity high-resolution positioning systems, 2PP microfabrication finally enters the realm of industrial applications.

1.6 Photonic Crystals – Engineering the Propagation of Light

Photonic crystals are artificial dielectric microstructures exhibiting periodic modulation of refractive index [Yab87, Joh87]. Due to this periodicity they can diffract electromagnetic waves in a way that prevents their propagation. In analogy to solid-state physics, the range of wavelengths, in which no propagating states exist, can be interpreted as a gap in the dispersion function, it is also known as a photonic bandgap. A most prominent example of one-dimensional photonic crystals are dielectric mirrors or multi-layered dielectric stacks, exhibiting high reflectivity for light of a certain wavelength incident at a certain angle upon such stack. Here the periodicity along one direction is achieved by the variation of dielectric indices of stacked dielectric layers.

The main distinction of a 3D photonic crystal is that one can design structures where photonic bandgaps for different light propagation directions overlap, resulting in a complete or omnidirectional photonic bandgap - a frequency range for which the propagation of light is forbidden in any direction. The central frequency of the bandgap or the photonic crystal operation wavelength is roughly on the order of the half of the dimension of periodicity. Therefore, by tailoring the structures dimensions and dielectric index contrast, the position of the central frequency of the photonic bandgap can be precisely adjusted. For 3D photonic crystals the periodicity has to be achieved for any given propagation direction inside the structure. It is commonly done by sequential succession of air and dielectric regions inside the structure.

For the past decades, semiconductors technology has played a role in almost every aspect of our daily lives. The drive towards miniaturization and high-speed performance of integrated electronic circuits has stimulated considerable research around the world. Unfortunately, miniaturization results in circuits with increased resistance and higher levels of power dissipation. In an effort to further the progress of high density integration and system performance scientists are now turning to light instead of electrons as the information carrier. Devices based on photons, instead of electrons as information carriers have potential to revolutionise the information technology [BLW⁺04, LBB⁺05].

Since the introduction of the principle of the photonic bandgap, the design and construction of 3D photonic devices has been the subject of much research [JJ01, JDW08, Sak05, IO04, NB03]. Devices based on photonic crystals allow tailoring propagation of light in a desired manner. Many fascinating physical phenomena occur in such structures: control of spontaneous emission [JVF97], sharp bending of light [NTY⁺00], lossless guiding [CJT03],

zero-threshold lasing [MFS⁺02], birefringence [NHB⁺01]. Futuristic prospects include not only applications in telecommunications as all-optical signal processing, but also “transistors” for light and optical computers.

However, the fabrication of devices, operating in the near-IR and visible spectral range is a major technological issue, since the requirement is for structures of millimetre scale to be fabricated with nanometre resolution. Already back in 1990 some believed that photonic bandgaps in this spectral range are impossible to achieve [Mad90]. First successful attempts to produce 3D photonic crystals were based on intrinsically planar semiconductor technology approaches, therefore a layer-by-layer structure, known as woodpile (see section 3.2.2. for more detail), was first to be realised. Lin et al. used repetitive deposition and selective etching of multiple dielectric films to fabricate a 5 layer silicon woodpile, exhibiting a bandgap centered at around 11 μm [LFH⁺98]. Chutinan et. al also used deposition of multiple semiconductor films [YNS97, NYI⁺99]. In order to obtain the rods, the upper layer, consisting of GaAs, was structured by electron beam lithography or reactive ion etching. The stripe patterns were then assembled on top of each other and joined using wafer bonding technique. The carrier substrate material was then removed by wet etching, revealing a GaAs woodpile containing 4 layers. Later, using this method, the first woodpile operating at the telecommunication range has been realised [NTY⁺00]. An even more tedious approach was undertaken by Garcia-Santamaria et. al [GMU⁺02], they have reproduced a 3D diamond lattice by assembling latex and silica spheres using a nanorobot and an SEM for live observation. In a subsequent step latex spheres were removed to reveal a 3D lattice consisting of silica spheres only, no bandgap effect was demonstrated for this structure.

Currently most promising approaches for photonic crystal fabrication are colloidal self-assembly, holographic photofabrication and direct laser writing by 2PP technique. In colloidal self-assembly, spherical beads from silica, polystyrene or polymethylmethacrylate, are used to produce 3D structures also known as opals. This method is based on natural tendency of such particles to organise into closely packed 3D structure characterised by a face-centred cubic symmetry. Theoretically, large scale photonic crystals can be produced in a fast and potentially inexpensive way. The main problems originate from unavoidable presence of disorder, which can occur due to polydispersity of the microspheres or inherent stacking defects, developing during the opal growth process. Many different self-assembly methods have been developed in order to improve the situation. Currently, the most popular approach is vertical sedimentation, where a carrier substrate is submerged into a colloidal suspension. While solvent is allowed to evaporate, the meniscus, which is formed at the liquid-air interface on the substrate, helps to deposit the spheres in a crystalline arrangement [JBH⁺99]. Such opal photonic crystals allowed to study some properties of 3D photonic crystals experimentally [BJH⁺99]. Despite the fact that by definition opals are photonic crystals, due to low porosity direct configuration cannot have a complete photonic bandgap. These structures are mostly used as a template for obtaining an inverted opal photonic crystals, which, provided that the refractive index contrast exceeds 2.8, can exhibit a complete photonic bandgap [BSS⁺98, BJ98]. For infiltration procedure few methods, that allow filling

the air gaps of an opal with high refractive index materials, were developed [NV01]. After such infiltration procedure, the opal itself is etched away, revealing a porous 3D mesh consisting of high refractive index material. Inverse opal photonic crystals, consisting from silicon, with an omnidirectional bandgap at 1.5 μm were first successfully demonstrated by Blanco et al. [BCG⁺00]. Many photonic crystal applications, such as low-loss waveguides or zero-threshold optical cavities, rely on the presence of line or point defects, introduced into the 3D structures in a controlled manner. These defects cannot be formed by self-assembly. Lee et al. have applied 2PP technique to write waveguides inside an opal whose voids are filled with a liquid photosensitive material [LPB02]. In order to produce opals shaped as prisms [YX02] or microfibers [MYT⁺02] patterned surfaces can be used as substrates.

Holographic recording is a method that allows fast (literally single shot) fabrication of up to few mm large 3D crystals with long range periodicity. The 3D interference patterns, produced by a multiple laser beams, is a well studied subject, because it is used for trapping of atoms. The idea is to record spatial intensity distribution, created by two or more beams, into a photosensitive material. If the beam parameters are chosen properly, it is possible to polymerize photosensitive resin at the locations with higher intensity, while leaving the rest unpolymerized. That is, one has to choose intensities at the maxima to be larger than the threshold intensity for polymerization, while intensities at the minima have to be lower than polymerization threshold. Tuning the intensity inside this working window changes the filling factor and therefore has an effect on stability of the structure. Material that is not polymerized is then washed out to reveal a solid 3D mesh in air. Depending on the number of beams applied and their arrangement, different lattices can be obtained. Period of the produced photonic crystal depends on the wave vectors of the applied laser beams. Campbell et al. have reported results on using interference of four UV laser beam to create periodic 3D pattern in 30 μm thick commercial lithographic SU8 photo resist. Structures with sub- μm features were produced by a single 6ps pulse of a UV laser [CSH⁺00]. Shortly after that Shoji and Kawata have reported fabrication of 3D hexagonal photonic crystal lattice by a two step process: in a first step three-beam interference was used to obtain 2D hexagonal arrangement of rods, in second immediate step two more interfering beams formed additional layers which are perpendicular to the rod array [SK00]. In 2003 Shoji et al. also demonstrated fabrication of woodpile structure by two-step four-beam interference [SSK03]. Four-beam interference produced a square lattice rod array; a woodpile is formed from two such lattices rotated by 90 degrees with respect to each other. Several groups used single-step exposure four-beam interference to fabricate FCC lattices with different filling factors and have optically characterized them [MMB⁺03, WXS⁺03]. In these works umbrella-like beam configuration, where a central beam symmetrically surrounded by three other beams, was used. In 2001 Kondo et al. have proposed laser interference technique using diffractive beam splitter and a mask selecting desired orders of diffraction, second harmonic femtosecond laser pulses were used [KMJ⁺01]. Wang et al. have proposed simplified method, where a single beam was split into four by a cleaved tip prism put in contact with the cell containing photosensitive emulsion. Four refracted portions of the same beam interfere in the sample analogous to the

case of umbrella like configuration [WTY⁺03]. A special case of holographic recording approach, based on application of phase masks, was proposed by Lin et al. [LHD05]. They have generated 3D woodpile structures in photosensitive SU8 in a two step process using two masks, an approach similar to that applied by Shoji et al. for four beam interference [LPB02]. Fabrication of 3D periodic lattices by holographic illumination of photosensitive materials has a great potential as technology for mass production. Theoretical aspects of this approach are well studied. Since the required illumination time is quite short, the requirements for the mechanical stability of the system are not as high as in the case of 2PP microfabrication. Similarly to self-assembled opal structures, the main drawback of holographic photofabrication is that it is not possible to introduce defects in a first fabrication step. Similar to the case of opals an additional step, where waveguides or point defects are introduced by 2PP direct writing is possible. It is easier to realise in this case, since the sample is readily a photosensitive material no additional effort is required in order to match refractive indices. Also final sample developing is a single common step. Common to most available photosensitive materials are values of refractive index that do not allow realisation of complete photonic bandgap in such holographically recorded 3D crystal. In order to overcome this limitation an additional infiltration procedure, similar to that of opal structures, is necessary.

Fabrication of photonic crystals by 2PP technique was first suggested by Cumpston et al. back in 1999 [CAB⁺99]. The structural resolution of this technology is sufficiently high for fabrication of photonic crystals operating at the telecommunication wavelength. Compared to intrinsically serial methods, such as self-assembly or holographic microfabrication, 2PP is relatively slow, since here each structure is produced by direct laser writing. The main advantage is that 2PP allows realisation of any structure, be it periodic or not. Therefore, introduction of defects at desired location or structure shaping do not present any difficulties [SMX⁺01]. This approach is more flexible in a sense that structural parameter variations can be introduced without big efforts. For example in order to change the period of fabricated 3D photonic crystal, it is enough to change the design provided as input for the microfabrication setup. In case of opal self-assembly different bead size has to be applied, which will eventually require adjusting the overall fabrication process parameters and conditions. In holographic microfabrication it will require changing the applied illumination wavelength, and, therefore, again readjusting the fabrication conditions. In the same manner, by providing according input, different 3D structures such as woodpile [SMM99], diamond [KSD⁺03], spiral-based [SMM⁺05] or even quasiperiodic [LCH⁺06] photonic crystals, can be produced by 2PP microfabrication. The refractive index of most photosensitive materials is comparably low. Just as in the case of holographic photofabrication, structures directly produced by 2PP do not possess omnidirectional photonic bandgap. Nevertheless, they can be used as a template for later infiltration with high refractive index material, in order to produce 3D structure with a complete photonic bandgap. This approach has been successfully demonstrated on the example of woodpile structures produced by 2PP technique [TFD⁺06].

2 Materials and methods

2.1 Experimental Setup for 2PP Processing

The main factors determining the performance of the 2PP system are the sample positioning precision, the laser system stability, and the flexibility of the scanning algorithm. The schematic representation of the experimental setup is shown in figure 2.1. The femtosecond solid-state Ti:sapphire laser (Chameleon, Coherent) generates pulses with duration of 120fs and a repetition rate of 94 MHz. The central emission wavelength of such a laser can be tuned between 700 and 1000 nm. Unless otherwise noted, for all the experiments described in this thesis, laser radiation at the central emission wavelength of 780 nm was applied. A small portion of the light exiting the laser is guided into the spectrum analyser for continuous monitoring of the laser emission spectrum. The computer-controlled polarization rotating element in combination with the polarization-sensitive beam splitter enables continuous adjustment of the average power of the beam entering the AOM (acousto-optic modulator). The AOM is adjusted such that the first diffraction order of the beam can pass the diaphragm aperture, while the zero order is blocked. By controlling the AOM on/off state with computer generated TTL-signal, it is used as a laser shutter. In order to completely fill the aperture of a focusing optic and to achieve optimal focusing conditions, the beam is expanded to a diameter of about 10 mm by a telescope. A highly sensitive CCD camera is mounted behind the last dichroic mirror to provide online process observation. The refractive index of applied materials is slightly changed during photopolymerization process, and the 2PP created patterns become visible immediately. The relative position of the laser focus within the sample is controlled by two galvo-scanner mirrors (angular range $\pm 12.5^\circ$, resolution 6.7 μrad) and three linear translational stages (XYZ, resolution 10 nm, maximal travel distance 2.5 cm). Unless otherwise noted, a 100 \times microscope immersion oil objective lens (Zeiss, Plan Achromat, NA=1.4) was used to focus the laser beam.

The average power is measured before the scanning unit and the beam expander, so after losses at the mirrors and the truncation by the microscope objective aperture only 15 % of laser power reaches the sample.

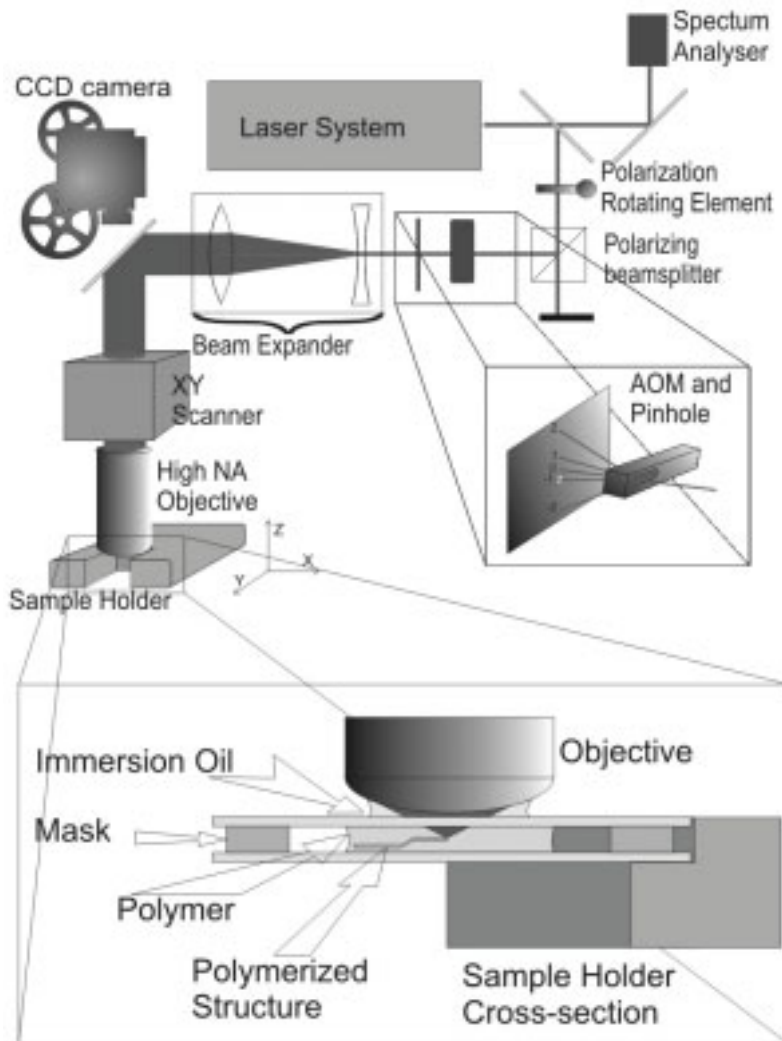


Figure 2.1 Schematic representation of the experimental setup used for 2PP microfabrication

2.2 Materials Applied for 2PP Processing

ORMOSIL

A few sol-gel materials from class of ORMOSILs (organically modified silica) were synthesised at the LZH. The properties of final ORMOSIL material can be tailored by adjusting the synthesis parameters and applied precursors. The refractive index of the final polymer can be adjusted by controlling the Zr or Ti precursor content. It is also possible to add nonlinear materials, e.g. SGDR1. Active materials such as Er or Yt have also been successfully incorporated into these hybrids [XAB⁺03].

Generally the material synthesis and processing is conducted in four steps:

1. Hydrolysis and condensation in which precursors or monomers such as metal oxides or metal alkoxides undergo hydrolysis and condensation to form a porous interconnected cluster structure. Either an acid such as HCl or a base like NH₃ can be employed as a catalyst.
2. Gelation occurs when the solvent is removed and a gel is formed by heating at low temperature. The heating process results in the condensation of the hydroxy-mineral moieties and the formation of the inorganic matrix. Hydrolysis and condensation do not stop with gelation; it is at this stage that solvents are removed and any significant volume loss occurs.
3. Photopolymerization. Because of the presence of the double bonds, and provided a photoinitiator has been added to the gel, the photoinduced radicals will cause polymerization only in the area they are present. At this step there is no material removal and no volume loss; the reaction that occurs is the cleavage of the pendant carbon-carbon double bonds by a free radical process to form a macromolecular network structure of the organic polymer backbone.
4. Development; the sol-gel is immersed in an appropriate solvent and the area of the sol-gel that is not photopolymerized is removed.

During Zr containing material synthesis methacryloxypropyl trimethoxysilane (MAPTMS, 99%, Polysciences Inc.) and methacrylic acid (MAA, >98%, Sigma-Aldrich) are used as the organic photopolymerizable monomers. Zirconium n-propoxide (ZPO, 70% in propanol, Sigma-Aldrich) and the alkoxysilane groups of MAPTMS serve as the inorganic network former moieties. The molar ratio of MAPTMS to ZPO can be varied from 10:0 to 5:5. The difference in reactivity of the alkoxysilane and the zirconium precursor require a three-step procedure for the successful formation of the combined inorganic network: (1) MAPTMS and ZPO are separately hydrolyzed and stabilized by MAA, respectively; (2) the pre-hydrolyzed MAPTMS is slowly added to the zirconate complex; and (3) final hydrolysis of the mixture. The hydrolysis of MAPTMS is performed using HCl solution (0.01 M) at a 1:0.75 ratio. Since MAPTMS is not miscible with water the hydrolysis is carried out in a heterogeneous phase. However, after 20 min of stirring, the production of methanol and the hydrolysis of the alkoxysilane groups are sufficient to allow the miscibility of all species present in solution. ZPO is chelated in a separate vial by adding equal molar of MAA dropwise, the resulting sol is stirred for 45 min.

After 45 min, the partially hydrolyzed MAPTMS is slowly added to the zirconate complex. Following another 45 min, water is added to this mixture with a final 2.5:5 MAPTMS:H₂O molar ratio. A Photoinitiator is added in the final step. After stirring for 24 h, the materials are filtered using 0.22µm filters. Most commonly a 4,4' - bis(diethylamino)benzophenone (Sigma-Aldrich), 2% to the final product is used as a photoinitiator.

The resulting formulation is a transparent liquid. The samples for 2PP processing are prepared by spin-coating or drop-casting the material onto glass substrates, and the resultant films are dried on a hotplate at 100 °C for 1 hour before the photopolymerization. The heating process results in condensation of the hydroxy-mineral moieties and the formation of the inorganic matrix. After writing structures by 2PP polymerization technique, the material, which was not polymerised by the laser radiation, is removed by developing in 1-propanol (Sigma-Aldrich).

ORMOSIL Containing Nonlinear Chromophore

In order to prepare a second-order nonlinear polymeric material, NLO chromophore DR1 (Disperse Red 1, Sigma-Aldrich), was firstly reacted with (3-isocyanatopropyl) triethoxysilane to form a functionalized silicon alkoxide precursor (SGDR1). In a subsequent step SGDR1 was mixed with MAPTMS and the photoinitiator.

(3-isocyanatopropyl) trimethoxysilane and dibutyltin dilaurate (DBTDL) were purchased from Sigma-Aldrich and used without further purification. NLO chromophore DR1 was recrystallized twice from ethanol before use. The synthesis of the NLO-active triethoxysilane was carried out according to [CPR⁺98]. (3-isocyanatopropyl) trimethoxysilane and DR1 at a 2:1 mole ratio were dissolved in anhydrous tetrahydrofuran (THF) under a nitrogen atmosphere. Next, 1 wt% DBTDL was added to the reaction flask and the solution was refluxed for 4 h. The resultant solution was reduced to about half its initial volume under vacuum, followed by precipitation of the product as a red solid in hexane. The final product (SGDR1) was dried in a vacuum oven at 60°C for 24 h and subsequently stored under vacuum until use. The product was characterized by ¹H NMR spectroscopy which verified the successful synthesis of SGDR1.

To obtain the photosensitive gel, SGDR1 was first dissolved in toluene and stirred for 24 h. Then MAPTMS was added to the SGDR1 solution (SGDR1 up to 40% w/w) and the mixture was hydrolyzed by the addition of HCl (pH=1). After stirring for 1 h, Irgacure 369 (up to 3.3 wt% to MAPTMS) was added and the mixture was stirred for a further 1 h. To remove any aggregates, the solution was filtered through a 0.22 μm pore size Millipore syringe filter. After filtration, the solution remained clear without any sign of further particle aggregation for several weeks. Thermogravimetric analysis of the composite showed that it was stable up to 250°C, above which temperature it started to decompose.

The samples are prepared by spin-coating or drop-casting the final mixture onto Indium Tin Oxide (ITO)-coated standard coverslips. The samples are then prebaked on a hotplate at 100 °C for 1 hour. THF is used as a developer for this material. Developed samples are rinsed in 2-propanol.

ORMOCERS

The name Ormocer® (organically modified ceramics) designates a whole class amorphous organic-inorganic hybrid materials developed by the Fraunhofer Institut für Silicatforschung. In presented work a material now commercially available under name Ormocore (Micro Resist Technology GmbH, Berlin) is used. This material is originally developed for optical applications, and is conventionally structured by UV lithography [www.MR] or by UV molding (see next section). Commonly to all Ormocers it possesses high chemical resistance and is thermally stable up to 270°C. Recent studies showed that this material is well suited for biomedical applications [ADM05, JRK⁺04].

Ormocers are also synthesized by sol-gel process [BS90], from liquid precursors, and contain organically modified silicon alkoxides, metal alkoxides, and organic monomers [KP05]. The inorganic components crosslink and form inorganic siloxane (silicon-oxygen-silicon) networks through condensation of organically modified silicon alkoxides and controlled hydrolysis. In case of Ormocore the inorganic backbone is solely established via a polycondensation reaction in order to avoid O-H groups, which would significantly increase the optical absorption around 1550 nm. As silane precursors, diphenylsilanediol and 3-methacryloxypropyltrimethoxysilane are used. The synthesis is carried out at elevated temperatures between 60 and 100 °C with a basic catalyst. By-products which are generated upon synthesis such as, for example solvents like methanol, are removed from the materials under reduced pressure. The synthesis as well as chemical characterisation of the material is described elsewhere in more detail [BKP⁺01].

A standard formulations used for 2PP processing contains 1.8 % of photoinitiator Irgacure 369 (Ciba Specialties), which absorbs strongly in UV and has an absorption peak at around 320nm (see section 1.4). The formulation is therefore highly transparent in visible and near-IR spectral regions, providing a possibility of 2PP microstructuring deep inside the material.

Ormocore is used as received. Since the material is liquid, the sample is prepared in a “sandwich configuration”, where the droplet of the material is placed between two coverslips separated by a spacer (see section 2.1). The structures are “built” on the lower coverslip. After the 2PP processing the unpolymerized material is removed by developing in a 1:1 mixture of 4-methyl-2-pentanone (Sigma-Aldrich) and 2-propanol (Sigma-Aldrich). The sample is rinsed in 2-propanol after developing. In a final step, before the 2-propanol has dried, the sample is exposed to UV-light. The postprocessing UV-exposure leads to cross-linking of any possible residual material in the structure, and so improves its mechanical stability.

Alternatively, in order to avoid any deformation, associated with the capillary forces occurring during the solvent drying on the structures, a critical point drying can be applied (see section 2.4). In this case the 2-propanol has to be replaced by ethanol (Sigma-Aldrich).

Poly(Ethylene Glycol) diacrylates

Poly(Ethylene Glycol) (PEG) is known to be biocompatible, and is widely applied in tissue engineering and drug delivery. There are also a number of PEG-based materials, which have been studied extensively for biomedical applications. Therefore, use of Poly(ethylene glycol) has a few great advantages when it comes to development of novel biomedical applications. It has proven to be non-toxic, and use of some of its derivatives is approved by the FDA and other governmental organisations for the variety of commercial products. The properties of PEG and PEG-based materials have been well studied with respect to use in a number of biomedical applications. It has been demonstrated that aqueous solutions of acrylated PEG can be photopolymerized in direct contact with cells and tissues [KRP02]. PEG actually includes a whole class of materials, most commonly used in biomedicine are grades between PEG 600 and PEG 9000.

In this work, application of 2PP microfabrication to PEG-based photosensitive materials, was studied on the example of two different water-soluble PEGdiacrylate materials, having molecular weights of 302 (SR259, Sartomer) and 742 (SR610, Sartomer). Both materials are transparent for the applied laser radiation. Materials were used as received 2wt% of photoinitiator 4,4' - bis(diethylamino)benzophenone (Sigma–Aldrich; see section 2.4) are introduced by stirring.

The resulting formulation is a transparent liquid. Similar to the case of Ormocer, the samples for 2PP processing are prepared in a “sandwich configuration”, where the material is placed between two coverslips separated by a spacer (see section 2.1). The structures are “built” on the lower coverslip. After the 2PP processing the residual monomer is removed by developing in ethanol or water. In a final step, the sample is exposed to UV-light. The postprocessing exposure leads to polymerization of any possible residual material in the structure, and so improves its mechanical stability.

Alternatively, in order to avoid any deformation, associated with the capillary forces occurring during the solvent drying on the structures, a critical point drying can be applied (see section 2.4). In this case the water has to be replaced by ethanol (Sigma-Aldrich).

2.3 3D Structure Replication by UV-micromolding

Any direct laser writing technique is inherently a serial approach. However, for many applications and in perspective to applications in mass production it is necessary to obtain large series of identical samples. Replication of produced structures by UV-micromolding provides a suitable method. It is closely related to well-known soft lithography [GXL⁺04]. Here the structures produced 2PP microfabrication are used as a master for soft elastomeric mold preparation. In further steps this mold is used to produce replica in UV-sensitive material. Therefore, throughput is increased independently of the 2PP microfabrication system capacity. A further advantage of UV-micromolding is the freedom of material choice. The material used for replication has to be photosensitive, but it is not necessary the same material as used for 2PP microfabrication of original structures. Therefore the microstructures can be reproduced from a material photosensitive in a different spectral range, or from materials containing dopants, such as for example nanoparticles, and from materials that cannot be structured well by 2PP technique.

In this work, molds were produced from polydimethylsiloxane (PDMS). Figure 2.2 presents schematically a process of mold preparation using an array of microvenus structures. Commercially available PDMS monomer and suitable curing agent (Sylgard 184, Dow Corning) are used as received. Accordingly to the recipe they are first mixed in a 10:1 proportion. The resulting highly viscous mixture is degassed under low pressure for a few minutes in order to avoid trapped air bubbles which might compromise the quality of the stamp. The prepared mixture is then poured over the structures fabricated by 2PP technique (the master). A 5mm tall metal ring, placed on the substrate, limits the spreading of liquid PDMS monomer beyond sample border (see figure2.2b). If necessary the PDMS is degassed

one more time under low pressure in order to eliminate bubbles trapped at the structure and PDMS interface. The sample, prepared this way, is placed on a hotplate for 2 hours at 70°C. During this period PDMS is polymerized. At last, the ready elastomeric mold is peeled off the substrate (see figure 2.2d). Due to elastomeric character of such mold it can deform and then acquire its initial shape again. This way it can be peeled off the original 3D structure without destroying it. The sample can be reused again for further mold preparation.

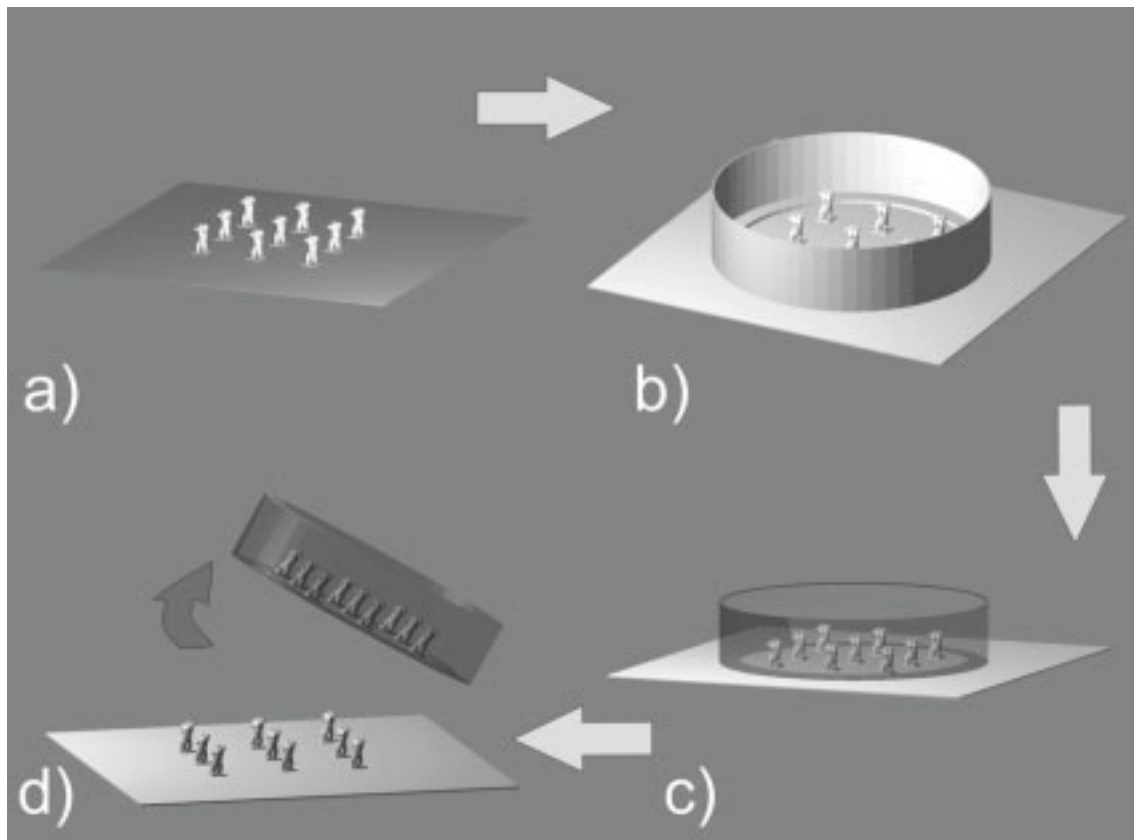


Figure 2.2 Preparation of elastomeric mold from polydimethylsiloxane (PDMS): a) original microstructures produced by 2PP technique on a glass slide are used as a master; b) a metal ring placed on the sample is filled with a liquid PDMS monomer formulation; c) PDMS monomer is thermally cured to produce a transparent elastomeric mold; d) a ready mold is peeled off the structure.

In most cases, the PDMS separation is straightforward. Depending on the material and the structure itself, an antisticking layer, helping the release of the structure, is necessary. Samples microstructured by 2PP technique are analysed by SEM before further replication. For SEM imaging a 100nm gold layer is deposited on the original sample. This gold layer serves as a natural anti-sticking surface, and is sufficient to avoid PDMS sticking to the structures and structure detachment from the substrate. A more sophisticated anti-sticking layer might be required for complex structures [ZCP05, LCK06].

Now that the transparent elastomeric stamp is available further structure replication can be undertaken. UV-micromolding has a few advantages over other imprint processes – it can be performed at room temperature, under atmospheric pressure and therefore does not

require sophisticated equipment. Replication process using produced mold is schematically illustrated in figure 2.3. A droplet of liquid photosensitive material is applied in a glass or other substrate. Mold is pressed against the substrate and its empty cavities are filled with replication material. For structures with complex geometry the material can be applied onto the mold. The mold is then heated or placed in the vacuum in order to ensure that its cavities are filled completely. The mold is then pressed against the substrate and placed under UV-light source (figure 2.3c). After photopolymerization is completed the mold is peeled off the substrate and can be reused again. Produced structures stay attached to the substrate (figure 2.2d). If used replication material exhibits poor adhesion to the substrate, suitable adhesion promoting agent has to be applied to the substrate prior to the replication step.

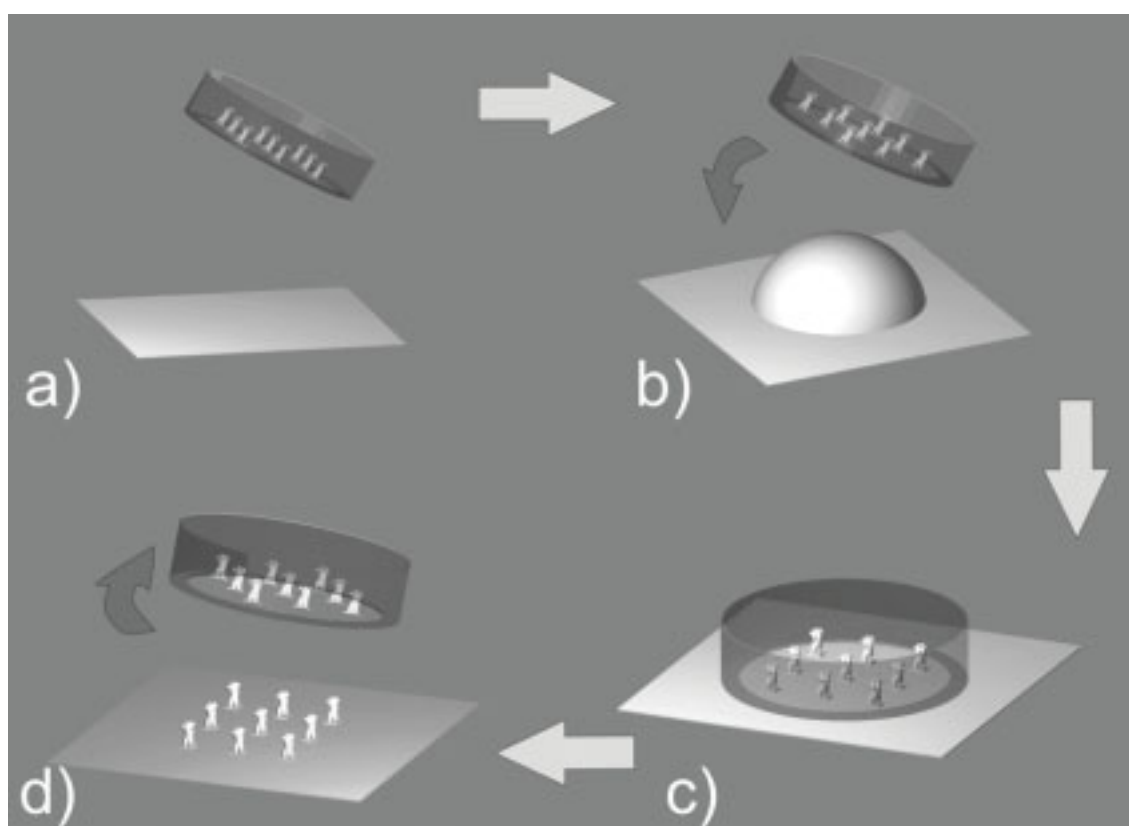


Figure 2.3 Replication of 3D structures by UV-micromolding: a) an accordingly prepared glass slide or other substrate is used as a replica base; b) replication material is applied to the substrate and the mold is pressed against it; c) the sample together with the mold are subjected to UV-radiation in order to cure the replication material; d) the mold is peeled off the structure. Produced structures stay attached to the substrate.

Possibility to replicate 3D microstructures was demonstrated on the example of microvenus structures presented in figure 2.4a. The original array, fabricated by 2PP of Ormosil, was used for the preparation of elastomeric mold. For the purpose of illustration SU8 material, containing magnetic nanoparticles, was used as replication material. Due to high scattering by nanoparticles, this material cannot be processed directly by 2PP technique. Prepared PDMS mold is highly elastic and allows the release of produced microvenus structures, without pulling them off the substrate. Thus, despite the fact that the structures are

3D by nature, the UV-micromolding was completed successfully. SEM image of an array of microvenus statues replicated in material containing magnetic nanoparticles is shown in figure 2.4b. Subsequent EDX analysis of the replicated array confirmed content of Co and Sm in the produced structures.

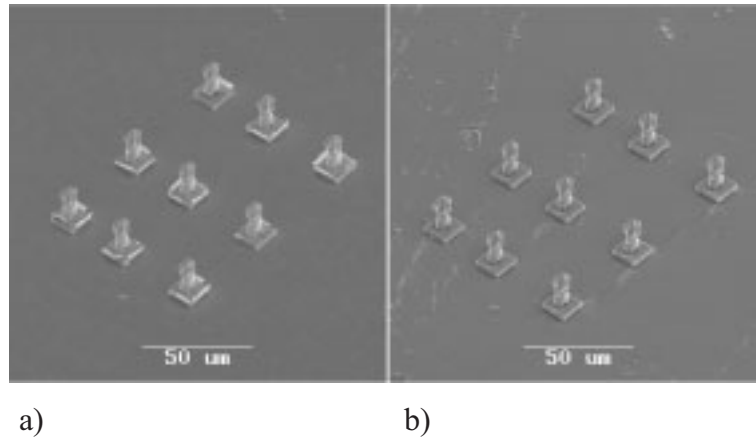


Figure 2.4 Replication of an array of 3D microvenus statues by UV-micromolding. SEM images of: a) original array used for mold preparation; b) array replicated into material containing magnetic nanoparticles.

Using soft lithography, replication of 2D patterns with sizes below 10 nm was previously reported [Sot03]. This value is an order below the best structural resolution currently accessible by 2PP microfabrication. UV- micromolding method allows to obtain large series of samples identical to the original 2PP microfabricated structures. Furthermore 3D structures of certain complexity levels can be reproduced with high precision. Since each 2PP fabricated sample can be used to prepare multiple molds, and each mold can reproduce multiple replicas, manifold increase in throughput is achieved. Therefore, combining 2PP microfabrication with UV-micromolding is a low cost root for fabrication of large series of identical samples. And finally the structures marked by precision of 2PP microfabrication can be obtained from materials which cannot be structured directly by this technique.

3 Results and Discussions

3.1 Investigations of 2PP process

3.1.1 Hybrid Organic-Inorganic Materials for 2PP Processing

Concerning possible variations of material composition and synthesised material properties, hybrid organic-inorganic materials provides considerable advantages. For a fixed material system most often such variations are achieved by adjusting the ratio between the inorganic and organic component. Therefore, it is important to investigate the possible effect of variation in material composition on their processability by 2PP technique.

The two main components of the Zr-based ORMOSIL material employed in this work are Methacryloxypropyl trimethoxysilane (MAPTMS) and Zr-propoxide (ZPO). In order to study the influence of Zr content on materials properties, formulations with different ZPO:MAPTMS ratios were prepared (see section 2.2 for detailed description of material synthesis). The refractive index of these different materials was determined from an m-line prism coupling experiment, using thin material films [MHF00]. By adjusting the Zr content, the refractive index of the composite can be modified, as shown in figure 3.1 The materials refractive index increases linear over a range of 0.04 with the ZPO content. This useful property would, for example, allow the “fine tuning” of a PBG position in photonic crystals in the range of 100nm. The fact that this increase is linear greatly simplifies the material design criteria, as typically such increases are saturating so that the doping concentration becomes very critical. However, in the presented concentration range no such limitation is apparent.

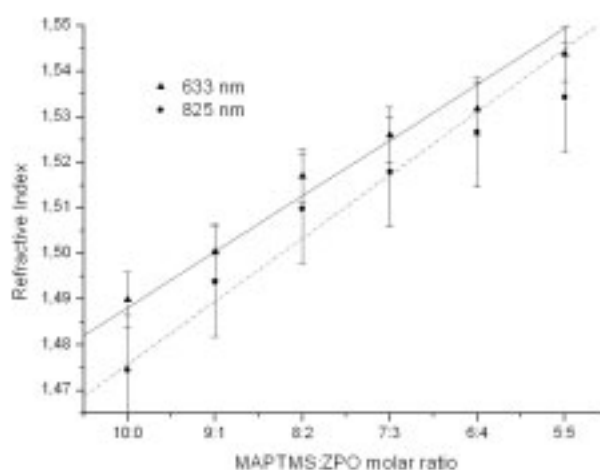


Figure 3.1 Dependence of refractive index of ORMOSIL on the ZPO content measured at two different wavelengths 633nm and 825nm. The lines are guide to the eye, indicating that the dependence is linear in the error range.

In order to study the influence of the Zr content on the structurability of the material by 2PP technique, structures shown in the insets of figure 3.2 were fabricated. Here, first two parallel walls are fabricated using constant laser power. In a second step solitary parallel lines

scanned with different illumination parameters are produced on top these walls. The structural resolution is acquired by measuring the width and the height of 3.6 μm long free-hanging lines. The dependence of the structure width on the average laser power at a constant scanning velocity for different material formulations is shown in figure 3.2. For an average laser power of 22 mW, the voxel height tripled even when only 1 % molar content of the chelated ZPO compound was added to the material. No lines would survive the development process for an average power below 22 mW for material containing no Zr. A further increase of the ZPO content leads to a linear increase of the material sensitivity. The same trend is observed for the values of the structures widths. The value range is somewhat narrower in this case. The smallest structure width obtained with the material not containing Zr is around 260nm and 390nm for material composed out of 30% ZPO.

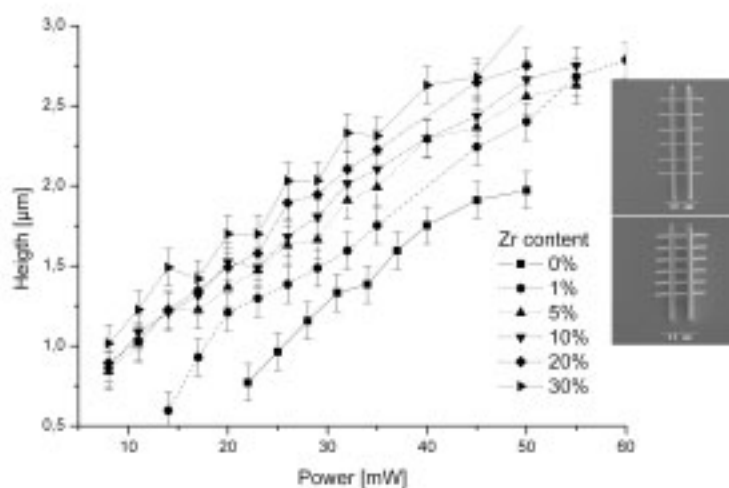


Figure 3.2 Voxel height dependence on the average laser power in relation to the ZPO content in the material (photoinitiator (PI) content is kept at a constant level of 1 %). The inset shows the SEM images of examples of the structures used for free-hanging line height analysis.

In order to clarify the relation of the ZPO content to increasing material sensitivity, the absorption spectra of thin material films were analysed (UV-Vis, Perkin-Elmer). The films were prepared by spin-coating the materials onto quartz substrates and drying them on a hotplate at 100 °C for 1 hour. A few representative spectra are shown in figure 3.3. It appears that the absorption peaks in the spectra of the material that does not contain any Zr essentially originate from the absorption by the photoinitiator (PI) at around 460nm. Next to that, the material with initial 30% ZPO ratio is transparent down to 300nm in the absence of the PI. Remarkably, addition of only 1% PI to the material containing 1% of ZPO, results in a well expressed absorption peak at around 370nm and a new second absorption peak at around 470nm. Furthermore the second peak is enhanced significantly for material containing 30% ZPO and 1% PI. This kind of behaviour indicates that there is interaction between the material matrix and the photoinitiator, resulting in the shift of an absorption peak. The second peak disappears when the materials absorption are analysed in solution, indicating that molecular proximity is required for such interaction.

The PI used in this study is the 4,4'-bis(diethylaminobenzophenone). The benzene is well-known to show three absorption bands located in the far-UV at 184nm, 203.5nm and 254nm [DS87]. In this PI molecule, the presence in the para-position of two strong auxochromes groups, such as ethylamino and carboxy groups, acts as electron donor by inductive and mesomeric effect, respectively. Both phenomena increase the mobility of the electrons located in the aromatic group of the molecule, and facilitate transfer from their fundamental π orbital to excited π^* orbital. The result is a shift of absorption bands toward the higher wavelength (lower energy), commonly known as bathochromic effect. This is confirmed by the fact that the measured full width half maximum of the absorption peak (68 nm) closely corresponds to the expected value, given by the difference between the highest ($\lambda_{\max} = 254$ nm) and the lowest ($\lambda_{\min} = 184$ nm) absorption bands observed in the benzene UV-Visible spectrum (70 nm).

As described above, the absorption band shift toward the higher wavelengths is intimately associated with a bathochromic effect, resulting from the increase of the electronic transfer of the electron of the aromatic group from their π to their π^* orbital. In the present case, the only group that could provoke such effect is the zirconium complex. Indeed, the zirconium atom has a strong polarisability and electropositivity, which lead to a strong reactivity within a nucleophilic environment, particularly in the catalysis of sol-gel reaction [TSM72]. Furthermore, the zirconium atom possesses free 'd' orbitals, that could be used for the formation of complexes with the PI.

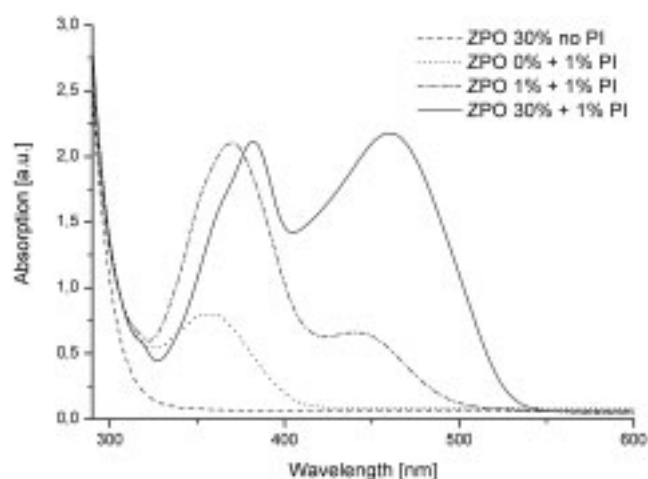


Figure 3.3 Absorption spectra of solid material layers with different ZPO (Zr-propoxide) and PI (photoinitiator) content indicate shift of absorption peak caused by Zr and PI interaction.

The most plausible explanation for the observed phenomenon could associate all these properties. First, in the solid state, the high nucleophilic affinity of the zirconium atom will tend to approach the electron donors groups such as the amino and carboxyl groups contained in the PI. Second, as a result of this proximity, the formation of coordinated bonds is facilitated, the resulting in mutual interactions between both molecules.

Conclusions

The discussed interaction between PI and the polymer matrix is critical as it governs the photosensitive properties of the material, affecting the 2PP fabrication process. To my best knowledge, this is the first study that highlights the bathochromic effect of the Zr atom in presence of PI. Furthermore this effect can be used in order to increase and tune the material sensitivity by using the properties of the polymer matrix instead of increasing the PI content.

3.1.2 Shrinkage of Materials Processed by 2PP Technique

Material shrinkage is one of the fundamental aspects of photopolymerization. It can result in overall photopolymerized structure deformation and cause static material stress. Understanding of processes underlying shrinkage is important for both the design and the process reproducibility of devices [LQY⁺08]. In case of 2PP, volume reduction still has not been fully investigated. Unlike conventional methods, 2PP enables the study of the shrinking processes locally, at the microscale. Here, a simple, straightforward methodology allowing the evaluation of shrinkage is suggested. It can be applied even to materials exhibiting very low shrinkage. It is shown here that for the case of Zr-based hybrid Ormosil material, volume reduction is directly related to the average laser power (irradiation dose) used for the microfabrication and becomes a critical issue near the polymerization threshold. The controllable shrinkage has been exploited to improve the structural resolution further, without compromising the functionality of the fabricated structures.

In order to investigate structure shrinkage dependence on the applied average laser power, woodpile structures supported by a set of columns were fabricated. Columns are attached to the glass at one end, and woodpile structure at the other end. The woodpile structures were fabricated at the scanning speed of 200 $\mu\text{m/s}$, the in-layer rod distance is set to a constant value of 1 μm , and the distance between the neighbouring layers is set to 390 nm. The applied material is a Ormosil prepared with ZPO:MAPTMS ration of 2:8. Final formulation contained 2% of photoinitiator 4,4'-bis(diethylaminobenzophenone) (see section 2.2 for detailed description of material synthesis). Samples are prepared by drop casting the material onto conventional glass coverslips, and prebaking them at 100°C for one hour. The resulting material layer is solid, therefore during the 2PP microfabrication the produced pattern is immobilised throughout the processing step. To remove the unpolymerized material after the 2PP processing, the samples are developed in 1-propanol.

Subsequent solvent removal/drying from the woodpile might result in a structure deformation due to capillary forces. In order to avoid these effects, the critical point drying was applied. 1-Propanol - the original material “developer”, was substituted by ethanol prior to insertion into the critical point dryer chamber (Quorum Technologies, UK).

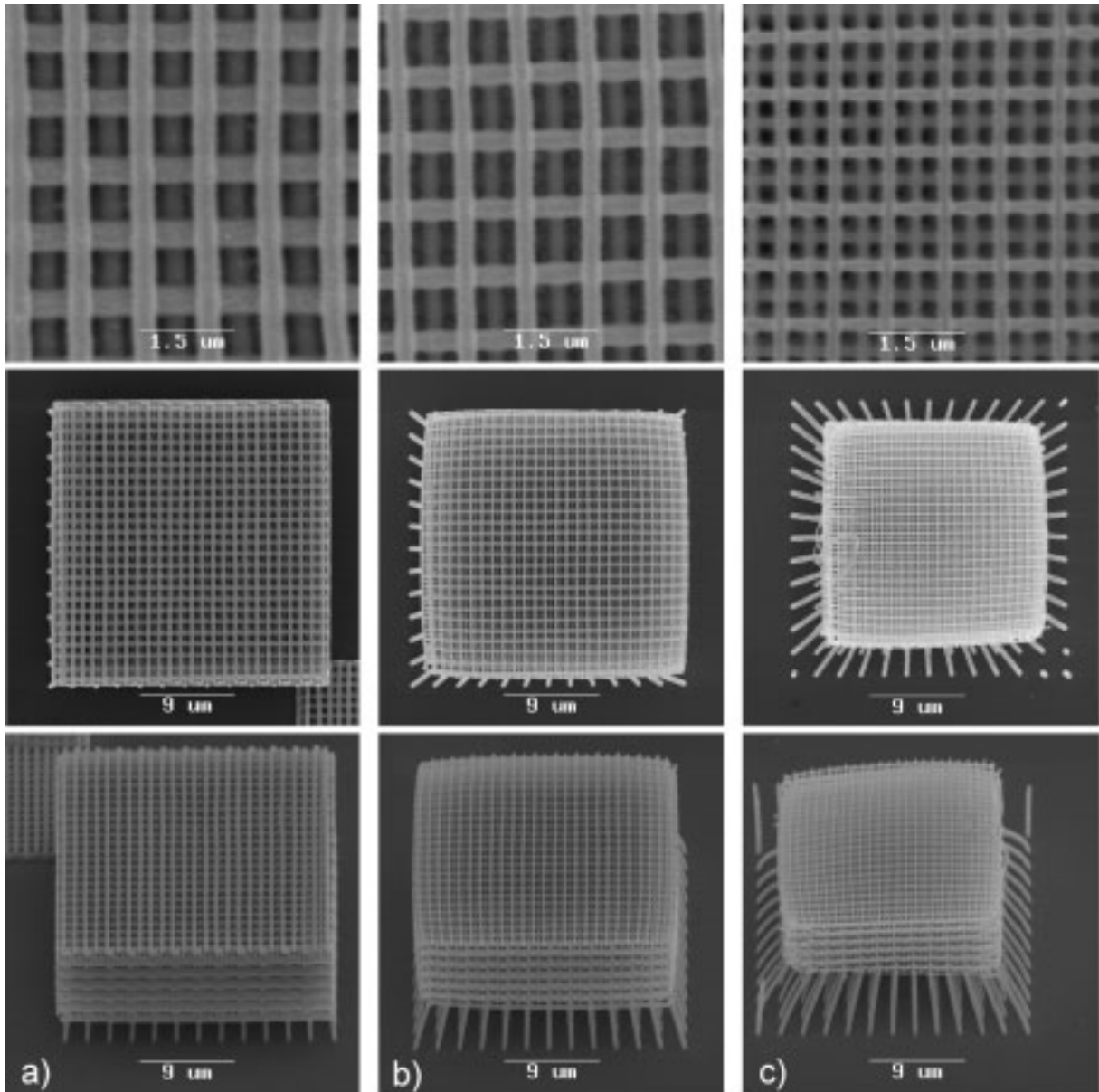


Figure 3.4 SEM images of representative woodpile structures, applied for investigations of shrinkage. From bottom to the top: structure side view, top view, and a close-up view on the upper layers are presented. The applied average laser powers are a) 8.0 mW, b) 5.5 mW and c) 4.5mW. It is observed that the decrease of laser power results in increased material/structure shrinkage, and deformation of the supporting columns.

Woodpile photonic crystals, fabricated at different laser powers, are shown in figure 3.4. Structures, obtained at average laser powers well-above the polymerization threshold, do not exhibit any shrinkage. These structures retain their “original” size, and the vertical support columns show no sign of deformation (see figure 3.4a). However, at lower laser powers material shrinkage results in the overall size reduction of the fabricated structures, while column deformation increases gradually with decreasing laser power (see figure 3.4bc). The woodpile walls remain vertical, suggesting that the shrinkage has progressed to its full extent throughout the structure. By measuring the structure dimensions and comparing it to those of the structure design, the linear strain values were obtained. The shrinkage strain along one direction was evaluated as a change in the structure width ($W_0 - W$) divided by the design

width value W_0 . The strain is therefore defined as $\gamma = (W_0 - W)/W_0$. The dependence of the linear strain on the average laser power is presented in figure 3.5a. The values are given in [%], where 0% designates that no shrinkage has occurred and the structure width is preserved throughout the processing. The maximum shrinkage strain of 18% was observed for the structures fabricated at 4.5mW. Polymerization is also obtained at the average laser powers below 4.5mW. In this case however, the mechanical stability of the structures is so low that they collapse during the development step, and cannot be used for the measurements.

Line width dependence on the average laser power is shown in the figure 3.5b. By assuming Gaussian intensity distribution in the focal plane, the obtained data can be fitted using dependency of a general form [JMS⁺05, SEO⁺03]:

$$d = w_0 \sqrt{\ln\left(\frac{P}{P_{th}}\right)} \quad (1)$$

here d is the width of the photopolymerized line, w_0 is the focal spot size, P is the applied laser power, and P_{th} is the average laser power threshold for polymerization.

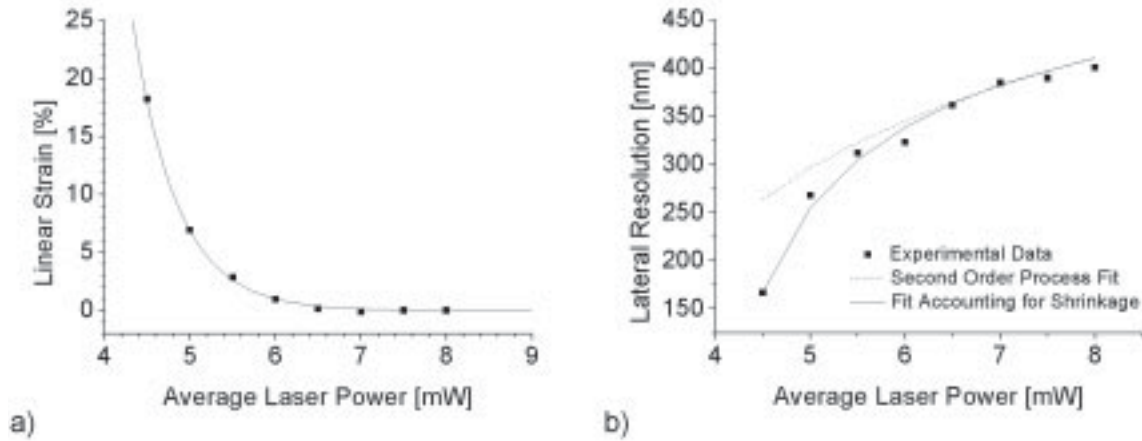


Figure 3.5 Characteristics of the polymerized structures: a) linear shrinkage strain in [%] as a function of the applied laser power; b) line width (lateral resolution) dependence on the applied laser power.

At average laser powers below 5.5 mW, this dependency yields somewhat larger line width values (dashed curve in figure 3.5b) than those obtained experimentally. This fact correlates with the observed illumination dose dependent material shrinkage (figure 3.5a). This disagreement between theory and experiment can be solved by introducing a correction in the form $d \times (1 - A \times \gamma)$ to Eq. (1). When this equation was fitted to the data, (solid curve shown in the figure 3.5b) using the strain values from figure 3.5a, the correction coefficient value $A=2$ was derived. In this case, the maximum lateral strain of $A \times \gamma = 35\%$ was obtained, suggesting anisotropic shrinkage behaviour. The line width reduces more than its length and the coefficient A describes the degree of this asymmetry. Indeed, a closer look at the SEM image in figure 3.4c reveals that the lines are somewhat thicker at the intersections

when compared to a free-hanging line section. Such behaviour is most likely due to a partial arrest of shrinkage provided by the overlap with the neighbouring line. The fact that these features disappear in the woodpiles fabricated using larger average laser power (figure 3.4ab) supports this conclusion.

At high average laser powers, the negligible structure shrinkage of the zirconium-silicon composite under study is due to the double polymerization ability of sol-gels. During the baking of the sample, condensation of the alkoxy groups takes place to form an inorganic matrix. Alcohol, water, and any other solvents present in the film are released from the system at this stage and the unstructured material shrinks. Subsequently, the structuring by 2PP results in the formation of an organic network without the release of any molecules and thus, to no significant distortion of the structures due to shrinkage.

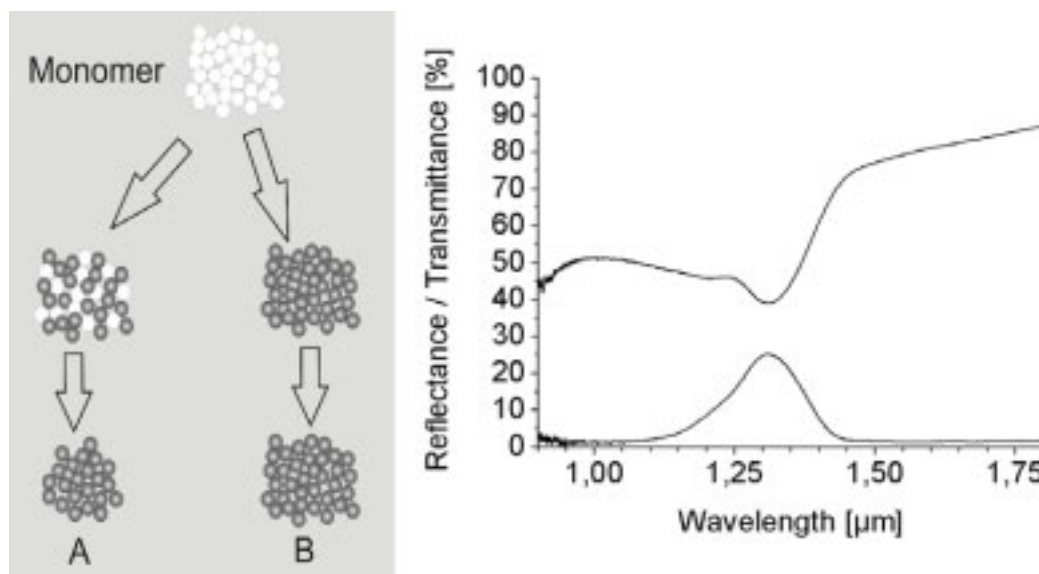


Figure 3.6 a) Schematic illustration of the polymerization process, subsequent developing step and volume shrinkage at low (A) and high (B) average laser powers; b) Optical characterisation of the woodpile structure shrunken to a maximum extent. The reflectance and transmittance spectra obtained by a microscope coupled to FTIR spectrometer, indicate a bandstop at 1330 nm.

At illumination parameters slightly above the 2PP threshold, the photopolymerization does not progress to its full possible extent (cross-linking density). Thus, during developing, the non-polymerized material is removed, leaving a sponge-like material behind. The mechanical support provided by non-polymerized material is therefore eliminated. The collapse of this material at a molecular level results in the structural shrinkage observed at low average laser powers (see figure 3.6aA). On the other hand, for average laser powers above 6 mW the polymerization yield is complete, therefore, the resulting material is mechanically stable and no structural shrinkage is evident (see figure 3.6aB).

Non-uniform shrinkage might destroy the structural periodicity of a photonic crystal, resulting in the degradation of its optical quality. To investigate the integrity and functionality of structures fabricated near the polymerization threshold, their optical properties were analysed by means of microscope-coupled FTIR spectroscopy (Bruker Equinox). Reflectance

and transmittance spectra were measured with a probe beam “perpendicular” to the upper surface of the woodpile. Figure 3.6b shows the spectra obtained for the structure of figure 3.4c. The reduction in transmission and the respective peak in the reflectance spectra indicate a clear bandstop at around 1330 nm. This suggests that uniformity and structure functionality is preserved even for the structures produced at low average laser powers exhibiting the maximum volume reduction. This is achieved by a) a building design which allows the structures to shrink freely and b) using a critical point drying process, to eliminate capillary forces during solvent removal.

Conclusions

Understanding and controlling photopolymerized material shrinkage is very important for 2PP microfabrication of devices demanding high structural resolution. In this section a new, simple methodology, which allows the direct analysis of shrinkage of photosensitive materials on the microscale, was introduced. Furthermore, illumination dose dependent shrinkage was investigated and its influence on the structural resolution was studied. In case of woodpile photonic crystal structures, it has been demonstrated that at sufficiently high laser powers the structures produced do not exhibit any measurable shrinkage. At lower average laser powers shrinkage results in a structural reduction of up to 18%, and line width reduction of up to 35% of the original values. At the same time, the shrinkage uniformity was confirmed by the investigation of the optical properties of the woodpile structures. A stopband at around 1330 nm was measured in the reflectance and transmittance.

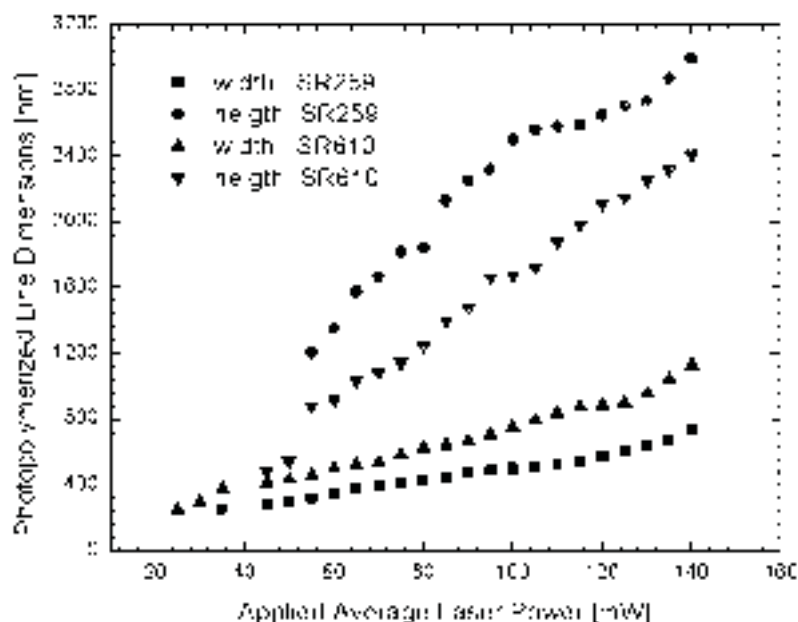
It is clear from this study that controlled shrinkage can be used in order to indirectly “improve” the structural resolution. i.e. to decrease feature sizes. In contrast to other proposed post-processing resolution improvement methods [FCJ⁺04, PLY⁺04], in this case not only the line width but also the whole size of the structure is reduced.

3.1.3 Structuring of Acrylated Poly(Ethylene Glycol)s with 2PP

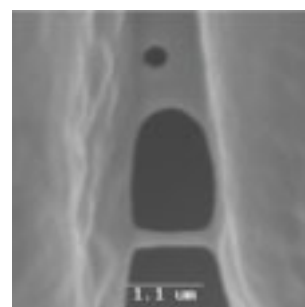
PEG based materials are widely applied in biomedicine and tissue engineering. Most often PEG polymolecules are made photosensitive by adding acrylate or methacrylate functionalities to them. Such photosensitive PEG-based formulations with different molecular weight are widely commercially available. In order to explore the general possibility of 2PP microprocessing of PEG-based materials, commercially obtained photosensitive PEGda formulations were used. Molecular weight of initial material has a great effect on the properties of the final polymer with respect to biomedical applications. Therefore, structurability of PEG diacrylates with two different molecular weights 302 (SR259, Sartomer) and 742 (SR610, Sartomer) were explored (see section 2.2 for details). In previously described hybrid materials, mineral molecular network is established during the sample preparation (gelation) step. Therefore mostly the mobility of the photoinitiator is contributing to the photopolymerization process. In PEG diacrylates photopolymerization

progresses according to the classical scheme, where reacting molecules are forming polymolecules with increasing molecular weight. Due to formation of these large chains molecule mobility is constantly decreasing until the process reaches equilibrium, i.e. polymerization is progressed to full extent [FR93, PB07].

For investigations of structural resolution structures shown in the figure 3.7bc were produced from both materials. In this method two parallel walls support a set of parallel lines, photopolymerized using a different average laser powers. Resulting lines are positioned above the glass. The scanning speed is kept at a constant value of 200 $\mu\text{m/s}$ throughout the experiment. Lines heights and widths dependence on the applied average laser power is presented in the figure 3.7a. Naturally, lower average powers result in smaller illumination doses, and therefore in smaller line dimensions. Due to the intrinsic properties of 2PP technique, these lines have an elliptical cross-section elongated along the laser beam propagation direction.



b)



c)

a) Figure 3.7 a) Obtained line width and height dependences on applied average laser power for both PEGda material formulations; b) an SEM image of a representative structure used for resolution studies; c) an SEM image of a diffusion driven patterns obtained with SR610.

For SR259 material minimum lateral resolution of 200nm is obtained at the average laser power of 27 mW. Similar structure size is obtained in SR610, at somewhat lower applied average power of 22 mW. No lines were obtained at average laser powers below these values. It is observed that lower molecular weight material yields structures with well defined edges and lower surface roughness. From the graph (see figure 3.7a) it is clear that lines with smaller height to width aspect ratios are obtained from SR610 material. Since the intensity distribution in the laser focus does not change substantially, compared to the case of SR259,

this fact can only be attributed to the material property itself. A most reliable conclusion is the higher shrinkage of the material with higher molecular weight, resulting in a more symmetrical line cross-section.

At the upper end of applied average power range 2PP of SR610 material very often resulted in patterns shown in figure 3.7c. The membrane-like structure observed in the upper side of the image does not result from direct irradiation with the laser, since only the lines were scanned. These patterns are manifestation of diffusion-driven polymerization, often referred to as dark polymerization or repolymerization [QLT⁺07, TLQ⁺07]. Free radicals, produced while irradiating walls and separate line between them, diffuse and cause polymerization outside the laser exposed region. As a result the observed structures are created. Most of these membranes are not complete and have some holes, an indication of their poor mechanical stability. Quite often a single line instead of a membrane has appeared. Such lines are also observed in the structures fabricated from SR259 material. Most remarkably the lateral dimensions of such single lines can be as small as 100nm. This fact indicates that measured spatial resolution of structures formed by 2PP is not limited by material and can be further improved.

Conclusions

It has been observed that PEGda based photosensitive materials can be structured by 2PP technique. The structures with feature size well below micrometer can be easily realised. This investigation shows that as the molecular weight of the PEGda increases, the surface of the fabricated structures become rougher and exhibits a less defined geometry. Combination of rigid structures fabricated by two-photon polymerization of low molecular weight PEDda and a high molecular weight PEGda based hydrogels, will allow fabrication of the scaffolds with well controlled mechanical, as well as biodegradability properties. These findings indicate that PEGda can be used for manufacturing of complex designed 3D structures which could be able to control cell proliferation. Application of 2PP technique for microstructuring of these materials brings together a very flexible microstructuring technology and a well known material platform, so addressing a wide area of potential applications in tissue engineering and biomedical fields.

3.2 Applications of 2PP technique in photonics

3.2.1 Fabrication of Microoptical Elements

Conventional methods used for fabrication of refractive microoptical elements, such as lithography or reflow, often lack flexibility when it comes to redefining the element design or implementing new solutions [WRZ⁺06]. In the initial microoptical element array prototype fabrication and testing stage, application of 2PP provides considerable advantages. Many materials that can be structured by 2PP are actually designed for optical applications, and therefore possess superior optical properties. Produced structures exhibit very low surface roughness. During fabrication design of single elements can be freely adjusted directly from CAD input, series of identical patterns can be produced. Patterns fabricated by 2PP technique can be replicated with high confidence using such well developed techniques as soft lithography, injection moulding or electroplating. Therefore the original structure can be microfabricated by 2PP, while replication provides cost-effective route to mass production.

Fabrication of the refractive microoptical elements by 2PP technique was studied on the example of microprisms. Since 2PP microfabricated structures consist out of single voxels, “surface discretization” is one of the practical aspects of that have to be taken into account. Most often 2PP structures are produced layer-by-layer manner, with layers parallel to the substrate. This approach is inherited from stereolithography and by no means is the only one possible by 2PP. Figure 3.8 presents different slicing strategies that can be applied to a prism, single polymerized voxels are represented by ellipsoids. Conventional slicing approach illustrated in figure 3.8b would result in unacceptable step-like surface. In order to improve surface quality one can let the layers overlap, as it is shown in figure 3.8c. On one hand enhancing the voxel overlap in vertical direction improves surface quality; on the other hand the overall fabrication time is increased accordingly. The best solution for the prism slicing is presented in the figure 3.8a. Here the sliced layers are oriented parallel to the prism surface. The overlap of the voxels and the distance between the slices is the same in both cases (figures 3.8a and b), resulting fabrication time will also be similar. Nevertheless the surface will be smoother for the structure sliced parallel to the outer prism facet.



Figure 3.8 Schematic illustrations of different slicing strategies on the example of the microprism (side view).

To illustrate the approach presented in figure 3.8c complex microprisms with facets inclined at few different angles was fabricated. The original design and an SEM image of the fabricated test structure are shown in figures 3.2a and b accordingly. Here a 100x immersion oil objective (NA=1.4) was used for the fabrication. The slicing is performed parallel to the

substrate plane. The parameters used for fabrication are as follows: in-layer scan distance of 370nm, interlayer distance of 300nm, the average laser power of 70mW at the scan velocity of 320 μ m/s. The disadvantage of this approach is readily observed by comparing the quality of the visible facets having four different inclination angles. While most surfaces are high quality and exhibit low roughness, the step-like features emerge as the angle between the facet and the substrate becomes very small (left-most part of the prism in figure 3.9b). This feature is not surprising, since it already appears in the slices of the original design. One way to improve the situation would be to further reduce the distance between the slices, which will result in a proportional increase in fabrication time. A better solution is to use the approach illustrated in the figure 3.8a. Using this approach series of microprisms was fabricated. An example of such 2PP produced microprism is shown in figure 3.9c. Realisation of such structures does not require very high resolution in the vertical direction, which allows the use of 50X microscope objective (0.8 NA) lens instead of high NA optics, to focus the laser beam. The material applied in this case is a standardOrmocore ([www.MR], see section 2.2) formulation. The optimal distance between the sliced layers was found to be 6 μ m, according distance between parallel inlayer scans 350nm. Key performance parameters of the micro-optical elements are the deviations of the surface profile in terms of peak to valley deviation and surface roughness. From the SEM image some conclusions about the surface roughness can be drawn, it is however not easy to analyse the overall conformity of the produced prism with the original design.

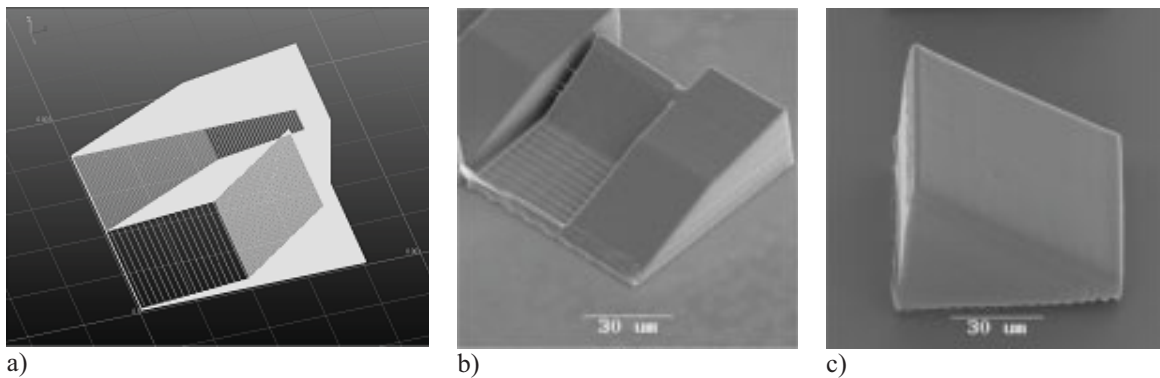
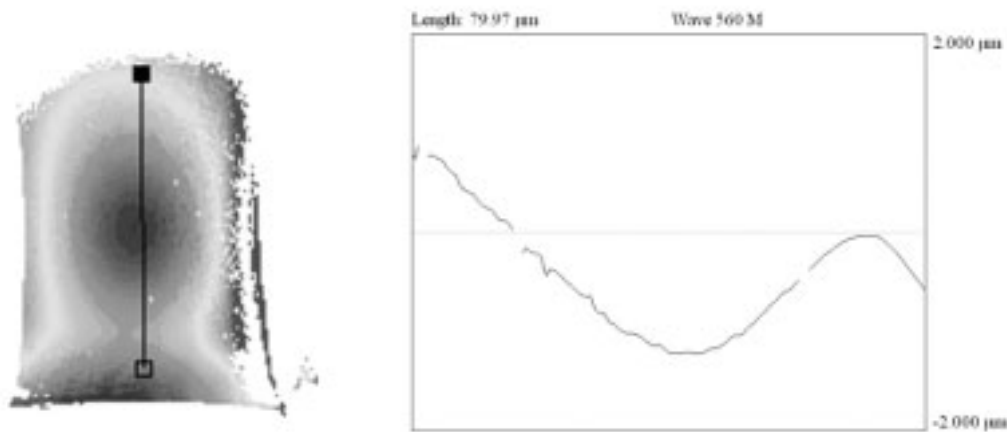


Figure 3.9 Refractive element consisting of microprisms with few different facet inclination parameters a) original design, b) SEM image of according microstructure fabricated by 2PP technique; c) SEM image of single simple microprism fabricated by 2PP technique.

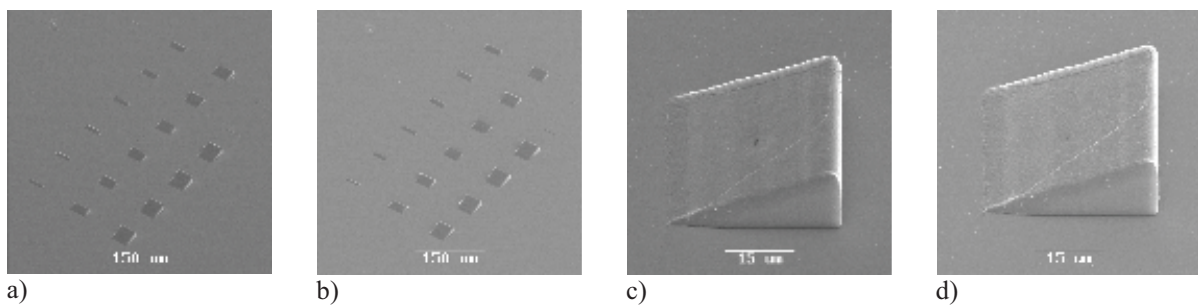
White-light interferometry (ATOS Micromap 570) was used to assess the information on the upper prism facet flatness. The substrate carrying the micro structure was placed on a goniometer in order to adjust the prism surface parallel to the focal plane of the interferometers objective. The results are shown in the figure 3.10, white areas in the plot indicate locations where no height information could be obtained. This happens if the slope angle of the structure becomes too large and the reflected light is therefore not collected by the objective. Observed peak to valley deviation of about 2 μ m (figure 3.10b) is due to shrinkage effects, which is the intrinsic property of applied material. As a consequence the structure is deformed, resulting in an inwardly curved hutch. However, the surface is very

smooth and no influence of the lateral discretization can be observed. Measured roughness value is around 100nm, which fully satisfies requirements imposed on most microoptical elements. The shrinkage issue can be eliminated by applying photopolymers with lower shrinking coefficients. Alternatively precompensation for shrinkage is possible. For this original prisms design has to be adjusted such that after shrinkage the structure will acquire desired shape (see section 3.2) [LQY⁺08].



a) b)
Figure 3.10 Prisms upper facets profile acquired with white-light interferometry: a) colour map; b) height vs position plot along the line indicated in a).

For the fabrication of microoptical elements in the industrial scale high-throughput technologies capable of serial processing are often required. In order to investigate the possibility of replication of microprisms by UV-micromolding, series of experiments involving PDMS as soft stamp material were performed. An array of 40µm wide prism was fabricated by 2PP of Ormocomp, the length and the height of the prisms was adjusted by varying the initial z-position (see figure 3.11a and c). For SEM imaging a 100nm gold layer was deposited on the original sample. The same gold layer serves as anti-sticking surface when it comes to PDMS and Ormocomp separation. A mold from PDMS elastomer was prepared from this structures in accordance to procedure described in section 2.3.



a) b) c) d)
Figure 3.11 Microprism replication by UV-micromolding with PDMS mold: a) original microprism array fabricated by 2PP of Ormocomp; b) according replica in the SU8 photoresist; c) A step like feature on the front facet of the “original” prism results from the removal of a part of 100nm thick gold layer together with PDMS mold; d) this feature is well reproduced in the SU8 replica.

UV-micromolding allows replication of microstructures in a material different from the one used originally. The produced PDMS mold was used to obtain microprisms in SU8 material. SU8 is well known lithographic photoresist widely applied for the fabrication of optical components. Standard photosensitive SU8 formulation (SU8-2050, Microresist Technology [www.MR]) was deposited directly onto the PDMS mold, and placed into low vacuum for 10min in order to remove the solvent from the SU8 and also possible air bubbles trapped at the PDMS/SU8 interface. Later the mold with SU8 on it is pressed against the glass substrate and UV radiation is applied to induce photopolymerization in the SU8. In the final phase the sample is heated at 100°C for 10min to allow complete polymerization of the SU8. Resulting microprism array exactly resembles the original/master one (see figure 3.11b). The exactness of the replication can be evaluated by taking a closer look at the microprism shown in figure 3.11c. Here a part of the 100nm thick gold layer ripped off the microprism resulted in a step-like feature visible on the front facet. This feature is also well reproduced in SU8 replica (see figure 3.11d). UV-micromolding allows exact replication of produced structures. The smallest reported feature size that is reproduced by soft lithography is 8nm [Sot03]. Therefore combining 2PP microfabrication with UV-micromolding is a low cost root for fabrication of large series of identical samples, it provides guidelines for mass produced microoptical components created by 2PP technique.

Conclusions

Regarding the variety of possible surface profiles and the achievable sag heights 2PP technique is superior to laser lithography. Many materials designed for optical applications can be structures by 2PP technique. Key performance parameters of the micro-optical elements are the deviations of the surface profile in terms of peak to valley deviation and surface roughness as well as refractive index gradients. The control of the volume shrinkage of the material is considered as most demanding task for the manufacturing of high quality micro-optical components. In the perspective to mass production of such microoptical elements, it is meaningful to use structures fabricated directly by means of 2PP microfabrication in order to prepare molds for further replication with UV-micromolding.

3.2.2 Realisation of 3D Photonic Crystals

Theoretical Investigations of Properties of 3P Photonic Crystals

Woodpile Structure

The woodpile structure was first proposed in 1994 by Ho et al. [HCS⁺94]. This structure can be derived from diamond lattice, by replacing chains in the diamond by the rods [MT04]. Due to its layer-by-layer architecture, this structure is marked by relative simplicity of experimental realisation by planar semiconductor processing methods [LFH⁺98]. A sketch of a woodpile structure, having rods with elliptical cross-section, is shown in figure 3.12a. It consists of layers of one dimensional rods, with a stacking sequence that repeats itself every four layers. The distance between four adjacent layers is denoted by ‘c’. Within each layer, the axes of the rods are parallel to each other with a distance ‘d’ between them. The adjacent layers are rotated by 90°. Between every other layer, the rods are shifted relative to each other by ‘d/2’. Generally, the resulting structure has a face-centered-tetragonal (fct) lattice symmetry. For the special case of ‘(c/d) = $\sqrt{2}$ ’, the lattice can be derived from a face-centered-cubic (fcc) unit cell with the basis of two rods [HCS⁺94]. Figure 3.12b presents an example of a woodpile structure fabricated by the 2PP technique.

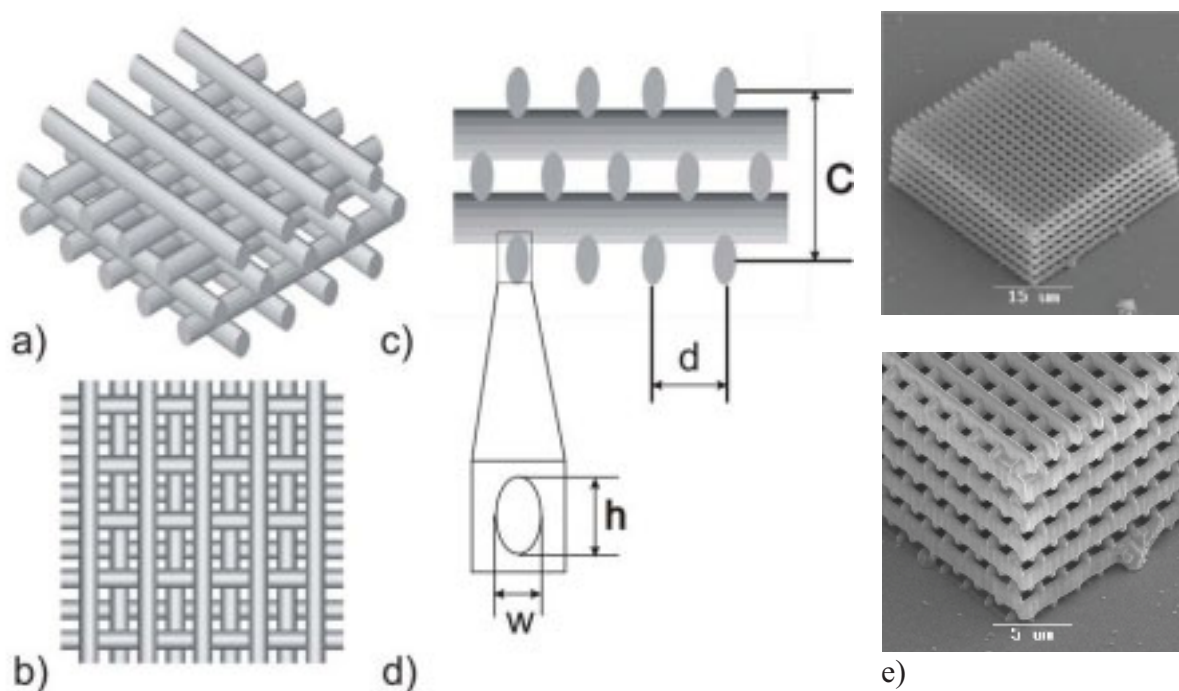


Figure 3.12 Woodpile Photonic crystal: a) schematic representation; b) top view; c) and d) show relevant structural parameters: in-layer rod distance ‘d’, unit cell height ‘c’, spirals cross-sections width ‘w’ and height ‘h’; e) SEM image of woodpile structure fabricated by 2PP technique.

The quality of photonic bandgap (PBG) can be characterised by gap width to midgap ratio, which will be referred to later as relative PBG size. It has been previously reported, that woodpile structure can exhibit a wide complete PBG for both direct (dielectric rods in air,

relative PBG of 18%, found for dielectric filling fraction $\Phi=30\%$) and inverse (cylindrical holes in dielectric, relative PBG of 25%, found for dielectric filling fraction $\Phi=82\%$) configurations [HCS⁺94]. Minimal refractive index contrast of 1.9 is required for the existence of the omnidirectional PBG in the optimum woodpile configuration. In addition such dependencies as filling ratio and 'c/d' ratios have been explored. It was obtained that 'c/d' ratio of 1.4, according to the fcc configuration, exhibits largest relative PBG size, while at the ratios of above 2 the omnidirectional photonic bandgap is closed for described configuration. In addition, since at the time layer by layer stacking approach, associated with complicated alignment procedures was envisioned for the realisation of the woodpile, the effect of layer number was checked. From calculation it followed that even a structure consisting of two unit cells in the vertical direction (i.e. 8 layers) provides attenuation levels that are sufficient for many applications. A few later theoretical studies, confirmed that woodpile architecture is quite immune to many assembly-based fabrication process imperfections (lateral rod misalignment, rod crossing angle deviations) [CN99]. The woodpile structure, possessing PBG in the far-IR, was also one of the first structures to be realised experimentally [LFH⁺98, NTY⁺00].

Woodpile configuration is still one of the most frequently applied 3D photonic crystals geometries. Fabrication of a woodpile structure by 2PP technique has been demonstrated by a few groups [SMM99, SG02, SOC04]. One important advantage of this particular geometry is the possibility of straight forward visual analysis of possible defects and fabrication process failures. In contrast to previously proposed realisation methods, in case of 2PP the cross-section of the fabricated rods is elliptical. This is an intrinsic property of 2PP microfabrication, related to the fact that the two-photon point-spread function is elongated in the axial direction, owing to the finite numerical aperture of the focusing lens. Since every voxel reflects the intensity distribution in the laser focus, it will resemble an ellipsoid stretched along a beam propagation direction (see section 1.3). In addition, the woodpile rods of neighbouring layers overlap to a certain degree in order to provide structural stability. This circumstance contributes to a change in the dielectric filling fraction. Generally, for the 2PP microfabrication of woodpiles, the distances between the rod geometrical axes are defined in the positioning algorithm. And so, while keeping the in-layer rod distance and inter-layer distance fixed, it is possible to independently tune the rods cross-section parameters by adjusting the illumination conditions – laser pulse energy and scanning speed. It is clear that increase in the rods cross-section area will lead to increase in the dielectric filling fraction. The rod obtained by a single scan has typical cross-section height to width (h/w) aspect ratios exceeding 2.5. At the expense of lateral resolution, it is possible to achieve lower aspect ratios by placing two such single-scan rods side by side.

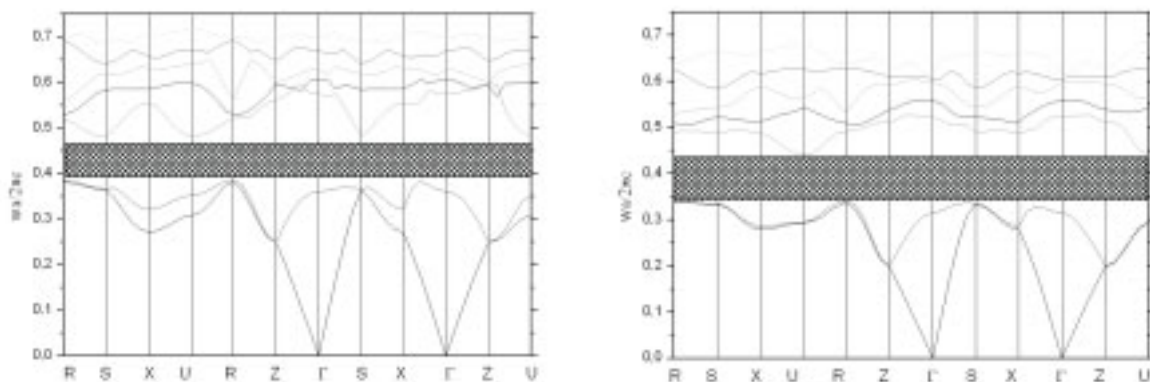
Results of Theoretical Investigations on Woodpile Architecture

In order to study the general possibility of producing woodpiles with omnidirectional PBG by 2PP technique, it is necessary to perform PBG simulations taking into account 2PP fabrication

peculiarities. It is important to notice that photosensitive materials, used for experimental realisation of these structures, have a refractive index values below the ones required in order to obtain structures exhibiting complete PBG.

For the purpose of the illustration, taking into account that the photonic crystals fabricated by 2PP can be interpreted as low refractive index templates for subsequent infiltration with high refractive index materials, the simulations was performed by considering Si as dielectric materials forming the structure. The simulations were performed using the freely available MPB software package, the tool developed by Johnson et al. [Joh02]. From theoretical point of view, the description of light in photonic crystals must involve the solution of Maxwell's equations in a periodic medium. An appealing aspect of Maxwell's equations is that, unlike the complex strongly interacting many particle problem of electrons in a solid, they can be solved exactly [JVF97]. Another fundamental aspect of Maxwell's equations is that there is no fundamental length scale. If the changes in the dielectric function with frequency are ignored, a photonic crystal designed at one length scale will have the same fractional gap as the crystal at any other length scale. The results are therefore presented as unitless normalised frequency ' λ/d ', where 'd' is the in-layer distance between the rods for the woodpile case.

For simulations a photonic crystal consisting of simple geometrical elements is constructed. Approach presented here actually imitates the 2PP process by building a model consisting out of single ellipsoids (representing a single polymerized voxel). The ellipsoids, closely packed along the linear track, produced smooth rods, composing the structure. Using this approach the realistic fabrication approach of 2PP microfabrication process is imitated. This provides us with an important opportunity to study the influence of fabrication factors on the PBG. Each structure is represented by its unit-cell, in which a computational grid with resolution between 16 and 32 pixels/unit-cell-direction was defined. The effective dielectric tensor in each grid point was found by averaging over a mesh of 3 points. A convergence tolerance of $[10^{-7}]$ is used.



a) b)
 Figure 3.13 Band structure obtained for a woodpile photonic crystal with the optimized parameters: a) direct configuration; b) inverse configuration.

The PBG properties of a woodpile structures in both, direct (rods with dielectric constant of $\epsilon_{\text{mat}} = 12.25$ embedded in air $\epsilon_{\text{air}} = 1$) and inverted (ϵ values are interchanged accordingly) configuration, were studied as a function of rod cross-section parameters (width ‘w’ and height ‘h’), in-layer rod distance ‘d’ and interlayer distance ‘C/4’ (figure 3.12a). Here ‘C’ denotes the unit cell height. The unit cells width value is equal to in-layer rod distance ‘d’. First part of this investigation was concerned with optimisation of structure parameters, in order to achieve the largest relative PBG. In the case of direct woodpile structure, a local maximum of the relative PBG was found with parameters equal accordingly to $[w; h; C/4] = [0.3; 0.32; 0.28]$. In this configuration the optimum dielectric filling fraction was found to be $\Phi = 26\%$. According band structure is shown in figure 3.13a. A large complete photonic band gap of 17.7% relative width opens between the second and the third bands centred at normalized frequency of 0.42. For the inverse woodpile structure configuration the maximum relative PBG values were obtained at $[w; h; C/4] = [0.73; 0.67; 0.39]$. In this configuration the optimum dielectric filling fraction was found to be $\Phi = 21\%$. An even wider complete photonic band gap of 25.3% relative width, appears centred at the normalized frequency of 0.39 (see figure 3.13b). The obtained structural parameters for optimal configuration are slightly different from those reported previously for a woodpile with square rod cross-section [HCS⁺94]. Nevertheless, the resulted fill factors and relative photonic bandgap sizes are in close agreement, indicating that the rod cross-section shape alone does not have a great influence on the achievable optical properties.

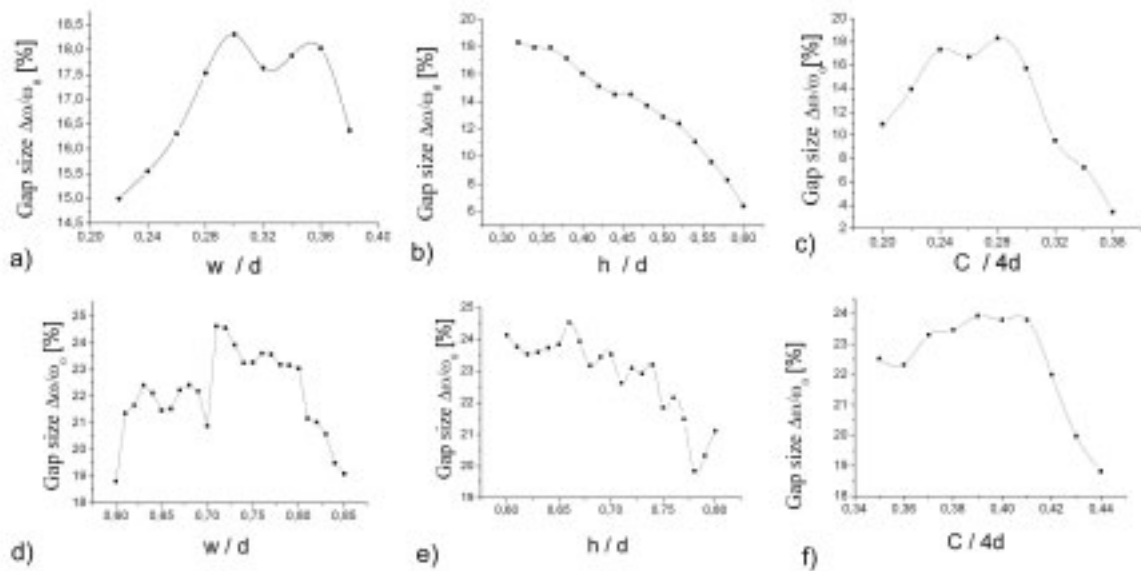


Figure 3.14 Woodpiles PBG size as a function of parameters ‘h’, ‘w’ and ‘C/4’, for direct (a,b,c) and inverse (d,e,f) configurations.

From practical point of view, it is important to examine the robustness and sensitivity of the photonic band gap to small changes in the geometry of the woodpile. The departure of the PBG size from its maximal value as the parameters of the optimal structure are changed is presented in figure 3.14a-c for the direct structure and in figure 3.14d-f for the inverse structure. From left to right the value of PBG size as a function of the rod cross-sections

height ‘h’, the rod cross-sections width ‘w’ and the distance between neighboring layers ‘C/4’ are presented. It is observed that the relative PBG size is much more sensitive to the rod's height than the other two parameters.

Generally, the woodpile structure is described by an fct lattice symmetry. In the special case when $(C/d)=\sqrt{2}$, the lattice can be derived from the unit cell of an fcc (face centered cubic) lattice with a basis of two rods. The fcc configuration of the woodpile has been conventionally considered to have the largest PBG. However, results presented in figure 3.14c reveal that this statement is not valid for the case of elliptic rods. Here, distance between adjacent layers of 0.35 as in the face center cubic case, leads to small PBG of just 5%. The distance between adjacent layers that maximizes the PBG is 0.28, which correspond to ratio $(C/d) = \sqrt{1.12}$.

In the inverse woodpile case, the optimal ratio between the unit cell height and length is $(C/d) = \sqrt{2.43}$ and the optimal distance between adjacent layers is $C/4=0.39$. In this case, the PBG is less sensitive to variations in the distance between adjacent layers as can be seen in figure 3.14f, and the fct configuration gives still notably large relative gap ratio.

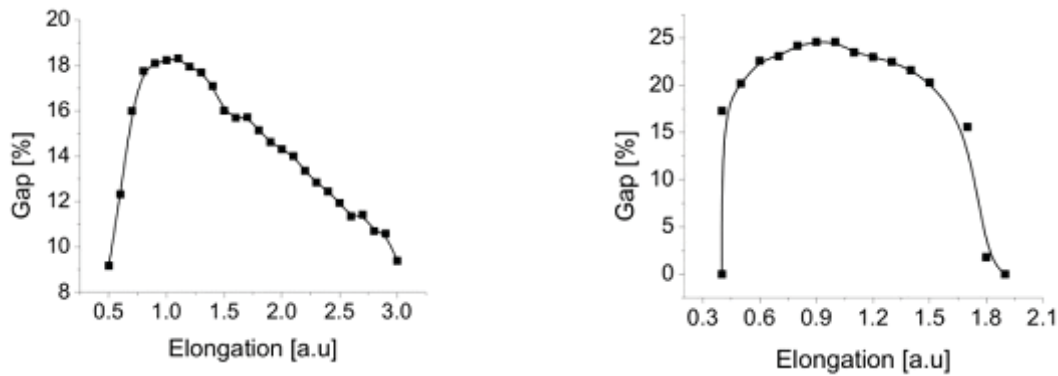


Figure 3.15 Woodpiles PBG size as a function of rods cross-section elongation parameter ‘h/w’ for direct (a) and inverse (b) configurations. The plots present the largest possible PBG size for a given elongation ratio.

As it was mentioned, the rods produced by a 2PP technique obtained with a single scan have a typical cross-section length to height (w/h) aspect ratios exceeding 2.5. This feature is due to the intensity distribution in the focal point and is an intrinsic property of the 2PP technique. Figures 3.15 a and b show the effect of the elongation on the PBGs for the direct and inverse structure, respectively. In order to obtain the largest possible PBG size for a given elongation ratio, the rest of the parameters were varied. It appears that the PBG size is less sensitive to increase in the elongation than to a decrease. The increase of elongation value from 1 to 3 (which is typical for 2PP microfabrication) leads to the PBG drop by 50% (for comparison the same effect is obtained when the elongation is decreased to 0.5). The inverted structure is more sensitive to variation of elongation. Here, the complete PBG is closed in when the elongation value exceeds 2. The layers spacing has major affect on the PBG size in all these cases. It was found that for a moderate elongation values (between 0.75 and 2) the

largest complete PBG is achieved when the layers spacing is 0.28 for direct and 0.4 for inverse structures, respectively.

Photonic Crystals Constructed from Spiral Elements

The circular spirals based face-centre-cubic (fcc) lattice photonic crystals, proposed by Chutinan and Noda [CN98] in 1998, is an example of a structure with optical properties superior to those of a woodpile. Three different configurations consisting of spiral-shaped rods, arranged in simple-cubic, face-centered-cubic, or body-centered cubic lattices were proposed. The fcc-based structure was predicted to exhibit maximal relative complete gap of the 28% when fabricated in silicon ($n=3.5$) [CN98], which is the second largest bandgap predicted to-date. The idea of spiral configuration has emerged from connecting the lattice points of structures known to possess a photonic band gap, such as diamond or woodpile. In the same manner spiral lines can be found in all of the known three dimensional photonic crystals structures [MT04]. Figure 3.16a shows schematic structural representation of such structure. Each spiral is characterised by its pitch ‘C’, diameter ‘D’, and lateral lattice period ‘a’ corresponding to the double distance between two neighbouring spirals. Parameters ‘C’ and ‘a’ correspond accordingly to the height and the width of a unit cell. Two further parameters, width ‘w’ and height ‘h’, describe the cross-section of spirals rods by a plane coinciding with the spiral axis. The fcc configuration is achieved by shifting adjacent spirals in by half a period as they wind in the vertical direction. Figure 3.16b presents an example of spiral photonic crystal fabricated by 2PP technique.

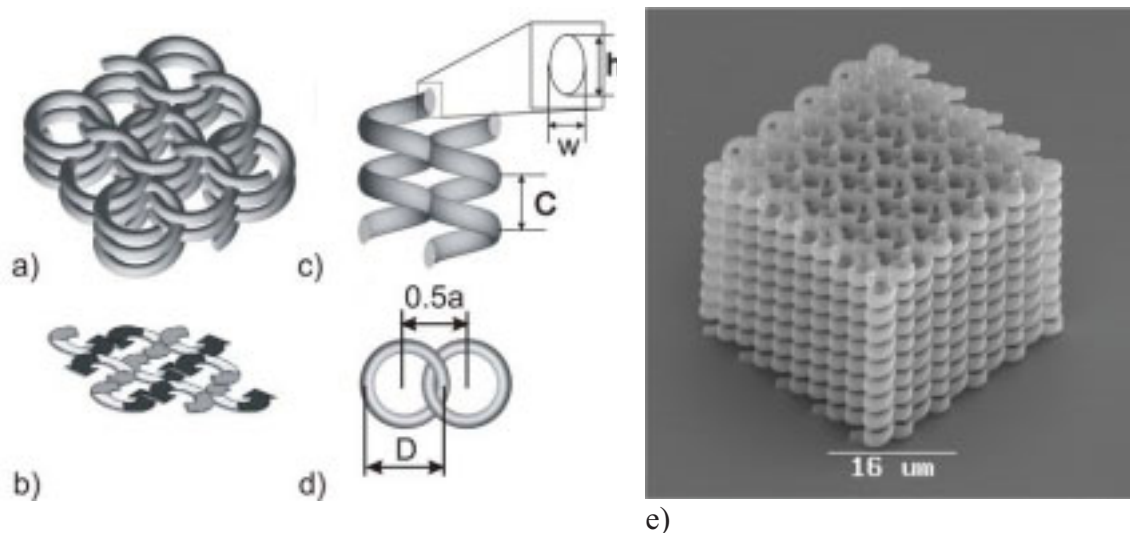


Figure 3.16 Spiral photonic crystal: a) Schematic representation; b) spiral termination pattern in the upper/lower structure facet illustrates the phase shift between the neighbouring spirals composing the structure; c) and d) show relevant structural parameters: spiral pitch ‘C’, diameter ‘D’, distance between the spirals ‘a’, spirals cross-sections width ‘w’ and height ‘h’; e) SEM image of a spiral structure fabricated by 2PP microfabrication.

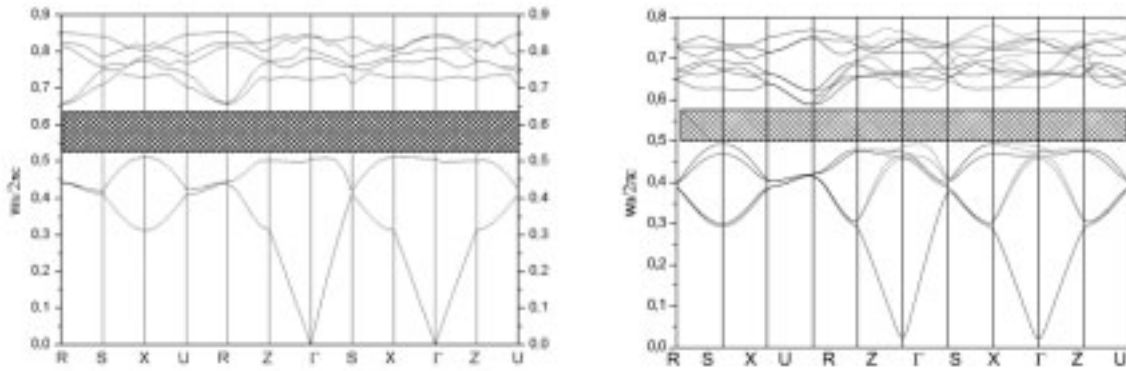
It was reported that the structural parameters that would yield the largest gap is obtained when the rods have a diameter of $0.22a$ (here “a” is the lateral lattice constant), and

the spirals have a diameter of $0.32a$ and a pitch of ‘ a ’ [CN98]. The realisation of this structure, is quite complex, mainly due to the half a period shift between the adjacent objects. As a result, despite its attractiveness, the structure received minor attention since its proposal.

Results of Theoretical Investigations on Spiral architecture

In order to provide guidelines for fabrication of the fcc spiral structure with a complete PBG by 2PP technique, it was investigated how the structural proportions can be altered without destroying the complete PBG.

The fcc spiral structure has five variable parameters: the spiral’s diameter, the spiral’s pitch, the rod’s width, the rod’s height and the distance between adjacent spirals (see figure 3.16a). Here, the parameters were normalized in respect to the lattice constant ‘ a ’, which is twice the distance between adjacent spirals.



a) b)
Figure 3.17 Bandstructure obtained for optimum parameters of the spiral photonic crystal in (a) direct and (b) inverse configurations.

The band structures were calculated using the MIT’s Photonic Bands (MPB) tool [Joh02], the applied simulation tool parameters are the same as the ones used for the woodpile photonic crystal. From the simulations it followed that, in the case of direct configuration, i.e. dielectric structure and air background the structure with the largest relative complete PBG was obtained when the spirals were made of rods with the width of $0.2a$, height of $0.25a$, and had a diameter of $0.4a$ and a pitch length equal to ‘ a ’. In the parametric space the structure is represented by the 4 element vector $[w, h, D, C] = [0.2a, 0.25a, 0.4a, a]$. The structure has an Φ of 20%, i.e. the dielectric material constitutes 20% of the total volume. It has a complete PBG between the second and the third bands with the relative width of 24.6%. The gap is centred at the normalized frequency of 0.58 (see figure 3.17a). In the inverted configuration, i.e. hollow spirals in the dielectric materials, the maximal relative complete PBG was found when $[w, h, D, C] = [0.5a, 0.55a, 0.35a, a]$, corresponding to a Φ value of 22%. The relative complete PBG was 25.1%. The gap in this case is centred at normalized frequency of 0.54 (see figure 3.17b). Despite the differences between the optimal structure parameters obtained

here and the ones that reported previously [CN99], the resulted values of Φ in both cases are the same, while the sizes of the maximal relative bandgaps differ by about 3%. This minor deviation might be due to difference in the specifications that were used in calculation. However, no evidential conclusions could be made on this matter, since we did not have an access to the method that was used in [CN99].

The size of the PBG was found to be more sensitive to changes in the relative spiral diameter and less sensitive to changes in the relative spirals cross-section dimensions, (see figure 3.18(a-c)). In fact, the complete PBG width is reduced by 50% when the spiral diameter is decreased by only 25%. Here a single parameter was varied each time, while the others are fixed to their optimal value. Changes in the spirals cross-section width have in general stronger impact on the bandgap size than changes in its height. In order to centre the PBG at the $1.5\mu\text{m}$ wavelength the lattice constant should be $0.9\mu\text{m}$. The structure dimensions would be then $[w, h, D, C] = [0.17\mu\text{m}, 0.22\mu\text{m}, 0.35\mu\text{m}, 0.9\mu\text{m}]$.

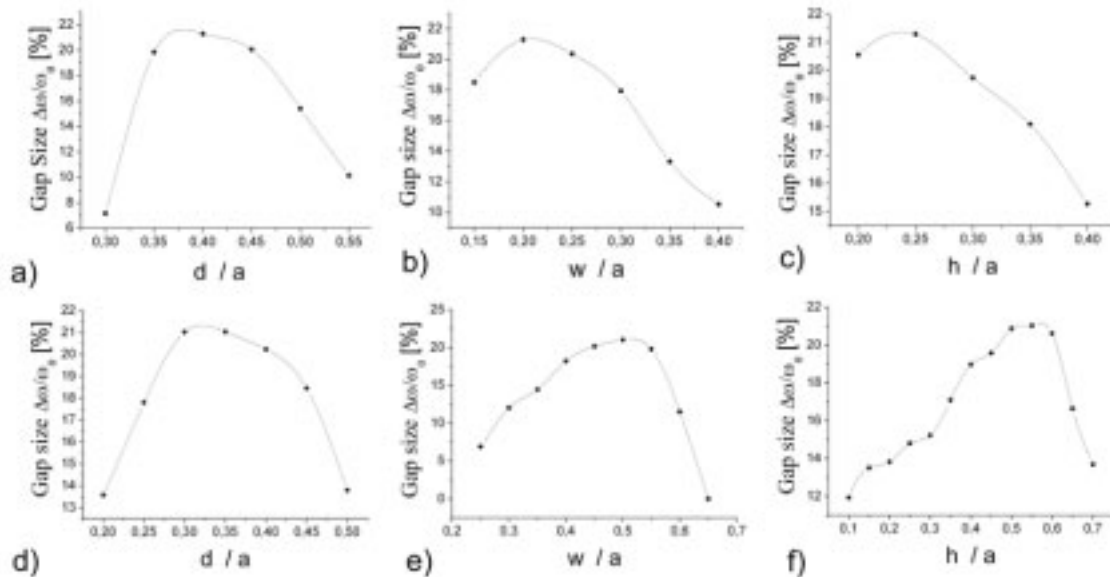


Figure 3.18 Spiral photonic crystal relative PBG size as a function of parameters ‘d’, ‘w’ and ‘h’, for direct (a,b,c) and inverse (d,e,f) configurations.

For inverse configuration the spirals cross-section width has a major impact on the size of PBG. In fact for the relative widths slightly above 0.6 the PBG is fully diminished (see figure 3.18e), which is not surprising since in this case the Φ is increased dramatically.

Results on Experimental Realisation of 3D Photonic Crystals and Characterisation of their Optical Properties

The fundamental attribute of photonic crystal concept is the possibility to ‘design’ a structure with desired optical properties. Following from equation Maxell scaling, the position of the PBG can be adjusted by proportionally varying the structure dimensions. Flexibility of 2PP technique provides opportunity to precisely adjust and define the optical properties of fabricated photonic crystals.

Optical characterisation of fabricated photonic crystals is performed by means of the Fourier transform infrared spectrometer (FTIR, Bruker Optics, Equinox) spectroscopy along a certain direction in a crystal. The photonic crystals presented in the following sections are fabricated from polymeric photosensitive materials. The refractive index of these materials does not exceed $n=2$, therefore no complete PBG is expected for the directly fabricated structures. Nevertheless, it is possible to characterise the optical properties of such structure by measuring the bandgaps, which open along a certain direction in a photonic crystal, referred further to as bandstops. For a woodpile the measurement is performed along the layer stacking direction (coinciding with the ΓX vector, see figure 3.13). Due to the “forbidden frequency range” effect of PBG, the spectra shall exhibit the dip in the transmission and an according peak in the reflection spectra. The reflection spectra are normalised to reflection from a silver mirror, and the transmission spectra are normalised to transmission of glass cover slip on which the structures are fabricated.

Characterisation of Woodpile Photonic Crystals Fabricated by 2PP Technique

For a woodpile photonic crystal with fcc symmetry, the ratio between the in-layer rod period and a unit cell height is fixed to $c/d=\sqrt{2}$. According distance between the adjacent layers is $dz=(1/4)*c=(1/4)*d*\sqrt{2}$. Here this ratio is varied by introducing a scaling factor ‘s’, i.e. $dz=s*FCC$ denotes $dz=s*(1/4)*d*\sqrt{2}$.

Dependence of a Bandstop Position on the Woodpiles Unit Cell Dimension

It was discussed in the previous sections that adjusting the lattice constant is one of the most straight-forward and intuitive methods for tuning the central frequency of a PBG.

Figure 3.19 presents the results of the FTIR measurements on a woodpile structures fabricated by the 2PP technique of Ormosil material containing 1% PI (see section 2.2). The in-layer photonic crystal period ‘d’ was varied between 1.2 μm and 1.8 μm . The inter-layer distance was chosen to be 0.6*FCC, therefore here the unit cell “width to height” ratio is preserved for all structures and essentially the dimension of the unit cell is adjusted. The theoretically predicted bandstop position for such structure is at 0.66 (normalised frequency). At scanning speed of 200 $\mu\text{m/s}$, the applied laser power was in the range 8-12mW, adjusted so, that the dielectric filling fraction for structures with different in-layer rod distance is approximately constant.

FTIR spectra, obtained for the fabricated structures, indicate two clear bandstop positions. In accordance to Maxwell equation scaling - the central frequency of a bandstop is shifting to shorter wavelengths as the unit cell size is reduced. In addition, the spectra show appearance of the higher order bandgaps for all the structures (e.g. at 1.5 μm for $d=1.6\mu\text{m}$), indicating the high quality of the fabricated samples.

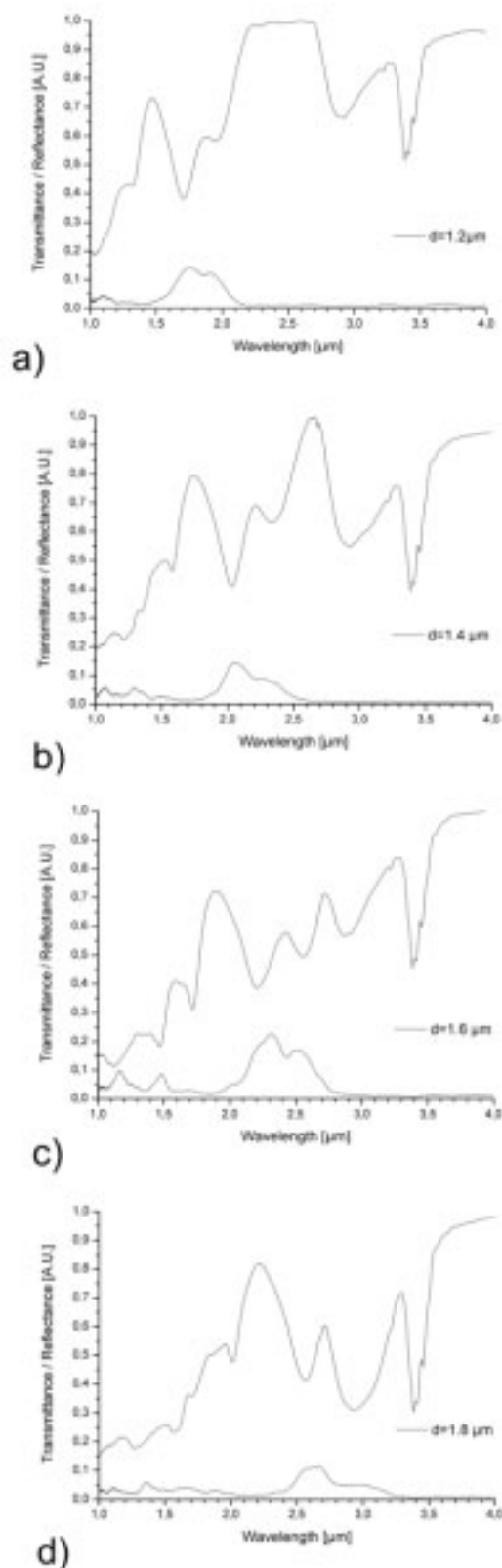


Figure 3.19 Measured reflection/transmission FTIR spectra of the fabricated woodpile structures. The central stopband position is adjusted between $1.7\mu\text{m}$ and $2.7\mu\text{m}$ by variation of the lattice constant 'd'.

The transmission suppression of up to 60% is achieved in fabricated structures. Since the reflection peak measurement is much more sensitive to scattering inside the photonic crystal and on the woodpile-glass / woodpile-air interfaces, the reflection peak amplitudes do not exceed 20%. The absorption bands at around $3\mu\text{m}$ and $3.4\mu\text{m}$ originate from the absorption of the material (C-H stretch vibrations in the polymer network), as has been confirmed by measurements on the flat, unstructured layers. The non-structured material is fully transparent in the range of 550nm to 2700nm (see figure 3.3 and figure 3.25). The relative drop in the transmission values at higher frequencies (to the shorter wavelength side from the bandstop dips) is associated with the known effect of light coupling to higher modes in the photonic crystal structure [DWL⁺05].

The values for central stopband frequency obtained from the theoretical simulations are accordingly $1.8\mu\text{m}$, $2.1\mu\text{m}$, $2.4\mu\text{m}$ and $2.7\mu\text{m}$ for the spectra shown in figure 3.19 a)-d). Compared to these values, the observed central position of the measured reflection peak maxima and transmission dip minima is blue shifted by around 100nm . The observed blue shift, and splitting of the absorption and transmission peaks (e.g. for the period of $1.6\mu\text{m}$ this splitting occurs around $2.4\mu\text{m}$) can be explained by taking a closer look at the experimental setup used for the FTIR transmission measurements. In order to focus the beam to the size of the fabricated photonic crystal in a wide range of measured wavelengths, a Cassegrain reflective optical assembly is used. In contrast to the ideal case, where collimated measuring beam is perpendicular to the surface of the structure, this assembly provides illumination of the structure with a hollow light cone having an acceptance angle between 15° and 30° . Previous studies on

3D photonic crystals have shown that scattering of the measuring beam entering the photonic crystal at a large angle leads to the reflection peak splitting and a blue shift of its central position [Rom01, Rom07, DWL⁺05]. Theoretical simulations have also confirmed these observations [LR07, DWL⁺05].

Optimisation of the Inter-layer Distance of a Woodpile Structure

Conventionally, close to fcc configuration is considered to be the optimal one for the woodpile photonic crystal. Variation of inter-layers distance in the vertical direction is another way to adjust the relative width of PBG. In case of 2PP microfabrication, reducing the inter-layer distance results in a higher overlap between the neighbouring layers, and therefore has an additional effect of increased dielectric filling fraction.

The fabrication conditions as well as the in-layer rod distance ($d=0.9 \mu\text{m}$) are kept constant for all the structures. At the scanning speed of $200 \mu\text{m/s}$, the laser power was kept at 4.5mW (PI concentration in the material is 2% in this case). Each crystal consisted from 24 layers.

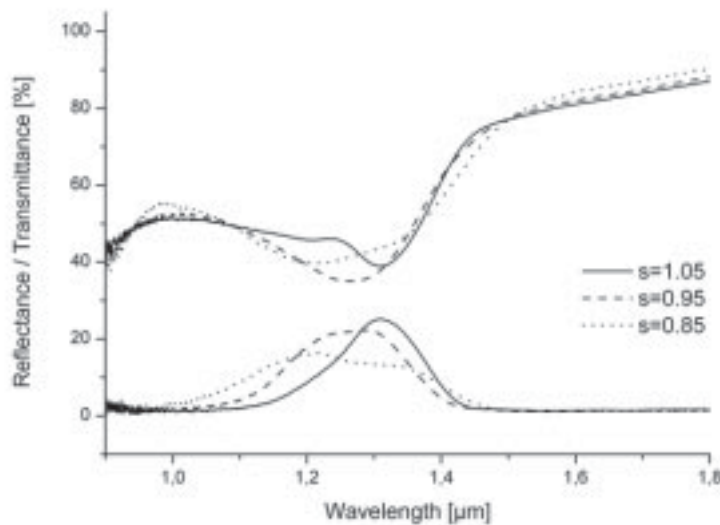
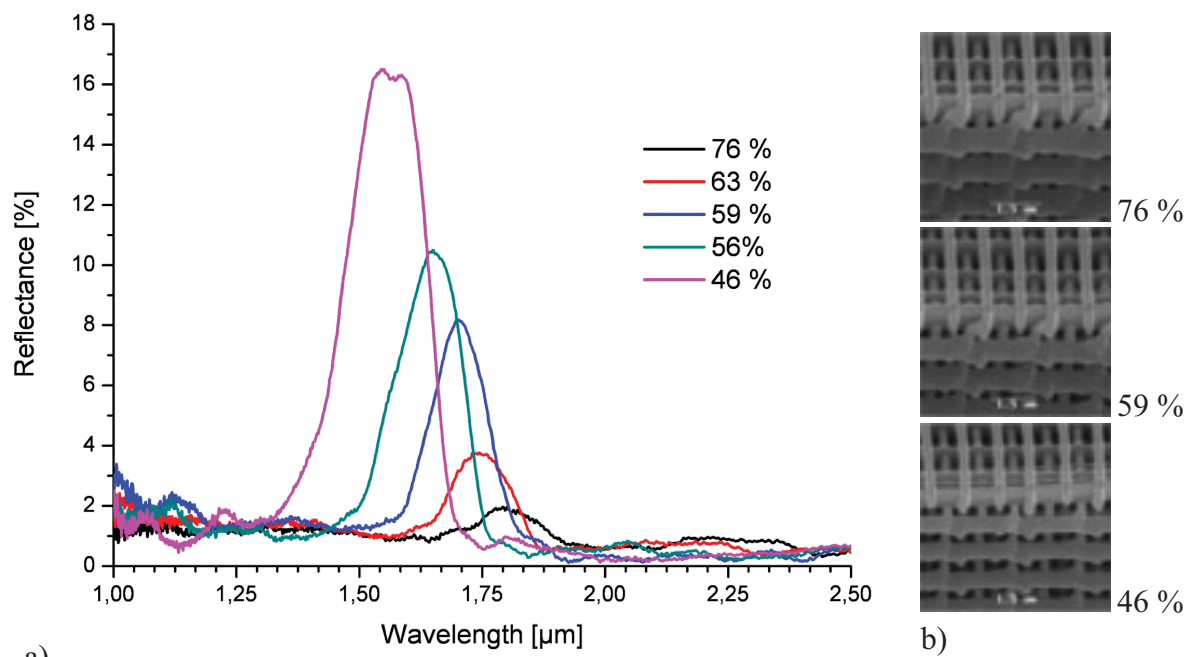


Figure 3.20 Measured reflectance/transmittance spectra of the fabricated woodpile structures with varying distance between the layers.

“Stretching” the woodpile along the vertical direction leads to increase in reflection peak amplitude and simultaneous increase of absorption peak (see figure 3.20). At the same time the central frequency of the bandstop is shifted to longer wavelengths. It is also observed that the splitting of the spectra disappears as the quantity of ‘s’ is increased. Similar behaviour, at bandstop positions around $2 \mu\text{m}$, has been reported previously (also see [SG02]). The maximum reflection peak amplitude is obtained for the s value of 1.05, while the most expressed transmission dip is found for $s=0.9$.

Effect of the Dielectric Filling Fraction Value on the Quality of the Bandstop

As it has been described in the theoretical section, dielectric filling fraction has a great effect on the size and the position of the PBG. It is therefore important to investigate the effect of dielectric filling fraction (Φ) variation during 2PP microfabrication of realistic microstructures. In 2PP microfabrication, Φ is directly adjusted by the illumination parameters (scanning speed, pulse energy), since they are in direct relation to polymerized voxel size (see section 1.3), i.e. the woodpile rods cross-sections dimensions. Figure 3.21 shows the reflection spectra for woodpile photonic crystal structures having different Φ values. The in-layer photonic crystal period is fixed at $1.0\mu\text{m}$ and the distance between the layers in z-direction corresponds to an FCC configuration. Each woodpile consists of 32 layers. The Φ is changed by varying the applied laser power in the range 5-7mW in steps of 0.5mW. The scanning speed is kept at constant value of $200\mu\text{m/s}$. The spectra indicate the clear bandstop positions, with central frequency shifting to shorter wavelengths as the Φ is decreased to 46%. Simultaneously, the reflectance is increased eightfold when compared to that measured with a structure having an Φ value of 76%.



a) Figure 3.21 a) Reflection spectra for woodpile structures with different fill factors; b) SEM side/top view images of according woodpile structures with Φ values 76%, 59% and 46%.

Photonic structures with Φ values below 46% were found to be too weak to survive. This is connected to the fact that further reduction of feature size for this woodpile dimensions results in structures that do not possess sufficient mechanical strength and collapse during the developing step. Therefore here we approach the lower limit of this technique when using current materials at the described structural parameters.

Effect of the Number of Woodpile Layers on the Quality of the Bandstop

Although for the case of 2PP microfabrication increasing number of layers does not present any significant challenge. For considerations of practicality, with prospective on other materials and infiltration methods, it is interesting to know what the minimum number of layers a crystal should contain in order to still exhibit the considerable photonic bandstop effect. Figure 3.22 illustrates the measured reflectance spectra for woodpile structures containing different number of layers in vertical direction. The number of layers is changed by the multiples of 4, i.e. a new unit cell is added every time in the vertical direction. The rest of the relevant structure parameters are kept constant: in-layer-period is $1\mu\text{m}$, the distance between the layers in the vertical direction corresponds to 1.05FCC , and the $\Phi = 46\%$. The fabrication parameters are set to 5mW for the average laser power and $200\mu\text{m/s}$ for the scanning speed. To avoid possible effects from structure termination and to make sure that none of the layers is truncated by the glass substrates on which the crystal is attached, the structures were fabricated above the glass substrates supported by a set of poles. As it was discussed in the section 3.1.2, this feature also helps to avoid possible anisotropic structure deformation due to shrinkage, and, which is more critical in this case, partial photonic crystal truncation by the carrying substrate. An array of such “free-standing” structures containing different number of layers were analysed by FTIR.

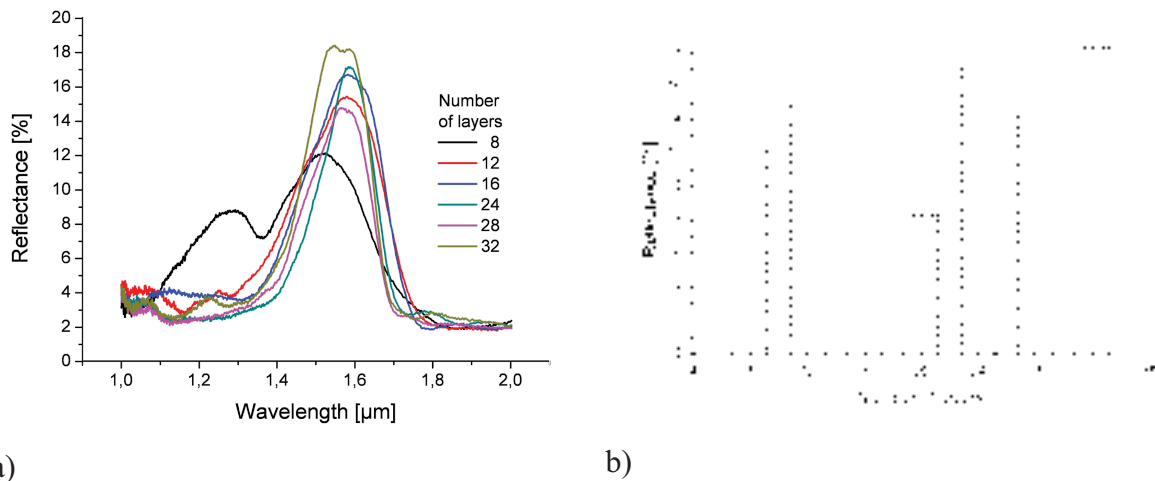


Figure 3.22 a) Reflection spectra for woodpile structures with different number of layers; b) amplitude of reflectance peak vs number of unit cells.

It is observed that already a structure containing only 8 layers shows almost 12% reflectance peak at the position of the bandstop. In this case a second peak appears at the shorter wavelength, this feature manifests presence of a higher order bandstop. Evolution of reflectance peak amplitude vs number of layers is presented in the figure 3.22b. Starting with 16 layers and up the reflectance is increased mere 3%. The sudden drop in reflectance for the structures with 20 and 28 layer, could be explained after detailed SEM analysis of the sample. It revealed that due to some deformation of support structure the upper facet of these

structures were not exactly parallel to the sample surface. As a result the incidence angle of testing beam deviates from the optimal value and results in reduced transmission signal.

Characterization of Spiral Photonic crystals fabricated by 2PP technique

Optimisation of the Dielectric Filling Fraction Value

A few factors have direct influence on the size of PBG, one of them is the dielectric filling fraction (Φ) determining the ratio of air to dielectric material in a photonic crystal. Spiral structures are fabricated by “pinpoint” illumination, where every single voxel is produced separately.

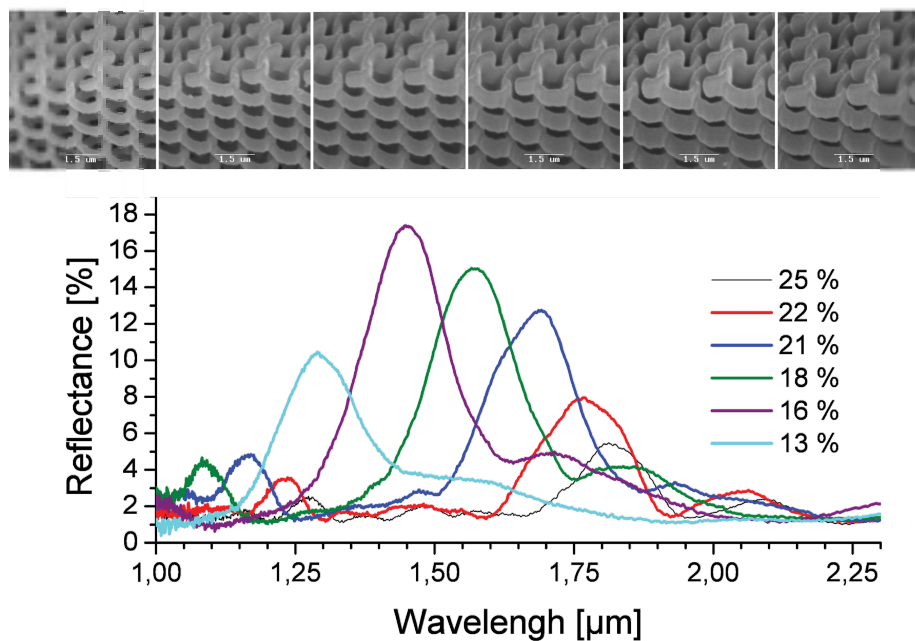


Figure 3.23 Measured reflection spectra of spiral photonic crystal structures with different dielectric filling fractions (Φ). Inset at the top shows according SEM images of the structures, from left to right: 13 %, 16 %, 18 %, 21 %, 22 %, 25 %.

During 2PP microfabrication of photonic crystals with fixed structural parameters, the value of Φ is adjusted by setting the illumination parameters, since they are in direct relation to polymerized voxel size, i.e. the spirals cross-section dimensions ‘w’ and ‘h’. The relevant fabrication parameters in this case are the applied average laser power and the illumination duration. In order to adjust Φ , average laser power was varied in the range 5.5 mW to 3mW, while the illumination duration is fixed to 1 ms. Each spirals parameters are fixed to have a radius $r=0.65 \mu\text{m}$ and distance between the neighbouring spirals of $d=1.2\mu\text{m}$, i.e. the neighbouring spirals overlap to a certain extent. Each structure consists of 18×18 single spirals completing 5 revolutions in the vertical direction. The pitch size value is set to 1200 nm. Supporting structures are provided to each spiral in order to avoid anisotropic deformation caused by possible shrinkage of the whole photonic crystal (see section 3.1.2). Figure 3.23 presents transmission spectra for spiral photonic crystal structures characterised

by different Φ values. The according side/top view SEM images of analysed structures are shown in the inset at the top of the figure. Compared to the case of woodpile photonic crystals, structures with much lower Φ values can be experimentally realised for spiral configuration.

Naturally, variation of Φ also influences the central position of the measured bandstop - the position of the reflection peak is shifted between 1.3 μm and 1.8 μm for fabricated structures. Decrease in Φ value result in a blue shift of central bandstop position.

The variation of Φ , directly influences the amplitude of the reflection peak, i.e. the quality of the bandstop. It is observed that an $\Phi = 16\%$ represents an optimum value for direct configuration spiral photonic crystal, characterised by a maximum reflectance of $R=17\%$.

Tuning the Bandstop Position by Adjustment of Spirals Pitch Size Value

The bandstops measured along the vertical direction are highly sensitive to the variation in spirals pitch size. Figure 3.24 presents reflection spectra for the spiral photonic crystals with different pitch sizes. The structures were fabricated using constant illumination parameters, i.e. the spiral cross-sections width and height are equal in all structures. The average laser power is set to 4mW, the illumination time is set to 1ms. Also in this case each spiral has a radius $r=0.65\ \mu\text{m}$ and distance between the neighbouring spirals of $d=1.2\ \mu\text{m}$. Each structure consists of 18 x 18 single spirals completing 5 revolutions in the vertical direction. Again supporting structures are provided in order to avoid possible deformations due to shrinkage and to make sure that no part of the photonic crystal is truncated by the carrier substrate.

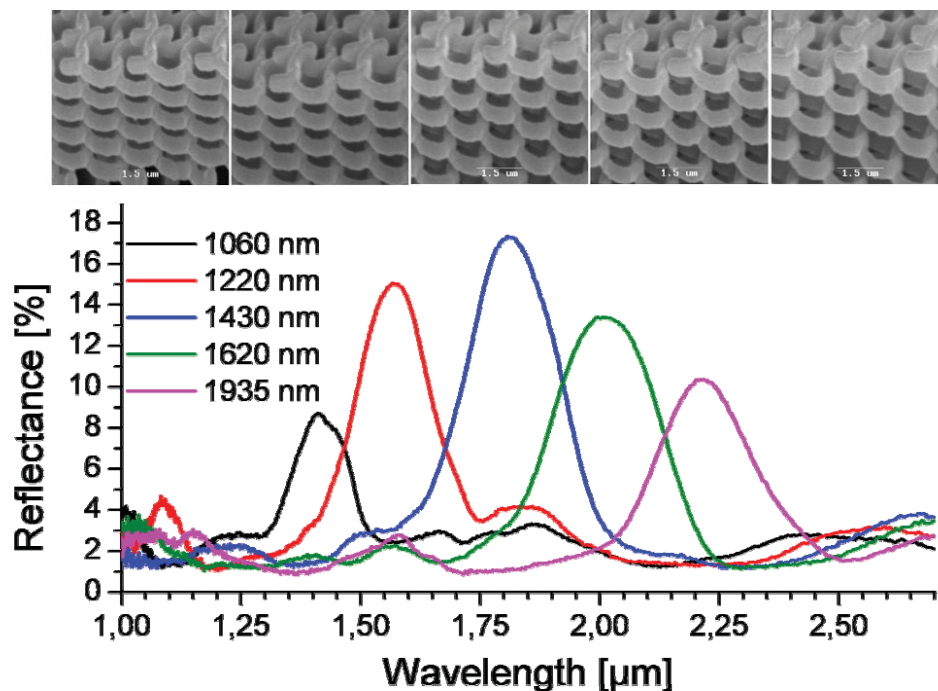


Figure 3.24 Measured reflection spectra for spiral photonic crystal with different pitch sizes; Inset at the top shows according SEM images of the structures, from left to right: 1060nm, 1220nm, 1430nm, 1620nm, 1935nm.

For pitch values between 1060nm and 1935nm, the central position of the measured reflection peaks is shifted by about 850nm. By increasing the value of the pitch size, while the rest of the parameters are fixed, one is simultaneously reducing the relative value of the dielectric filling fraction Φ . For pitch size values of 1060nm, 1220nm, 1430nm, 1620nm, and 1935nm, the calculated values of Φ are accordingly 23%, 20%, 16.5%, 13% and 11%. Comparison of the results presented in figures 3.24 and 3.23, shows that the directions of the shifts resulting from increasing the pitch size and decreasing the Φ only are opposite. Therefore, in comparison to a variation of the value of Φ only, larger relative shift of the central bandstop position can be obtained by tuning the spirals pitch.

The maximum reflection signal is obtained for the spirals with pitch size value of 1430 nm. This photonic crystal has a filling fraction of 16.5%, which is close to the optimum value of 16% obtained from experiment on Φ optimisation. From here it is concluded that the quality of the bandgap is mainly influenced by the parameter Φ , while the central position of the bandstop is best defined by the pitch size.

Fabrication of 3D photonic crystals containing an active nonlinear optical chromophore

Photonic crystals are considered to be the optical equivalent of semiconductors, as they modify the properties of light in the same way a semiconductor does for electrons. However, in contrast with electrons, photons cannot be easily dynamically tuned; for this, it is necessary fabricate photonic crystals made of nonlinear materials, whose optical response depends on the intensity of light that propagates through them. The unique properties of nonlinear photonic crystals would allow the creation of fast and compact all-optical devices. Despite efforts over the last decade, investigations into nonlinear photonic crystals have been limited to theoretical simulations and the fabrication of one or two dimensional semiconductor systems.

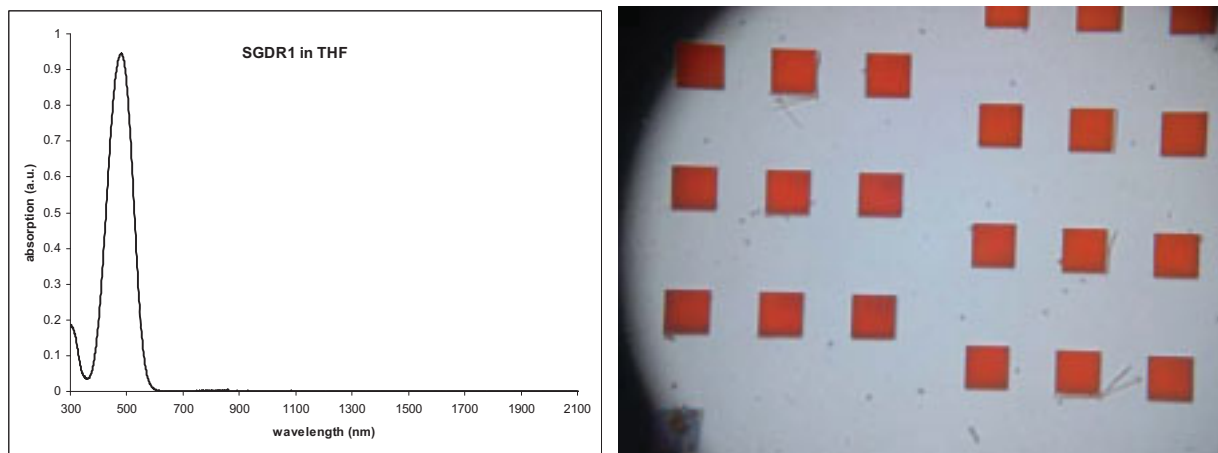
Nonlinear optical (NLO) silica sol-gel materials have attracted much interest because of advantages such as high nonlinearity, low cost, high poling efficiency and stable alignment of chromophore molecules, leading to high temporal and thermal stability of their nonlinear performance [ZLP⁺04, GCL⁺01]. Incorporating NLO chromophores into sol-gels in either a guest–host or a side-chain–main-chain strategy has produced electro-optically active sol-gels [EDM⁺07]. Research to date in this direction has only produced planar electro-optic devices [ZLL⁺04, ZLF06].

Side-chain-main chain incorporation strategy presents a more appropriate way when it comes to 2PP microfabrication, since NLO dopants might be washed out the guest-host structure in the development step involving solvents. In this work ORMOSIL photosensitive sol-gel is modified to contain NLO chromophore DR1. 2PP technique is employed to fabricate 3D photonic crystals with bandgaps in the near-IR spectral region. Similarly to pure ORMOSIL, this composite material exhibits minimal shrinkage during photopolymerization, eliminating the need for shrinkage compensation or the fabrication of support structures. In order to chemically bind this second-order NLO chromophore to ORMOSIL molecules it is

firstly reacted with (3-isocyanatopropyl) triethoxysilane to form a functionalized silicon alkoxide precursor (SGDR1). The details on material synthesis can be found in section 2.2.

The samples for 2PP processing are prepared by drop-casting the material onto 100 micron thick Indium Tin Oxide (ITO)-coated glass substrates. The resultant gel films are baked at 100 °C for 1 h, to condensate the sol-gel. ITO-coated glass slides were used to enable future electrical poling of the structures. After the 2PP processing, the samples are developed for three minutes in THF and rinsed in 2-propanol.

The absorption spectrum acquired from this composite material film, spincoated on a quartz substrate, is shown in figure 3.25a. The material absorbs very strongly in the spectral region 400-550 nm, but it is completely transparent at 600-2000 nm and has an additional window of transparency in the spectral region 300-400 nm. These properties make SGDR1 ideal for 2PP structuring with a Ti:Sapphire laser, emitting at 780nm. The IR transparency allows the focusing of the laser within the volume of the material, while the relatively high UV transparency means that there will be two-photon absorption mostly by the photoinitiator, and not by the NLO chromophore. In addition, as the material has no natural absorption in the near-IR spectral range, it can be used for the fabrication of photonic crystals exhibiting PBG centred at the telecommunication wavelengths, and consequently any nonlinearity will be off resonance.



a) Figure 3.25 a) absorption spectra of the material containing DR1; b) optical microscope image of an array of fabricated woodpile photonic crystals (single structure size is 30µm).

The structures were fabricated layer-by-layer bottom up with the last layer attached to the coverslip. After the completion of the component build process, the sample was developed for three minutes in THF and rinsed in 2-propanol. Figure 3.25b shows an optical microscope image of an array of photonic crystals; they have the bright red colour of Disperse Red 1. Scanning Electron Microscope (SEM) images of a DR1-containing photonic crystal fabricated by the 2PP are presented in the figure 3.26. As it can be seen, SGDR1 can be structured very accurately and without defects. Due to the properties of the ORMOSIL matrix the fabricated structures are not affected by shrinkage and no additional restraining support structures or precompensation procedure is required. The highest resolution achieved in this material is 250

nm. FTIR transmission spectra of fabricated structures confirmed the existence of a bandstop around $1.5\mu\text{m}$ (not shown).

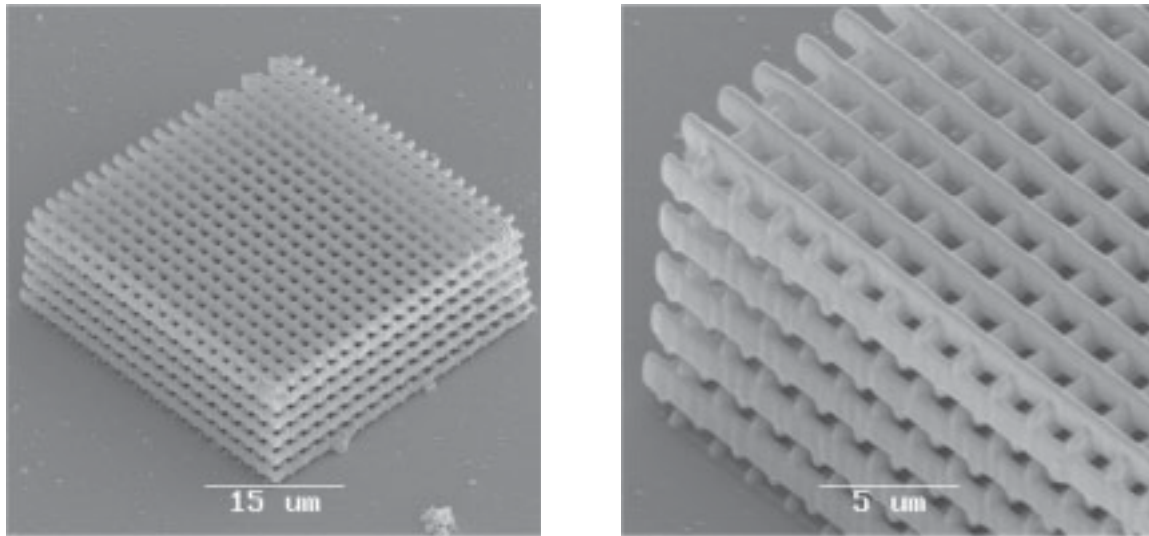


Figure 3.26 SEM images of woodpile photonic crystal fabricated by 2PP of NLO material.

Previous studies have shown that Disperse Red 1 sol-gel copolymers exhibit second order nonlinearity, with $d_{33}=30\text{-}55\text{ pm/V}$ at 1300 nm , depending on the DR1 content [CPR⁺98, RCL⁺95]. To manifest this nonlinearity, the symmetry in the material needs to be removed. This can be done by corona poling the samples at elevated temperatures. Once corona poled, the samples have been reported to exhibit excellent optical as well as mechanical stability.

Fabrication of Shaped 3D Photonic Crystals

Very often photonic crystals shape and surface termination can play an important role [SG05, MDM⁺07]. For this purpose a software application based on constructive solid geometry approach was developed. Here the inner geometry of the structure is defined as a property of endless space. The shape of the structure is described by a surface in 3D. Application of Boolean intersection between both inputs results in a porous structure with a defined volume.

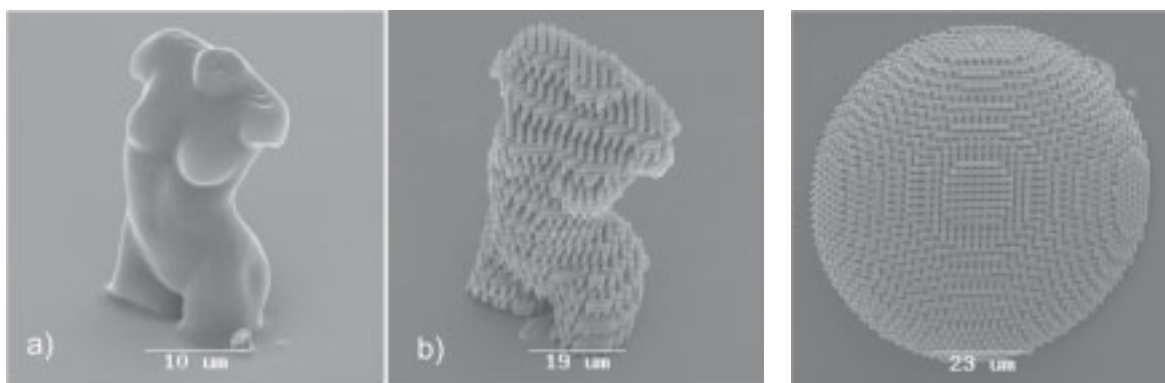


Figure 3.27 SEM images of 2PP produced structures: a) solid microvenus model; b) according “venus-shaped” woodpile; c) lens-shaped woodpile structure.

This method provides independent control over the structures outer shape and inner porosity. Figure 3.27b shows an example of venus-shaped woodpile structure produced by 2PP ofOrmocore material. The outer shape is defined by an introduced 3D surface described in standard stereolithography STL format.

Figure 3.27c shows a top-view SEM image of a lens-shaped woodpile structure. Although initially developed for photonic application, this software provides great opportunities for the fabrication of scaffolds for tissue engineering, as will be described in section 3.3.3.

Conclusions

Fabrication of 3D photonic crystals with various structural parameters, geometries and even shapes has been demonstrated by 2PP microfabrication. It is observed that 2PP allows precise tuning of the PBG position through controlling structural parameters of the fabricated structure in a reproducible manner. On the example of woodpile structures it was shown that quality of the achieved photonic crystals is sufficient to achieve a considerable PBG effect already for 4 unit cells along the testing direction.

Such complex architectures as spiral photonic crystals can be realised by 2PP technique. The woodpile structures were produced by continuous scanning, while “pinpoint” illumination method was applied for spiral structures. SEM analysis showed that high quality structures are achieved for both methods. It is generally considered that for large area microfabrication, pinpoint illumination presents disadvantage of longer processing time, when compared to continuous scanning approach. However, for a realistic micropositioning system, on-the-fly “pinpoint” illumination of spiral structures results in similar or even reduced processing times. Optical characterisation showed that optical response of the same order were obtained for both woodpile and spiral configurations. By setting the structural parameters, measured bandstops for these experimentally realised photonic crystals, can be precisely positioned in the near-IR spectral range at the telecommunication wavelengths.

Dielectric filling fraction (Φ) is very important parameter, influencing the size and, to some extend, the exact position of the PBG. In 2PP microfabrication the Φ value is controlled independently of structural parameters of a photonic crystal, by adjusting the illumination dose. For woodpile architecture a minimal Φ value of 46 % is limited by the stability of the produced structures. Further reduction of Φ value, i.e. woodpiles rods cross-section, results in structures which collapse during the developing step. It was observed that much lower values of Φ can be experimentally realised for spiral photonic crystals. This can be explained by the fact that, compared to woodpile, spiral structure resembles the diamond architecture much closer, while requiring less material [MT04]. In addition, substantial spatial overlap between individual spirals contributes to better mechanical stability and lower Φ values for the spiral architecture.

In order to control the value of Φ in 2PP microfabrication, it is extremely important to have possibility of precise control over the energy of the pulse delivered at the sample. Decrease of

illumination dose and, therefore, resulting voxel size, below a certain threshold, results in an overall structure shrinkage. This process results in deviation of achieved structure parameters from initial specification. On the other hand such “controlled shrinkage” can be used constructively in order to further reduce the structure size (see section 3.1.2).

Higher order features observed in the measured FTIR spectra indicate high optical quality of the fabricated photonic crystal structures. Photonic crystals fabricated from material containing NLO chromophore were demonstrated by 2PP microfabrication. DR1 chromophore was chemically modified and added in a side-chain-main-chain manner to a conventionally used ORMOSIL based sol-gel. It is seen that the NLO chromophore stays inside the material throughout the processing. This method provides important guidelines for alternative material modifications with other nonlinear, electrooptic or photoactive materials. In conclusion, 2PP provides important rapid prototyping tool for realisation of micro- and nanoscale all-optical circuits. For the applications where the existence of complete PBG is essential, structures fabricated by 2PP can be used as templates for further inversion with high refractive index materials [SOC04, TFD⁺06]. Recently demonstrated surface metallization approaches [CTT⁺06, MJT⁺07] provide alternative, often less complex and expensive means for complete PBG realisation.

3.3 Biomedical applications of 2PP microfabrication

3.3.1 Microneedles for Transdermal Drug Delivery

Advances in genetic engineering and proteomics have provided protein- and nucleic acid-based treatments for cancer and other chronic diseases [ZPC04, OS04]. Unfortunately, many novel drugs and vaccines cannot be administered in oral or transdermal form, because they may be metabolized by the kidneys or liver before reaching systemic circulation [PL05]. These agents may be administered intravenously using hypodermic needles; this route provides complete and instantaneous absorption [Pra04]. Use of conventional hypodermic needles involves trauma at the injection site, pain to the patient, medical skill to administer the injection, and difficulty in providing sustained delivery of a pharmacologic agent over extended period of time.

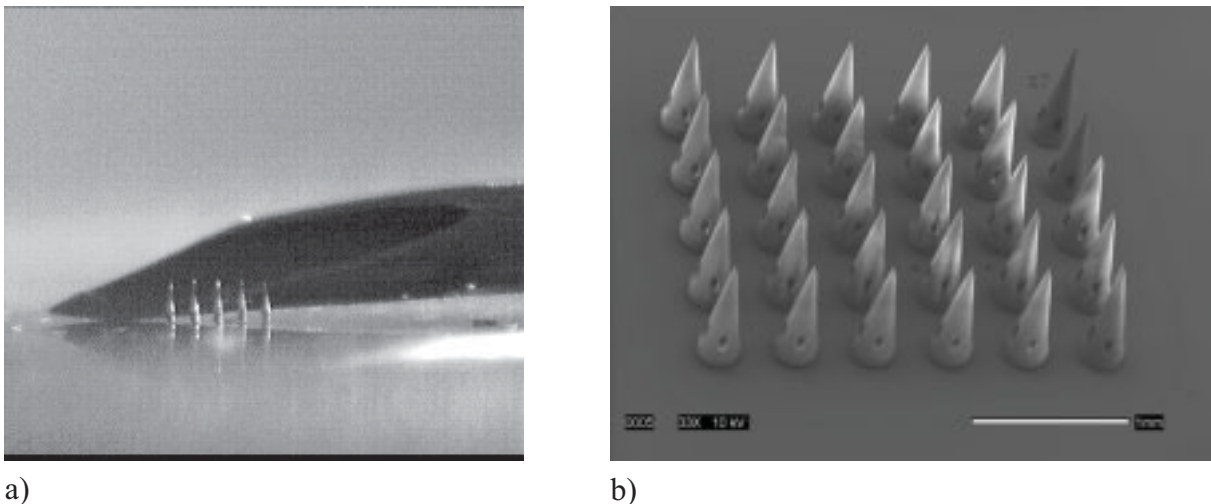
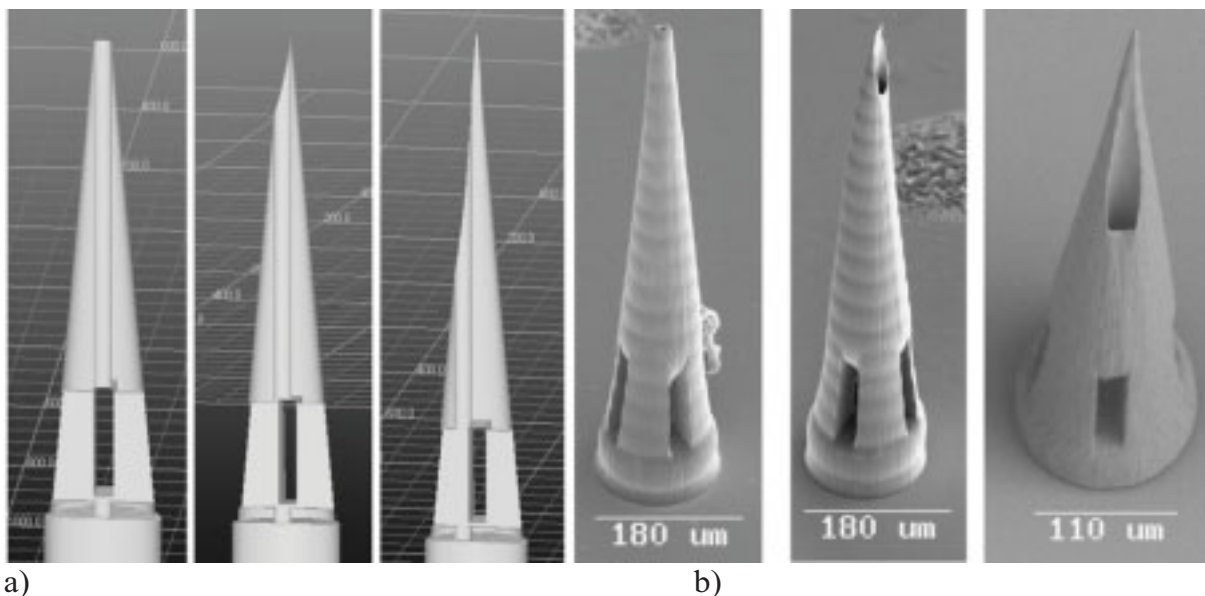


Figure 3.28 Microneedles fabricated by 2PP technique: a) an optical image of five Ormocore microneedles placed next to a conventional hypodermic needle; b) SEM image of an array of microneedles with an offcenter channel.

Transdermal drug delivery is an alternative method that has experienced a rapid development in the past two decades, and has often shown improved efficiency over the other delivery routes [PML04, CF89]. It avoids many issues associated with intravenous drug administration, including pain to the patient, trauma at the injection site, and difficulty in providing sustained release of pharmacologic agents. In addition, precise dosing, safety, and convenience are also addressed by transdermal drug delivery. However, only a small number of pharmacological substances are delivered in this manner today. The most commonly known example is nicotine patches. The main reason for that is the significant barrier to diffusion of substances with higher molecular weight provided by the upper layers of the skin. The top layer, called stratum corneum, is composed of dead cells surrounded by lipid. This layer provides the most significant barrier to diffusion to approximately 90% of transdermal drug applications [Fly96, SSW⁺05]. A few techniques, enhancing the substance delivery through the skin have been proposed. Two of the better-known active technologies are

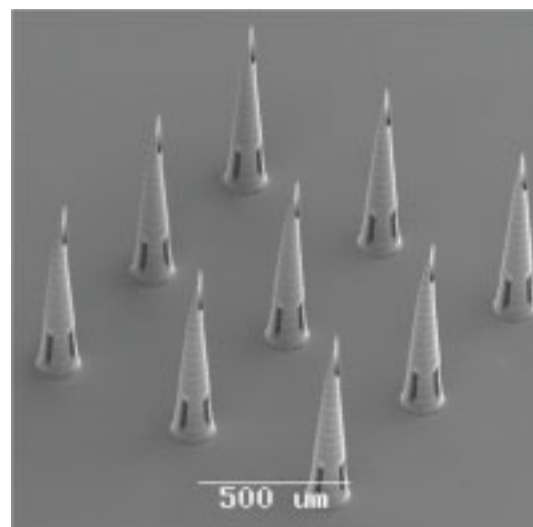
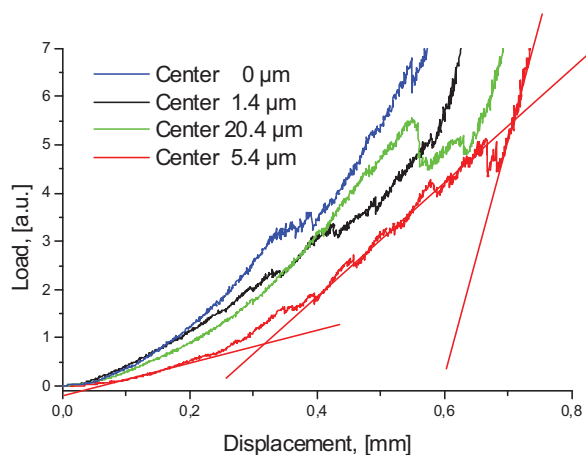
iontophoresis and sonophoresis. The rate of product development, involving these technologies has been relatively slow [Mit01]. This is partly conditioned by the relative complexity of the resulting systems, compared to the passive transdermal systems. One of the passive technologies is based on micro-needle enhanced drug delivery. These systems use arrays of hollow or solid microneedles to open pores in the upper layer of the skin and assist the drug transportation. Figure 3.28 shows examples of such microneedle arrays fabricated by 2PP technique. The length of the needles is chosen such that they do not penetrate into the dermis, pervaded with nerve endings, and thus do not cause pain. In order to penetrate the stratum corneum, microneedles for drug delivery have to be longer than 100 μm , and are generally 300–400 μm long, since the skin exhibits thickness values that vary with age, location, and skin condition. Application of microneedles has been reported to greatly enhance (up to 100,000 fold) the permeation of macromolecules through the skin [Bar01]. Hollow microneedles allow diffusion- or pressure-driven transport of pharmacologic agents through the needle bore to be adjusted over an extended period of time. The microneedles for withdrawal of blood must exceed lengths of 700–900 μm in order to penetrate the dermis, which contains blood vessels. Most importantly, microneedle devices must not fracture during penetration, use, or removal.

Finally, arrays of microneedles may be used to provide pharmacologic agent injection or biological fluid extraction at higher rates and over a wider area than individual microneedles. Microneedle arrays provide redundancy if individual needles are fractured or obstructed during the microneedle insertion process [GLB03]. In addition, arrays of microneedles provide greater possibilities for directly reaching vasculature in the dermis for extraction of blood. Microneedle arrays are also less prone to fracture if exposed to shear forces, because these forces are distributed over a wider area [GS03].



a) b)
Figure 3.29 Hollow microneedles for transdermal drug delivery: a) cross-section of original CAD design of microneedles with various positions of the channel center. The channel displacement allows to control the tip sharpness; b) SEM images of according microneedles fabricated by 2PP technique.

The flexibility and high resolution of the 2PP technique allows rapid fabrication of microneedle arrays with various geometries, and study its effect on the tissue penetration properties. In order to study the effect of microneedles geometry on its penetration properties, square arrays of 25 identical 500 μm spaced needles were fabricated by 2PP ofOrmocore material. Since these structures do not require very high resolution in the vertical direction, a conventional 10X microscope objective (0.2 NA) lens was used to focus the laser beam into a volume containing photosensitive resin. The average length of a fabricated needle is 800 μm and the base diameters are in a range 150-300 μm . The length of the needle enables its application for both drug delivery and blood drawing. Tip sharpness was changed by adjusting the position of the channel relative to the central symmetry axis in the original design (see figure 3.28). The diameter of the channel is fixed for all the samples. The four openings visible at the base of each needle were fabricated in order to guarantee the complete removal of the non-crosslinked polymer from the channel during the developing fabrication step, since one end of the needle would be blocked by the glass coverslip otherwise. These openings are omitted in the needles actually used for flow studies and drug delivery, since in that case both channel ends are open.



a)

b)

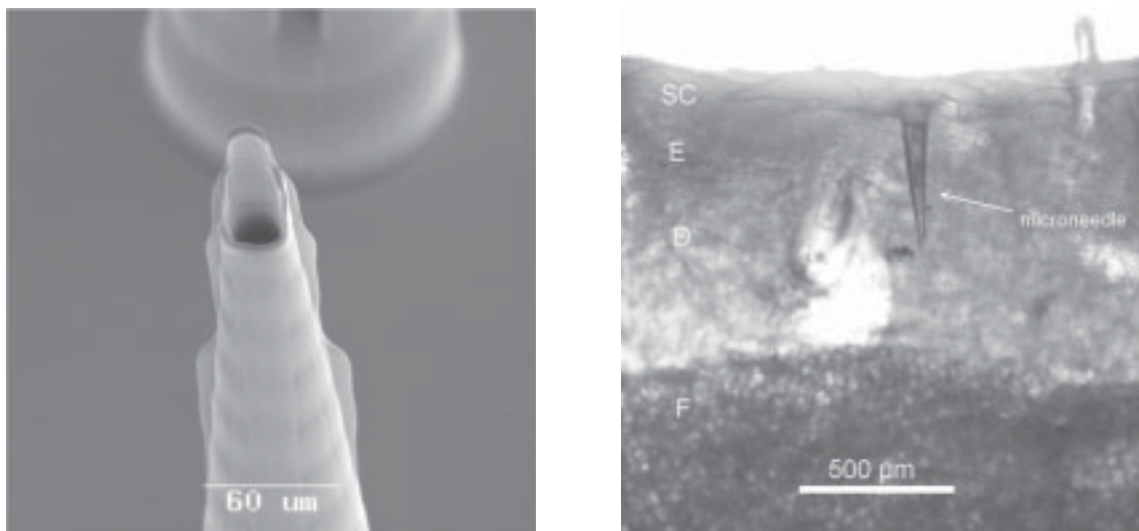
Figure 3.30 a) Load-displacement curves obtained for the needles with different flow channel-microneedle tip displacement (indicated in μm for each design); b) SEM image of a 3x3 off-centre microneedles array in the optimum configuration (channel is displaced by 5.4 μm relative to the needle axis).

Naturally it is desirable to fabricate needles that require least load in order to penetrate the skin. Microneedles undergo several forces during insertion into the skin, including compressive forces, bending forces, shear forces, buckling forces, and skin resistance. Fracture testing and penetration testing of microneedle arrays was determined using compression load testing (ELF 3200, Bose EnduraTEC Systems Group, Minnetonka, MN, USA). In these studies, 50 g and 500 g load cells were driven at 0.008 mm/s displacement rate against polytetrafluoroethylene (duPont, Wilmington, DE, USA) and cadaveric porcine adipose tissue (Nahunta Pork, Pikeville, NC, USA). Cadaveric porcine material was chosen

for this study because porcine epidermal and dermal layers closely resemble their human counterparts. Although cadaveric porcine adipose tissue is softer than whole porcine skin, it exhibits a homogeneous, uniform surface that is appropriate for mechanical testing. A video capture device was used to examine the microneedle penetration behaviour and determine the mode of failure.

Figure 3.30a contains load-displacement curves for in-plane and out-of-plane hollow microneedle arrays with several flow channel-microneedle tip displacement values (indicated in μm on the graph). Similar load vs. displacement curves were observed for needles with different base diameters. As indicated by the asymptotes, the slopes on the curves can be divided into three regions (from left to right), exhibiting different trends: initial needle contact with the porcine adipose tissue, prior its surface puncture; tissue puncture by a single, few or complete microneedles array; the final displacement value attributed to the contact between the tissue and the cover slip substrates carrying the microneedle array. The local maximum values indicate the points at which the load threshold was reached. At these values, the porcine adipose tissue was punctured by one or few microneedles in the microneedle array. Local minimum values were observed immediately adjacent to these local maximum values. The “off-center microneedles” with channel positioned at $20.4\mu\text{m}$ relative to the needles axis exhibited the sharpest needle tips values among the out-of-plane microneedles (see rightmost images in figure 3.29 ab). However, series of experiments consistently confirmed the lowest penetration threshold for the microneedles array with channel to tip displacement value of $5.4\mu\text{m}$, and not $20.4\mu\text{m}$ which has the sharpest tip. Optical microscopy analysis of the microneedles tips helped to clarify the situation. Apparently very long and sharp but less rigid tips of the microneedles with the channel shifted by $20.4\mu\text{m}$ relative to the needles axis, are bent during tissue penetration. Needle tip bending is associated with the presence of methacrylate groups in the cross-linked Ormocore, as a consequence the structures stay somewhat elastic. During the test the tip bends even further, resulting in increased penetration resistance and therefore the larger values of load threshold. Overall results indicate minimal dependence between geometry and skin penetration properties for polymeric microneedles fabricated using two photon polymerization.

Similar load vs displacement curves acquired for microneedles with different aspect ratios indicated a minor difference in the load values for different needles. The tests against polytetrafluoroethylene surfaces however suggested dependence in failure. In general, the larger the base of the microneedle, the higher the load it can endure before breaking or bending. Majority of the microneedles bend, and eventually tip off the glass when tested against polytetrafluoroethylene. Therefore by improving the needle attachment to the substrate one can further increase failure load threshold. This can be done by applying adhesion promoter to the substrate or by producing substrate from the same material as the microneedles.



a)

b)

Figure 3.31 a) SEM image of bioinspired microneedle with mosquito-like tip; b) optical micrograph of 2PP fabricated microneedle on full thickness porcine skin. Abbreviations on the left side of the image indicate different skin layers: the stratum corneum (SC), epidermis (E), dermis (D), and fat (F).

The 2PP microfabrication allows to introduce precise structural details into the needle design. Figure 3.31 shows a microneedle whose design was inspired by female mosquito fascicle. Mosquito needle is a well known “nature-created” tool for effective and painless “blood sampling”. Mosquito fascicle has a somewhat flat tip and additional microstructures on its sides [LO71]. It has been suggested that by applying small amplitude vibrations the mosquito cuts through the skin, rather than just statically puncturing it, this way reducing the force needed for penetration [YZ04]. Fracture and penetration study of 2PP fabricated microneedles with such saw-toothed walls showed no significant differences in load response. A separate trial was performed with such biomimetic microneedle arrays mounted on 3D piezoelectric actuator (in x, y, and z) in order to mimic mosquito fascicle movement. In this case vibrations, induced by piezo actuator, resulted in high noise levels in load response, which did not allow to draw any evidential conclusions, when compared to no piezoelectric actuation. Therefore a more sensitive apparatus has to be used in order to verify the advantages of such tip geometry over the other proposed designs.

Figure 3.31b shows an optical microscope image of a single microneedle on full thickness porcine skin. It is observed that the inserted 2PP fabricated needle penetrates all the way through epidermis, and will allow substance injection directly into dermis. Controlled administration of fluorescein-conjugated biotin (a water-soluble B-complex vitamin) solution into the dermal and hypodermal regions of skin was studied using off-centered microneedles. Figure 3.32 shows DIC-fluorescence micrographs of skin sections injected with biotin and frozen at various times. The images containing the skin cross-sections with the microneedle-induced perforations show injected substance penetration through diffusion at different times after injection. After 5 minutes, the biotin is localized in the perforation created by the microneedles. After 20 minutes, the diffusion of biotin into the dermal/epidermal junction is evident. At 60 minutes, the entire dosage of biotin diffused as deep as the dermal/hypodermal

region of the skin. At the same time the control sample (biotin applied on the surface of the skin) showed no diffusion beyond the stratum corneum even after 60 min.

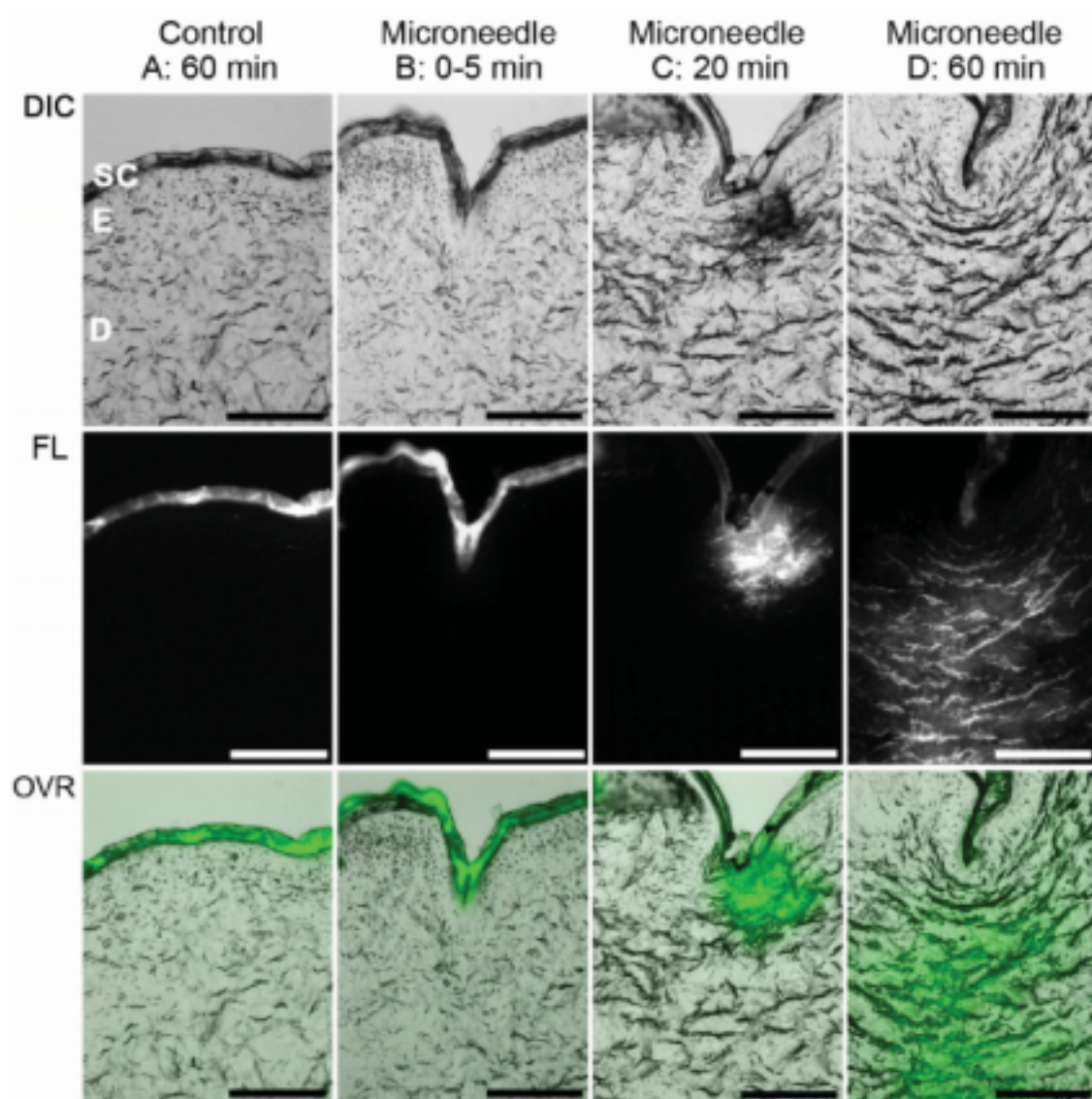


Figure 3.32 DIC-fluorescence microscopy of skin after administration of fluorescein-conjugated biotin using microneedles fabricated by 2PP technique. Treatment duration with microneedle (5 min, 20 min, and 60 min) is indicated on top of each column and may be compared with control at 60 min (without microneedle). Top row: DIC single-channel provides clear view of the various skin layers. The stratum corneum (SC), epidermis (E), and dermis (D) layers are indicated. Middle row: fluorescence images (FL) of fluorescein-biotin emission. Bottom row: DIC-fluorescence overlay (OVR) with the fluorescence channel (Green) shows distribution of biotin within the skin layers. Scale bar equals 100 μm in all images.

Conclusions

Microneedle arrays developed using conventional microelectronics fabrication techniques have inherent limitations that preclude the development of complex geometries and microneedles with large wall thicknesses. CAD/CAM rapid prototyping allows fabrication of complex geometries and rapid iterations of the structure design. Novel microneedles

developed in this fashion can readily be integrated with MEMS devices to allow control over amount and rate of pharmacologic administration. The control over the geometry of the microneedle enables its application for both drug delivery and blood sampling. Results of our studies indicate that microneedles created using the 2PP technique are suitable for *in vivo* use, and for the integration with the next generation MEMS- and NEMS-based drug delivery devices.

3.3.2 Fabrication of Microprosthesis

The malleus, incus, and stapes bones compose a so-called ossicular chain that serves to transmit sounds from the tympanic membrane to the inner ear (see figure 3.33ab). Ear diseases may cause discontinuity or fixation of the ossicles, which results in conductive hearing loss [Dan98, Cru94]. Ossiculoplasty is a technique for reconstruction of the bones of ossicular chain within the middle ear [Alb98, Bay00, Goo94]. The traditional method for restoring sound conduction in the middle ear involves the use of the remaining ossicles [Col99]. The most commonly used material is the patient's own incus bone. However, autograft materials are not always available in patients suffering from chronic diseases. In addition, shaping of these materials requires additional operative time. There are also concerns regarding loss of rigidity, resorption, or fixation of the implant to the wall of the middle ear. Homograft materials, which are obtained from cadavers, are now rarely used due to the risk of infection [Cur00, Gla88]. Alternatively artificial prostheses are used in ossiculoplasty. Figure 3.33c shows schematics of such reconstruction where a part of remaining stapes bone is used along with the partial ossicular replacement prosthesis. Several alloplastic materials have been considered for use in ossicular reconstruction. Polyethylene, high-density polyethylene sponge, polytetrafluoroethylene (PTFE), and Proplast (PTFE-carbon composite) pistons were used in middle ear reconstruction [Bra86]. These materials demonstrated migration, extrusion, penetration into the inner ear, and significant middle ear reactivity, resulting in a necessity of a repeated surgery. As a result, these solid polymers are not currently used for restoration of sound conduction. Titanium, alumina, stainless steel, and gold are biocompatible materials that have been considered for use in ossicular reconstruction [Jah83, Sch98, Str99, Sch06, Wan99, Zah00]. For example, titanium prostheses have demonstrated biocompatibility, rigidity, biostability, low ferromagneticity, low density, and good sound conduction. However, recent studies have indicated that a thin cartilage graft is needed to cover the head plate of the prosthesis and prevent prosthesis extrusion. Bioactive materials (Bioglass, Ceravital, hydroxyapatite) promote direct chemical bonding with body tissues, and bioactive prostheses were developed with the hope that these materials would have a lower rate of extrusion [Gro86, Gro85, Bli86, Man90, Gol00]. These materials can be placed directly under the tympanic membrane, and do not demonstrate significant extrusion. However, bioactive materials have not gained wide acceptance due to difficulty in shaping the prostheses and mechanical instability, especially at infected middle ear sites.

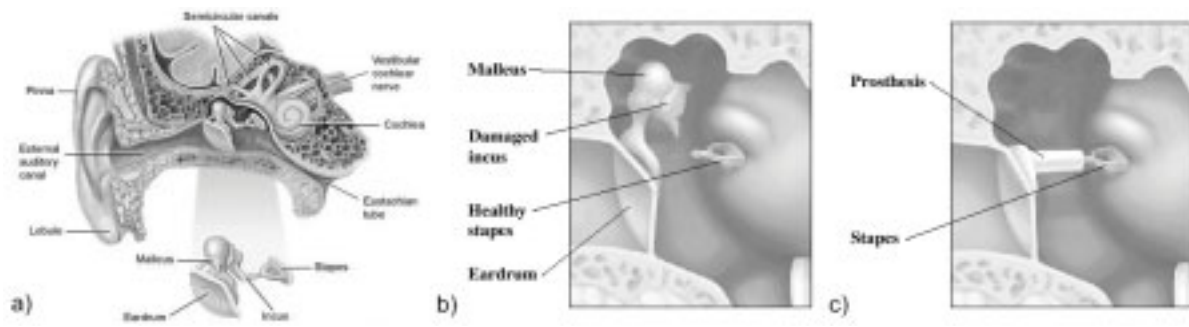


Figure 3.33 Schematic representation of: a) middle ear and ossicular chain; b) ossicular chain with damaged incus; c) ossicular chain repaired with Partial Ossicular Replacement Prosthesis (PORP) [www.SJ]

Novel materials and prostheses that provide improved sound transmission for longer periods of time are demanded by patients and surgeons. These materials must demonstrate a high degree of cell compatibility, ease of use, and minimal extrusion [Mer99, Mor98, Mur05]. Mass-produced implants are produced in several shapes and sizes; however, these designs do not take individual patient anatomy into account. One way of increasing the success of ossicular prostheses is the development of patient-specific implants [Mah95, Lim02]. Such implants possess the appropriate design features, including head size, weight, and footplate attachment, for a particular patient.

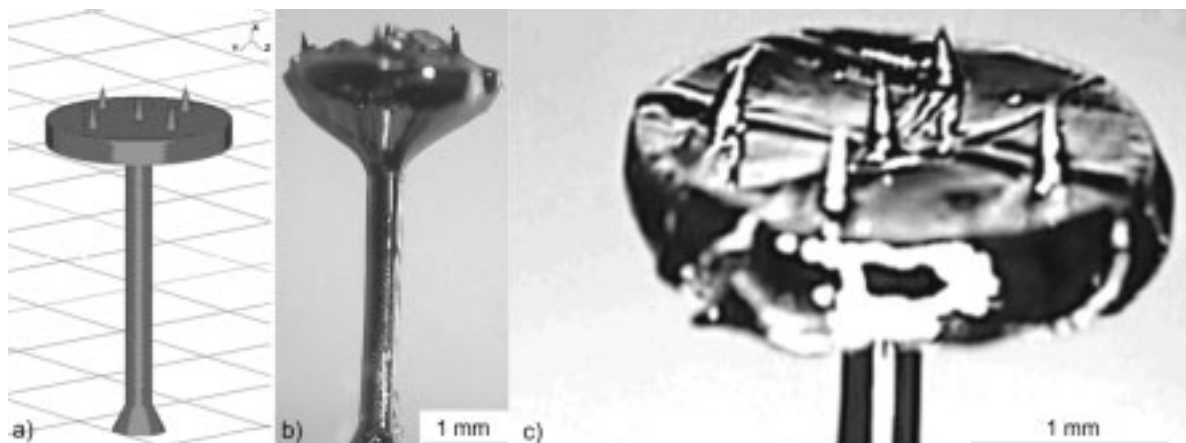
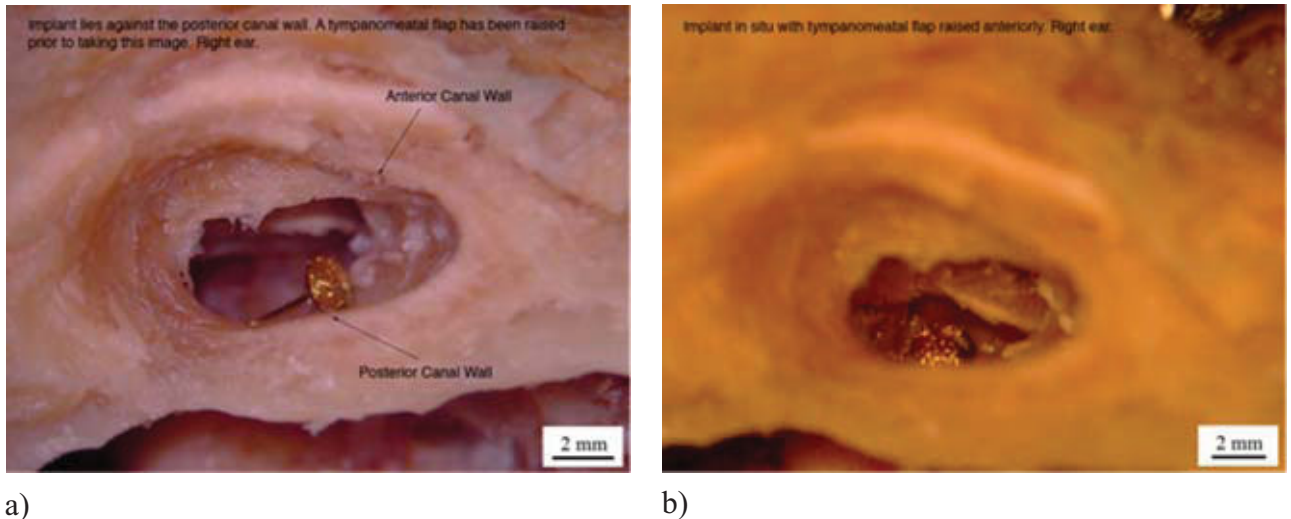


Figure 3.34 Total Ossicular Replacement Prosthesis (TORP): a) original design; b) optical image of a structure fabricated by 2PP ofOrmocore; c) close-up on the fabricated TORPs head plate.

Ormocore surfaces fabricated using 2PP approach demonstrated acceptable cell viability and cell growth profiles [DPN05]. Here we demonstrate the use of 2PP technique for rapid prototyping of Ormocore middle-ear bone replacement prostheses. The design used in this study was similar to that of a commercially available TORP prosthesis (total ossicular replacement prosthesis, Kurz Medical Inc., Dusslingen, Germany). Figure 3.34a contains a CAD and optical image of the TORP-shaped Ormocore ossicular prostheses. Such structure was produced by 2PP (see Figure 3.34bc) directly from CAD input in a layer-by-layer approach, with a distance of 25 μ m between the layers. The prostheses stand 4.3 mm tall, 300-400 μ m wide at shaft, 2.6 mm wide and 400-500 μ m thick at the diskshaped headplate. The

disk-shaped headplate of the prosthesis was designed to be placed under the tympanic membrane. The shaft of the prosthesis is designed to connect the footplate of the stapes with the undersurface of the tympanic membrane in order to enable sound conduction. The headplate also contained five microneedle-like structures protruding at 400 μm with 160 μm base width. These structures are introduced to improve cellular adhesion, avoid device migration, or provide means for possible cartilage attachment before the operation.



a) b)
 Figure 3.35 The implantation process of the 2PP fabricated TORP through the right external auditory canal: a) prosthesis aligned against the posterior canal wall; b) the implant positioned *in situ* on the footplate of the stapes below the tympanic membrane to provide sound conduction, as found in natural middle ear.

An important criterion for such prosthesis is the handling in a real operational room environment. In order to verify it, *in vitro* implantation test was performed into the right ear of commercially obtained human head. First the chorda tympani was partly removed in order to provide access to the middle ear and a possibility of optical imaging. The natural incus and the head of the stapes, initially present in the middle ear, were removed using surgical tools. The 2PP fabricated Ormocore prosthesis was then carefully aligned against the posterior canal wall (see figure 3.35 a). Finally, the implant was positioned *in situ* on the footplate of the stapes below the tympanic membrane to provide sound conduction, as found in natural middle ear (see figure 3.35 b). The prosthesis was handled without fracture during the entire procedure. The detailed description of this *in vitro* implantation study can be found elsewhere [OCA07].

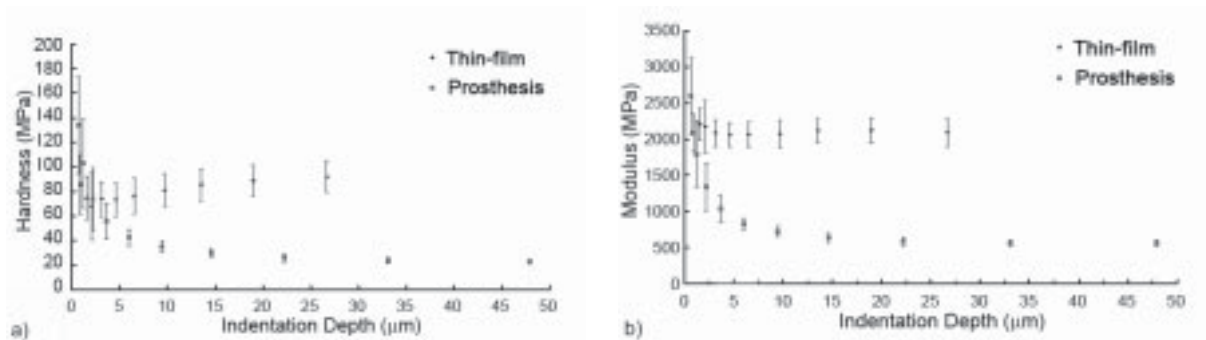


Figure 3.36 Nanoindentation test results of UV photopolymerized Ormocore thin film and Ormocore ear-prosthesis fabricated by 2PP technique: a) hardness (MPa) vs indentation depth; b) modulus (MPa) vs indentation depth. Error bars indicate standard deviation of mean.

For the mechanical tests the headplate was separated from the fabricated TORP. Nanoindentation tests performed on the surface of the headplate of the ossicular prosthesis were compared with thin-film Ormocore material (Figure 3.36). As the load increased, the measured values of Hardness (H) and Modulus (E) of the Ormocore thin-film were found to be significantly higher than the headplate surface. Both values were consistently higher by a factor of four in the thin-film material.

Conclusions

To conclude, ossicular replacement prosthesis fabricated by 2PP has shown good mechanical properties and ease of handling. The applied Ormocore material can be photostructured with high precision using 2PP technique, and has shown good biocompatibility. As mentioned earlier, conventional mass-produced implants do not sufficiently take individual patient anatomy into account. CAD/CAM rapid prototyping by 2PP may permit development of patient-specific geometries to allow unique fit with surrounding middle ear configurations and minimize prosthesis rotation and migration. Imaging (computerized tomography or magnetic resonance imaging) and image analysis software may be employed to generate implants with appropriate design, structure, and material properties for a particular patient. In addition, these prostheses may be designed to possess pores, which allow for diffusion of nutrients to cells and waste matter away from cells. Pore connectivity, shape, and size may influence cell-prosthesis interaction.

3.3.3 Scaffolds for Tissue Engineering (Recreating cellular microenvironment by 2PP).

Tissue engineering is an interdisciplinary field that applies the principles of engineering and life sciences toward the development of biological substitutes that restore, maintain, or improve tissue function or a whole organ. Tissue engineering has also been defined as "understanding the principles of tissue growth, and applying this to produce functional replacement tissue for clinical use" [www.Wk]. Cells in the body are exposed to a complex milieu regulated by their interactions with other cells, the surrounding cell matrix and soluble factors. A key element of this microenvironment is the 3D architecture of the extracellular matrix (ECM). Furthermore, upon removing cells from this microenvironment many cell types, such as liver cells, quickly lose their function. One of the most popular approaches for tissue engineering relies on the application of scaffolds. Scaffolds help to guide cell growth and create certain milieu required for cells to form a functional 3D tissue. Generally, scaffolds have to fulfil several basic requirements. They should promote cell attachment and migration, enable diffusion of vital cell nutrients and expressed products, and have appropriate mechanical properties [Hut01]. A number of studies have demonstrated that cells in artificial 3D matrices have an improved function relative to their culture on 2D substrates. Ideally the 3D matrices should mimic the structure and biological function of native ECM as much as possible. In an artificial scaffold pore shape, size, their distribution and connectivity play an important role. These factors influence the regeneration process [HKM⁺08], and simultaneously define the mechanical properties of the structure [Liu96].

Most conventional scaffold fabrication approaches such as freeze-drying, phase separation, solvent casting etc. have limitations when it comes to precise control of the scaffold internal architecture. Using these techniques it is now feasible to control pore connectivity and pore size. Porosity levels of around 90% can be realised, this way providing sufficient pore connectivity for cell attachment and nutrition factors diffusion. However no active control over the size and the position of each individual pore is provided. As a consequence, it is virtually impossible to produce structures in accordance to a predefined blueprint or series identical scaffolds.

With emergency of solid freeform fabrication and rapid prototyping technologies it became possible to partly solve these problems. Such techniques as stereolithography, 3D printing, selective laser sintering or fused deposition modelling allow realisation of structures using a predefined CAD model. Many materials, relevant in biomedical and specifically tissue engineering fields have been successfully tested. Some of these techniques even allow deposition of living cells and proteins directly during the fabrication process. Of equal importance is the fact that also the external shape of such scaffold can be defined in the initial CAD design. Using the 3D data input, provided for example by computer tomography, patient-specific scaffolds conforming to individual anatomic structure at the implantation sight can be realised.

A main difference between described passive and active technological approaches is the size scale. Passive technologies can produce scaffolds with pore sizes in the range from a

few microns to hundreds of micrometers. In solid freeform fabrication and rapid prototyping, due to limited structural resolution, large scaffolds with pore sizes on the order of hundreds of microns are produced. In order to overcome this barrier a combination of both, three-dimensional printing and salt-leaching has been applied [RSR⁺03]. This way the large features inside the scaffold are defined in accordance to initial CAD design, while smaller pore size and distribution cannot be controlled precisely.

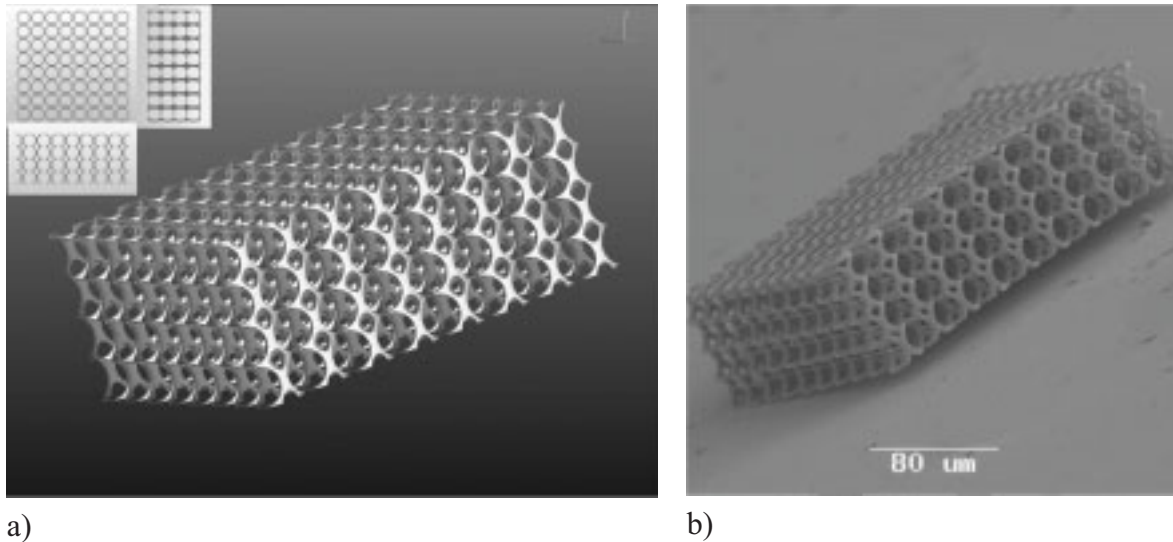


Figure 3.37 Highly porous 3D scaffold with two distinct pore dimensions: a) CAD concept (inset shows three side projections of the structure); b) SEM image of according structure fabricated by 2PP technique.

On the other hand, the structural resolution of the 2PP microfabrication technique can be scaled up by using a different focussing optics. Therefore, 2PP technique allows to close the existing gap in structural parameters of scaffolds produced by different techniques. Structures with feature sizes ranging from submicrometer to hundreds of microns can be now produced using a single technique. The particular advantage of 2PP technique for the fabrication of scaffolds for tissue engineering is the possibility to precisely control both external shape and internal porosity of the structure while delivering high structural resolution. Figure 3.27 in section 3.3.2 presented a shaped photonic crystal structure produced by 2PP, it can be seen as an example of such porous structure. Scaffolds with a more sophisticated pore size distribution can be realised by designing the pores directly. For the first time it is possible to create a “designer scaffolds” with feature sizes on the order of that of the natural extracellular matrix. The position of pores with sizes ranging from hundreds of microns down so submicrometer can now be exactly defined inside the scaffold. Figure 3.37a shows a CAD design of such scaffold having porosity of more than 80%, an inset in the image presents three side projections of the structure. The through pores, which can be accessed from each scaffold surface, are large enough to accommodate cells. A second set of pores, having diameter much smaller than the cell dimension, is introduced in order to enhance fluid transport inside the scaffold. In addition, the mechanical properties of such scaffold can be controlled by adjusting the applied material properties, varying the porosity and introducing changes in the internal geometry of the structure. An SEM image of according scaffold

fabricated by 2PP of Zr-based hybrid Ormosil material is shown in figure 3.37b. Despite high porosity the structure is mechanically stable. Large pores have diameter of around $20\mu\text{m}$. Interconnected micropores, of around $5\mu\text{m}$, while not accessible by cells, provide means for liquid transport inside this 3D scaffold. The high reproducibility of 2PP microfabrication, for the first time allows the fabrication of large series of identical samples, and therefore, enables systematic studies of scaffold-cell and cell-cell interactions in a 3D system.

One of the issues associated with the repair of large volume tissue defects is vascularisation. Since 2PP allows introducing pores of desired size at any location in the scaffold, it has a great potential for defining the future vascular network already in the initial scaffold fabrication step. This way it would be possible to integrate the newly formed vascular network, with the one already present around the particular defect in the body. Figure 3.38 shows an original CAD design of a fragment of a branching microcapillarie network model and an according structure fabricated by 2PP of SU8 material. The overall structure diameter is about $100\mu\text{m}$, the smallest feature size is around $2\mu\text{m}$. Similarly to most mammalian branching vascular and respiratory networks, the Murray's law governing the relation between the branching vessel diameters has been taken into account here.

The properties of material applied for scaffold fabrication can play a crucial role in tissue formation mechanisms. For adherent cells, the proliferation is only possible if the cells attach to the cultivation surface. Different properties of the culture material affect the adherence of the cells to the surface. It is known that a favourable distribution of charges influences the interaction between cellular adhesion molecules, such as integrins, and material [SVK95].

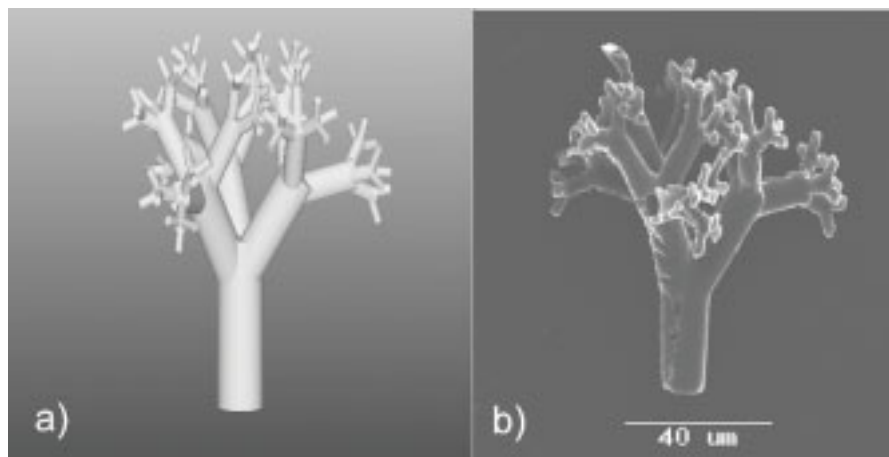


Figure 3.38 An original CAD design (a) and a scanning electron microscope (SEM) image of a fabricated structure (b), which resembles a fragment of pulmonary alveoli – microcapillaries responsible for gas exchange in the mammalian lungs.

In order to test the biocompatibility of materials applied for 2PP microfabrication, various cells were seeded onto flat cover slips coated with these materials. By comparing the proliferation rates of cells grown on flat material surfaces and under control conditions, it was demonstrated that hybrid organic inorganic and SU8 materials are not cytotoxic. Thus, these

polymers do not affect the cell proliferation in a negative manner, which demonstrates that they fulfil the minimum requirement for a scaffold material. However, there still can be effects associated with the modifications on a genetic level. If the adherent cells, used in this study, can not attach, they react by reduction of the proliferation rate and even by inducing cell death, which correlates with an increase of the DNA damage effect. Additional tests comparing the DNA strand breaking of the cells grown on the Ormocore and in control conditions have shown no statistically significant influence by the presence of Ormocore. The presence of Ormocore does not alter the proliferation parameter of the cells and does not increase the tailmoment. Therefore, one can conclude that Ormocore sustains the adhesion of cells.

When the intercellular junctions of a new tissue are formed, the gap junctions are the last junctions which are established. Their formation is conditioned by cell-to-cell adhesion structures, composed from other molecules, such as cadherins and cadherin-associated molecules [FNT⁺97]. Gap junction are cell-to-cell adhesion structures composed of direct cell-to-cell channels which allow a direct exchange of ions and small metabolites such as second messengers between neighbouring cells. An evidence of gap junction formation is therefore a good merit for evaluation of tissue formation. The compatibility of Ormocore with the formation of cellular junctions appropriate for the living tissue, such as gap junction coupling, was studied the double whole patch-clamp technique [NAT⁺05]. The gap-junction conductance measurements reveal that Ormocore does not alter formation of cell-to-cell junctions, critical for functional tissue growth [OSN⁺07]. Based on these results one can conclude that the cultivation of cells on Ormocore is compatible with the formation of tissue. The full description of the results of this study can be found in a following publication [SNO⁺07].

Conclusions

The fabrication of scaffolds with a desired structure in 3D is a very important task in tissue engineering. It has been demonstrated that CAD designed complex 3D structures can be generated by 2PP technique. Using different cell lines, it has been shown that two important polymers used for 2PP: Ormocore and SU8, support cell growth and are biocompatible at the cellular level. Cells are able to form cell-to-cell junctions, such as gap junctions, characteristic to functional tissue. It has been demonstrated that cells can be grown of the vertical surfaces of Ormocore structures generated by 2PP technique. These results demonstrate the great potential of 2PP technology for the fabrication of 3D scaffolds and test structures for tissue engineering and systematic cell interaction studies in 3D. Structures with feature size similar to natural extracellular matrix can be produced. With respect to other techniques conventionally used for scaffold fabrication, 2PP technique allows to close the existing gap in structural parameters of resulting structures. The high reproducibility of 2PP microfabrication, for the first time allows the fabrication of large series of identical samples, and therefore, enables systematic studies of scaffold-cell and cell-cell interactions in a 3D system.

4 Summary and Outlook

This thesis presented results of work on the development of 2PP technique and exploration of some its specific applications in optics and biomedicine. The results of the fundamental investigations of the 2PP microfabrication are presented in section 3.1. The effectiveness of 2PP initiation is closely related to the properties of the applied photoinitiator. On the example of Zr-based photosensitive hybrid it was demonstrated that interaction between the material matrix and the photoinitiator is critical, as it governs the photosensitive properties of the material. Due to the bathochromic effect of the Zr atom in presence of photoinitiator, the material absorption spectra is shifted to longer wavelength, when compared to the absorption of pure photoinitiator. Furthermore, this effect can be used in order to increase and tune the material sensitivity by using the properties of the polymer matrix instead of increasing the photoinitiator content alone. This finding is particularly useful for application where the high photoinitiator content is undesirable, e. g. tissue engineering or medical implant fabrication.

A further, common issue for photopolymerization, addressed in this chapter, was material shrinkage. It can result in structure deformation or even collapse, and therefore compromises the fidelity of the 2PP microfabrication and the quality of fabricated structures. In case of 2PP, volume reduction still has not been fully investigated. Unlike conventional methods, 2PP enables the study of the shrinking processes locally, at the microscale. In section 3.1.2, a simple, straightforward methodology allowing the evaluation of shrinkage was suggested. On the example of woodpile photonic crystal structures, built on supporting “legs”, it has been demonstrated that the degree of shrinkage is in direct relation with the applied irradiation dose. The structures produced at sufficiently high laser powers do not exhibit any measurable shrinkage, while at lower average laser powers shrinkage results in a structural reduction of up to 18%, and line width reduction of up to 35% of the original values. Furthermore, it is shown, that controlled shrinkage can be used in order to indirectly “improve” the structural resolution, i.e. to decrease feature sizes. Optical characterisation of photonic crystals, demonstrate that a woodpile, allowed to shrink to a full extent, exhibits a well expressed bandstop centered at 1330nm, indicating that homogeneous structure shrinkage could be achieved.

Section 3.1.2 is dedicated to 2PP structuring of pure organic materials, on the example of PEG-diacrylates. The general feature size dependencies on the irradiation dose have been measured for material formulations with different molecular weights. Structures with feature size well below micrometer can be easily realised by 2PP of these materials. PEG formulation with higher molecular weight in general results in voxels with lower aspect ratios, indicating higher shrinkage for this material. This investigation shows that as the molecular weight of the PEGda increases, the surface of the fabricated structures exhibits a less defined geometry and more expressed diffusion driven polymerization patterns. Application of 2PP technique for microstructuring of these materials brings together a very flexible microstructuring technology and a well known material platform, so addressing a wide area of potential applications in tissue engineering and biomedical fields.

Section 3.2 is dedicated to fabrication of microoptical elements by 2PP technique. Regarding the variety of possible surface profiles 2PP technique is superior to conventional approaches for fabrication of refractive optics. Furthermore, many polymeric materials, designed for optical applications, can be structures by 2PP technique. In the perspective to mass production of such microoptical elements, it is meaningful to use structures fabricated directly by means of 2PP microfabrication in order to prepare elastomeric molds for further replication with UV-micromolding.

Fabrication of 3D photonic crystals with various structural parameters, geometries and even shapes has been demonstrated by 2PP microfabrication. By setting the structural parameters, measured bandstops for these experimentally realised photonic crystals, can be precisely positioned in the near-IR spectral range at the telecommunication wavelengths. Higher order features observed in the measured FTIR spectra indicate high optical quality of the fabricated photonic crystal structures. On the example of woodpile structures it was shown that quality of the fabricated photonic crystals is sufficient to achieve a considerable PBG effect already for 4 unit cells along the testing direction. Dielectric filling fraction (Φ) is very important parameter, influencing the size and, to some extent, the exact position of the PBG. In 2PP microfabrication the Φ value is controlled independently of structural parameters of a photonic crystal, by adjusting the illumination dose. For woodpile architecture a minimal Φ value of 46 % is limited by the stability of the produced structures. Further reduction of Φ value, i.e. woodpiles rods cross-section, results in mechanically weak structures, which collapse during the developing step. It was observed that much lower values of Φ can be experimentally realised for spiral photonic crystals. This can be explained by the fact that, compared to woodpile, spiral structure resembles the diamond architecture much closer, while requiring less material. In addition, substantial spatial overlap between individual spirals contributes to better mechanical stability and lower Φ values for the spiral architecture.

For some future applications it is important to provide photonic crystals with nonlinear optical response. DR1 chromophore was chemically modified and added in a side-chain-main-chain manner to a conventionally used ORMOSIL based sol-gel. Such material containing NLO chromophore was successfully structured by 2PP technique. It is seen that the NLO chromophore stays inside the material throughout the processing. This method provides important guidelines for alternative material modifications with other nonlinear, electrooptic or photoactive materials. In conclusion, 2PP provides important rapid prototyping tool for the microscale all-optical circuit realisation.

Applications of 2PP microfabrication in biomedicine are presented in section 3.3. Microneedles produced by 2PP of hybrid photosensitive materials were tested for use in transdermal drug delivery. The optimisation of needle geometry for the lowest skin resistance during needle insertion has been performed. Flow studies using florescent dye solution provide evidence of controlled subcutaneous injection possibility through the microneedle. Results of this study indicate that microneedles created using the 2PP technique are suitable for *in vivo* use, and for the integration with the next generation MEMS- and NEMS-based drug delivery devices.

Another related application area is fabrication of microprosthesis. While conventional mass-produced implants do not sufficiently take individual patient anatomy into account, CAD/CAM rapid prototyping by 2PP may permit development of patient-specific geometries. Middle ear ossicular replacement prosthesis, fabricated by 2PP, has shown good mechanical properties and ease of handling. The appliedOrmocore material can be photostructured with high precision using 2PP technique, and has shown good biocompatibility. This study indicates high potential of 2PP technique for prototyping and fabrication of such patient-specific microimplants.

Finally flexibility of 2PP technique allows fabrication of complex 3D structures that can be used for guided cell growth. The fabrication of scaffolds with a desired structure in 3D is a very important task in tissue engineering. It has been demonstrated that CAD designed complex 3D structures with varying pores sizes can be generated by 2PP technique. For a given material the mechanical properties of such scaffold can be adjusted by changing the size and the positions of individual pores. These results demonstrate the great potential of 2PP technology for the fabrication of 3D scaffolds and test structures for tissue engineering. Structures with feature size similar to natural extracellular matrix can be produced. With respect to other techniques conventionally used for scaffold fabrication, 2PP technique allows to close the existing gap in structural parameters of resulting structures. The high reproducibility of 2PP microfabrication, for the first time allows the fabrication of large series of identical samples, and therefore, enables systematic studies of scaffold-cell and cell-cell interactions in a 3D system.

In perspective to further development of the 2PP technology, it is clear that further downscaling of the structural resolution is necessary in order to expand the number of applications of 2PP in the sector of nanotechnology. For example photonic crystals with the photonic bandgaps in the visible spectral range can be realised under the condition that structural parameters of these 3D structures can be scaled down accordingly. Indeed, recently a lot of efforts by scientific groups worldwide have been dedicated to this subject. Currently, 3D structures with features size as small as 65nm have been reported by 2PP using femtosecond laser at 520nm [HCH⁺07]. Naturally use of even shorter wavelengths should allow better focusing and result in smaller feature sizes. For this also materials and photoinitiators sensitive in the according spectral range have to be considered. Some possible solutions, based on elaboration of optical system, which were developed in order to improve the spatial resolution of multiphoton microscopy, can be readily applied for 2PP technique. Use of simple shaded ring filters helps to make the intensity distribution in the focus less asymmetric, and therefore improve axial resolution of fluorescence microscopy [MCI⁺03]. Similarly, 4-Pi illumination is a more sophisticated method, where two high NA microscope objectives are juxtaposed in order to allow constructive interference of their illumination wavefronts inside the sample. As a result, a close-to-spherical sharp excitation spot providing high spatial resolution can be realised [HLC⁺94]. Stimulated emission depletion (STED) is another possibility allowing to reduce the size of the excitation region in the fluorescence

microscopy [KEH01]. Here pairs of synchronised laser pulses at different wavelengths are applied. First pulse produces regular diffraction-limited excitation spot, while second donut shaped STED-pulse quenches excited molecules back to the ground state by stimulated emission. In the centre of the doughnut, fluorescence remains unaffected. Theoretically, using this approach the excitation spot can be narrowed down to the size of a single molecule. Practically STED-microscopy resolution as high as few tens of nanometres has been reported [KJD⁺00]. In 2PP STED can be applied to confine the photopolymerized region by quenching the photoinitiator molecules. Combination of both STED and 4-Pi microscopy is another, rather expensive, but possible route.

Potentially less expensive and more universal methods for improving the structural resolution rely on the modification of the materials applied for 2PP nanofabrication. Application of photoinitiators, specially designed to provide effective two-photon absorption has led to improved structural resolution [XDC⁺07]. Repolymerization patterns (see section 3.1.2) indicate that diffusion of radical molecules, away from the region where they were produced by the laser pulse, lead to unwanted increase of the polymerised volume. By adding radical quenchers chemical equivalent of STED effect, where excited photoinitiator molecules are spatially confined by local gradients of quencher concentrations, was realised [LD03, TSK05]. Here the diffusion of quencher molecules plays a critical role. Alternative solution is to reduce the diffusion and so provide better confinement of the polymerized volume. For this, solid materials, similar to ORMOSILs presented in this thesis can be used. Due to mineral network, formed during prebaking step, the mobility of the material molecules is already quite limited. Additional immobilisation of photoinitiator molecules, e. g. by chemical bonding onto such material network, should provide considerable improvement of the structural resolution.

Eventually the minimal resolution of 2PP technique will be limited by molecular size of applied materials. Further progress will rely on application of novel, possibly purely inorganic, photosensitive material systems.

With the development of turnkey femtosecond laser systems, 2PP technique enters the realm of industrial applications. First all-in-one laboratory scale systems for 2PP microfabrication are already commercially available [OC06]. Due to comparatively low throughput, it is very likely that such systems will be first used for rapid prototyping or fabrication of small series of microstructures. Few methods, allowing to increase throughput of 2PP by parallel processing with multiple laser spots, have already been demonstrated experimentally [MJM05, KTA⁺05]. In cases where large series of identical samples are required, structures produced by 2PP can be replicated by means of UV-micromolding or nanoimprinting [XKZ⁺96, LLF06]. While UV-micromolding presents a unique route for replication of 3D structures, well-established industrial scale techniques such as hot embossing or injection molding are most likely to be used for microoptical element fabrication.

The number of applications of 2PP technique will continue to grow. Micromechanical components produced by 2PP combined with on-chip microfluidic systems have already been demonstrated and are likely to get wider acceptance. A considerable advantage of 2PP for this

application is a possibility to fabricate complex interlocking micromechanical components in a single step, this way eliminating the assembly step [MIK03]. Metallization of structures produced by 2PP opens new possibilities through additional functionality, for applications where e.g. conductive 3D structures are required [FLP⁺06, HLA⁺05].

Realisation of 3D photonic crystals is a topic where 2PP still presents a unique technology capable of the widest number of possible solutions. The progress in this field will depend on the real demand of such structure realisation from the side of industry.

Without doubt, biomedical field will become one of the most important application areas of microstructures produced by 2PP. Scalability of this technique can provide solutions for a wide range of applications. Further reduction of the fabrication times will enable fast production of patient-specific prosthesis directly in the operational room environment. A set of data obtained with micro-coherence tomography of implantation site, can be used as an input for 2PP microfabrication system. Next generation intelligent transdermal drug delivery and blood sampling μ TAS-based (micro total chemical analysis system) solutions will rely on the use of microcapillaries or microneedles integrated into microfluidic chip. Here, 2PP presents a unique tool for rapid prototyping or manufacturing of small series of samples. Increasing throughput, by e.g. parallel processing or substantially accelerating the speed of fabrication, will bring 2PP approach closer industrial to scale manufacturing.

Fabrication of scaffolds for tissue engineering is certainly an application where 2PP offers enormous number of opportunities. When it comes to variation of possible 3D scaffold design and fabrication of series of identical samples no other technique possesses such flexibility as 2PP. Using 2PP microfabrication, for the first time enables systematic studies of scaffold-cell and cell-cell interactions in a 3D system. Eventually scaffolds fabricated from synthetic biodegradable polymers will be required. Such photosensitive materials are already available; their investigations are currently in progress at the Laser Zentrum Hannover. In perspective, 2PP can also provide means for adjustable surface-cell interaction mediated by nanostructures or biomolecules deposited by photografting [DKC⁺08]. Since the 2PP processing takes place at room temperature, the denaturation of proteins due to high temperatures can be avoided.

The future of the 2PP technique looks bright. The fact that there is still a lot of room for improvement in both fundamental, as well as technical aspects of this approach, indicates that it will continue to provide new solutions in different application areas.

References

- [ADM05] A. Al-Hiyasat, H. Darmani, M. Milhem, *Clin Oral Invest*, 9, 475 (2005).
- [AEH⁺07] L. E. Abolghasemi, S. Eaton, A. Hosseini, and P. R. Herman, Conference on Lasers and Electro-Optics/Quantum Electronics and Laser Science Conference and Photonic Applications Systems Technologies, OSA Technical Digest Series (CD) (Optical Society of America), paper CThN6., (2007).
- [Alb98] S. Albu et al., *American Journal of Otolaryngology* 19, 136-140, (1998).
- [Bar01] B. W. Barry, *Eur. J. Pharm. Sci.* 14, 101-114 (2001).
- [Bay00] A. Y. Bayazit, *Laryngoscope* 110, 176-177 (2000).
- [BC04] S. Basu, P. J. Campagnola, *Biomacromolecules*, 5, 572 (2004).
- [BCG⁺00] A. Blanco, E. Chomski, S. Grabtchak, M. Ibisate, S. John, S.W. Leonard, C. Lopez, F. Meseguer, H. Miguez, J.P. Mondla, G.A. Ozin, O. Toader and H.M. van Driel, *Nature*, 45, 437 (2000).
- [BE01] S. Buckley and R. Evershed, *Nature*, 413, 837 - 841 (2001).
- [BJ98] K. Busch and S. John, *Phys. Rev. E* 58, 3896, (1998).
- [BJB⁺03] A. Bertsch, S. Jiguet, P. Bernhard, P. Renaud, *MRS Symp. Proc.* 758 (2003)
- [BJH⁺99] J. F. Bertone, P. Jiang, K. S. Hwang, D. M. Mittleman, and V. L. Colvin, *Phys. Rev. Lett.*, 83, 300 (1999).
- [BKP⁺01] R. Buestrich, F. Kahlenberg, M. Popall, P. Dannberg, R. Müller-Fiedler, and O. Rösch, *J. Sol-Gel Sci. Technol.* 20, 181 (2001).
- [Bli86] C. van Blitterswijk et al., *Journal of Biomedical Materials Research* 20, 1197-217 (1986).
- [BLW⁺04] Busch Kurt, Lölkes Stefan, Wehrspohn Ralf, and B. Föll Helmut, *Photonic Crystals*, Wiley-VCH, Berlin, 2004
- [Boy92] R. W. Boyd, "Nonlinear optics", Academic, San Diego, 1992.
- [Bra86] D. Brackmann, *Annals of Otology, Rhinology, and Laryngology* 95, 76-77 (1986)
- [BS90] C. J. Brinker, and W. G. Scherer, *Sol-Gel Science*, Academic Press, New York, 1990.
- [BSS⁺98] R. Biswas, M. M. Sigalas, G. Subramania, and K. M. Ho, *Phys. Rev. B* 57, 3701 (1998).
- [CAB⁺99] B. Cumpston, S. Ananthavel, S. Barlow, D. Dyer, J. Ehrlich, L. Erskine, A. Heikal, S. Kuebler, I. Lee, D. McCord-Maughon, J. Qin, H. Rockel, M. Rumi, X. Wu, S. Marder, J. Perry, *Nature*, 398, 51–54 (1999)
- [CF89] S. Chong, H. L. Fung, "Transdermal drug delivery systems: pharmacokinetics, clinical efficacy, and tolerance development". In: J. Hadgraft, R. H. Guy, eds. *Transdermal Drug Delivery: Developmental Issues and Research Initiatives*, New York Marcel Dekker; 135, 1989.
- [CJT03] A. Chutinan, S. John, and O. Toader, *Phys. Rev. Lett.*, 90, 123901 (2003).
- [CN98] A. Chutinan, S. Noda, *Phys. Rev B* 57, R2006 (1998)

- [CN99] A. Chutinan and S. Noda, *J. Opt. Soc. Am. B* 16, 240-244 (1999).
- [Col99] Colletti V et al., *Otolaryngology-Head and Neck Surgery* 120, 437-44, (1999).
- [CPR⁺98] D. H. Choi, J. H. Park, T. H. Rhee, N. Kim, and S.-D. Lee, *Chem. Mater.* 10, 705-709 (1998).
- [Cru94] A. De la Cruz et al., *Otolaryngologic Clinics of North America* 27, 799-811, (1994).
- [CSH⁺00] M. Campbell, D. N. Sharp, M. T. Harrison, R. G. Denning, and A. J. Turberfield, *Nature London* 404, 53 (2000).
- [CTT⁺06] Y.-S Chen, A. Tal, D. B. Torrance, S. M. Kuebler, *Adv. Funct. Mater.*, 16, 1739, (2006).
- [Cur00] O. Cura et al., *Revue De Laryngologie Otologie Rhinologie* 121, 87-90 (2000)
- [Dan98] R. L. Daniels et al., *Laryngoscope* 108, 1674-1681 (1998).
- [Dec94] C. Decker, *Acta Polymer* 43, 333-347 (1994).
- [Dec98] C. Decker, *Polymer International*, 45, 133-141, (1998).
- [DFW⁺04] M. Deubel, G. von Freymann, M. Wegener, S. Pereira, K. Busch, C. M. Soukoulis, *Nat. Mater.*, 3, 444 (2004).
- [DKC⁺08] V. Dinca, E. Kasotakis, J. Catherine, A. Mourka, A. Ranella, A. Ovsianikov, B. N. Chichkov, M. Farsari, A. Mitraki, and C. Fotakis, *Nano Lett.*, 8, 538-543 (2008).
- [DJN⁺06] A. Doraiswamy, C. Jin, R.J. Narayan, P. Mageswaran, P. Mente, R. Modi, R. Auyeung, D.B. Chrisey, A. Ovsianikov, B. Chichkov, *Acta Biomaterialia*, 2, 267-275 (2006).
- [DPN⁺05] A. Doraiswamy, T. Patz, R. Narayan, B.N. Chichkov, A. Ovsianikov, R. Houbertz, R. Modi, R. Auyeung, D.B. Chrisey, *Mater. Res. Soc. Symp. Proc.* 845, AA2.4.1 (2005).
- [DS87] R. C. Denney and R. Sinclair, *Visible and Ultraviolet Spectroscopy*, Analytical Chemistry, John Wiley 1987.
- [DSW90] W. Denk, J. H. Strickler, W. W. Webb, *Science*, 248, 73-76 (1990)
- [DWL⁺05] M. Deubel, M. Wegener, S. Linden, and G. von Freymann, *Appl. Phys. Lett.* 87, 221104 (2005).
- [EDM⁺07] Y. Enami, C. T. Derose, D. Mathine, C. Loychik, C. Greenlee, R. A. Norwood, T. D. Kim, J. Luo, Y. Tian, A. K. Y. Jen, and N. Peyghambarian, *Nature Photonics* 1, 180-185 (2007).
- [FCJ⁺04] G. von Freymann, T. Chan, S. John, V. Kitaev, G. A. Ozin, M. Deubel and M. Wegener, *Photonics and Nanostructures - Fundamentals and Applications*, 2, 191 (2004).
- [FLP⁺06] R. A. Farrer, C. N. LaFratta, L. Li, J. Praino, M. J. Naughton, B. E. A. Saleh, M. C. Teich, J. T. Fourkas, *J. Am. Chem. Soc.*, 128, 1796 (2006).
- [Fly96] G. L. Flynn, "Cutaneous and transdermal delivery: Processes and systems of delivery", In: G. S. Banker, C. T. Rhodes, eds. *Modern Pharmaceutics*. New York, NY: Marcel Dekker; 239-299, 1996.

- [FNT⁺97] K. Fujimoto, A. Nagafuch, S. Tsukita, A. Kuraoka, A. Ohokuma, Y. Shibata, *J Cell Sci.* 110, 311-322 (1997).
- [FR93] J. P. Fouassier, and J. F. Rabek, *Radiation Curing in Polymer Science and Technology Volume III: Polymerizations Mechanisms*, Elsevier Applied Science, 1993.
- [FTT⁺06] F. Formanek, N. Takeyasu, T. Tanaka, K. Chiyoda, A. Ishikawa, S. Kawata, *Opt. Express* 14, 800 (2006).
- [FTC⁺06] F. Formanek, N. Takeyasu, T. Tanaka, K. Chiyoda, A. Ishikawa, S. Kawata, *Appl. Phys. Lett.*, 88, 083110 (2006).
- [GCL⁺01] H. Goudket, M. Canva, Y. Levy, F. Chaput, F., and J.P. Boilot, *J. Appl. Phys.* 90, 6044-6047 (2001).
- [Gla88] M. Glasscock et al., *Archives of Otolaryngology-Head & Neck Surgery* 114, 1252-1255 (1988)
- [GLB⁺03] H. Gardeniers, R. Luttge, E. Berenschot, M. de Boer, S. Yeshurun, M. Hefetz, R. van't Oever, A. van den Berg, *J. of Microelectromechanical Systems* 12, 855-862 (2003).
- [GMU⁺02] F. García-Santamaría, H.T. Miyazaki, A. Urquía, M. Ibisate, M. Belmonte, N. Shinya, F. Meseguer, C. López, *Adv. Mat.*, 14, 1144 (2002).
- [Gol00] R. Goldenberg et al., *Otolaryngology-Head and Neck Surgery* 122, 635-642, (2000).
- [Goo94] R. L. Goode et al., *Otolaryngologic Clinics of North America* 27, 663-675 (1994).
- [Gro85] J. Grote, *American Journal of Otology* 6, 269–271 (1985).
- [Gro86] J. Grote et al., *Annals of Otology, Rhinology, and Laryngology* 123, (1986).
- [GS03] P. Griss, G. Stemme, *J. of Microelectromechanical Systems* 12, 296-301 (2003).
- [GXL⁺04] B. Gates, Q. Xu, J. Love, D. Wolfe, G. Whitesides, *Annual Review of Materials Research* 34, 339-372 (2004).
- [GXZ⁺06] R. Guo, S. Xiao, X. Zhai, J. Li, A. Xia, W. Huang, *Opt. Express.*, 14, 810 (2006).
- [Haa00] K.-H. Haas, *Adv. Eng. Mat.*, 2, 571 (2000).
- [HCH⁺07] W. Haske, V. Chen, J. Hales, W. Dong, S. Barlow, S. Marder, and J. Perry, *Opt. Express* 15, 3426-3436 (2007).
- [HCS⁺94] K. M. Ho, C. T. Chan, C. M. Soukoulis, R. Biswas and M. Sigalas, *Solid State Communications* 89, 413-416 (1994).
- [HKM⁺08] B. Harley, H-D. Kim, M. Zaman, I. Yannas, D. Lauffenburger, L. Gibson, *Biophys. J.* online first (2008).
- [HLA⁺05] R. T. Hill, J. L. Lyon, R. Allen, K. J. Stevenson, J. B. Shear, *J. Am. Chem. Soc.*, 127, 10707 (2005).
- [HLC⁺94] S. W. Hell, S. Lindek, C. Cremer and E. H. K. Stelzer, *Appl. Phys. Lett.* 64, 1335-1338 (1994).
- [Hut01] D. W. Hutmacher, *J. Biomater. Sci. Polymer Edn.*, 12, 107-124 (2001).

- [HVP⁺02] N. P. Huang, J. Voros, S. M. De Paul, M. Textor, N. D. Spencer, *Langmuir*, 18, 220–230 (2002).
- [HWP63] J. J. Hopfield, J. M. Worlock, K. J. Park, *Phys. Rev. Lett.*, 11, 414 (1963).
- [Ino95] S. Inoue, “*Handbook of Optics*”, McGraw Hill, Inc., New York., 1995
- [IO04] K. Inoue and K. Ohtaka, eds., *Photonic Crystals, Physics, Fabrication and Applications*, Springer, 2004.
- [Jah83] K. Jahnke et al. *Biomaterials*, 4 137 (1983)
- [JBH⁺99] P. Jiang, J. F. Bertone, K. S. Hwang, and V. L. Colvin, *Chem. Mater.*, 11, 2132 (1999).
- [JDW08] J. D. Joannopoulos, R. D. Meade, & J. N. Winn, *Photonic Crystals: Molding the Flow of Light*, 2nd Edition, Princeton NJ: Princeton University Press, 2008.
- [JJ01] Steven G. Johnson, John D. Joannopoulos , *Photonic Crystals: The Road from Theory to Practice*, Springer, 2001.
- [JMS⁺05] S. Juodkazis, V. Mizeikis, K.-K. Seet, M. Miwa and H. Misawa, *Nanotechnology*, 16, 846–849 (2005).
- [Joh02] S. G. Johnson “MIT Photonic-Bands,” (Massachusetts Institute of Technology 2002) http://ab-initio.mit.edu/wiki/index.php/MIT_Photonic_Bands
- [Joh87] S. John, *Phys. Rev. Lett.* 58, 2486–2489 (1987).
- [JPS⁺99] M. Joshi, H. Pudavar, J. Swiatkiewicz, P. Prasad, B. Reinhardt, *Appl. Phys. Lett.*, 74, 170 (1999).
- [JRK⁺04] R. Janda, J. Roulet, M. Kaminsky, G. Steffin, M. Latta, *Eur J Oral Sci*, 112, 474 (2004).
- [JVF97] J. D. Joannopoulos, P. R. Villeneuve, and S. Fan, *Nature* 386, 143–149, (1997).
- [KBL⁺05] S. Klein, A. Barsella, H. Leblond, H. Bulou, A. Fort, C. Andraud, G. Lemerrier, J. C. Mulatier, K. Dorkenoo, *Appl. Phys. Lett.*, 86, 211118 (2005)
- [KEH01] T. A. Klar, E. Engel and S. W. Hell, *Phys. Rev. E* 64, 066611-066619 (2001).
- [KG61] W. Kaiser and C. Garrett, *Phys. Rev. Lett.* 7, 229-231 (1961).
- [KJD⁺00] T. A. Klar, S. Jakobs, M. Dyba, A. Egner, S. W. Hell, *Proceedings of the National Academy of Sciences of the United States of America*, 97, 8206 (2000).
- [KMJ⁺01] T. Kondo, S. Matsuo, S. Juodkazis, and H. Misawa, *Appl. Phys. Lett.* 79, 725-727 (2001).
- [KP05] F. Kahlenberg and M. Popall, *Mater. Res. Soc. Symp.* 847, EE14.4.1 (2005).
- [KRP02] W.-G. Koh, A. Revzin, and M. V. Pishko, *Langmuir*, 18, 2459 -2462, (2002).
- [KS02] M. Kaur and A. K. Srivastava, “Photopolymerization: A Review.” *Journal of Macromolecule Science- Polymer Reviews*, 481-512 (2002)
- [KSD⁺03] K. Kaneko, H. B. Sun, X. M. Duan, and S. Kawata, *Appl. Phys. Lett.* 83, 2091 (2003).
- [KTA⁺05] J. Kato, N. Takeyasu, Y. Adachi, H-B. Sun, and S. Kawata, *Appl. Phys. Lett.* 86, (2005).
- [LB02] V. A. Liu and S. N. Bhatia, *Biomed. Microdev.*, 4, 257–266 (2002).

- [LBB⁺05] J.-M. Lourtioz, H. Benisty, V. Berger, J.-M. Gerard, D. Maystre, A. Tchelmonov, *Photonic Crystals: Towards Nanoscale Photonic Devices*, Springer-Verlag Berlin and Heidelberg, 2005.
- [LBF⁺04] C. LaFratta, T. Baldacchini, R. Farrer, J. Fourkas, M. Teich, B. Saleh, M. Naughton, *J. Phys. Chem. B*, 108, 11256 (2004).
- [LCH⁺06] A. Ledermann, L. Cademartiri, M. Hermatschweiler, C. Toninelli, G. A. Ozin, D. S. Wiersma, M. Wegener, G. von Freymann, *Nature Mater.*, 5, 942 (2006).
- [LCK06] N. Lee, S. Choi, and S. Kang, *Appl. Phys. Lett.* 88, 073101 (2006).
- [LD03] C. A. Leatherdale, R. J. DeVoe, *Proceedings of SPIE-The International Society for Optical Engineering*, 5211, 112 (2003).
- [LFH⁺98] S. Y. Lin, J. G. Fleming, D. L. Hetherington, B. K. Smith, R. Biswas, K. M. Ho, M. M. Sigalas, W. Zubrzycki, S. R. Kurtz, and J. Bur, *Nature* 394, 251-253 (1998).
- [LHD05] Y. Lin, P.R. Herman, and K. Darmawikarta, *Appl. Phys. Lett.* 86, 071117 (2005).
- [Lim02] C. Lim et al. *International Journal of Advanced Manufacturing Technology* 20, 44-49, (2002).
- [Liu96] D.-M. Liu, *J. of Mater. Sci. Lett.*, 15, 419-421 (1996).
- [LLF06] C. LaFratta, L. Li, J. Fourkas, *Proc. Natl. Acad. Sci. USA*, 103, 8589 (2006).
- [LOw71] J. Larsen, and W. Owen, *Trans. Amer. Micros. Soc.*, 90, 294-308 (1971).
- [LPB02] W. M. Lee, S. A. Pruzinsky, and P. V. Braun, *Adv. Mater.*, 14, 271 (2002).
- [LQY⁺08] Y. Li, F. Qi, H. Yang, Q. Gong, X. Dong and X. Duan, *Nanotechnology* 19, 055303 (2008)
- [LQY⁺08] Y. Li, F. Qi, H. Yang, Q. Gong, X. Dong and X. Duan, *Nanotechnology* 19, 055303 (2008).
- [LR07] A. Lavrinenko, S. Romanov, PECS-VII Monterey, USA, April 8-11 (2007)
- [Mad90] J. Maddox, "Photonic band-gaps bite the dust," *Nature* 348, 481 (1990).
- [Mah95] D. Mahoney, *Computer Graphics World* 18, 42-48 (1995).
- [Man90] C. Mangham et al., *Annals of Otolaryngology, Rhinology, and Laryngology* 99, 112-116 (1990).
- [Mar03] S. Maruo et. al., *MRS Symp. Proc. Vol. 739* (2003).
- [Mar06] S. Maruo, *Polym. Prepr. Am. Chem. Soc., Div. Polym. Chem.*, 94, 101 (2006).
- [MCI⁺03] M. Martinez-Corral, C. Ibáñez-López, G. Saavedra, and M. Caballero, *Opt. Express* 11, 1740-1745 (2003).
- [MDM⁺07] V. Mocella, P. Dardano, L. Moretti, and I. Rendina, *Opt. Express* 15, 6605-6611 (2007).
- [Mer99] S. Merchant et al., *American Journal of Otolaryngology* 18, 139-154 (1999).
- [MFS⁺02] P. Markowicz, Ch. Friend, Y. Shen, J. Swiatkiewicz, P. N. Prasad, O. Toader, S. John, and R.W. Boyd., *Opt. Lett.*, 27, 351 (2002).

- [MGP29] M. Goepfert-Mayer, „Über die Wahrscheinlichkeit des Zusammenwirkens zweier Lichtquanten in einen Elementarakt“, *Naturwissenschaften* 17, 932 (1929).
- [MGP31] M. Göppert-Mayer, "Über Elementarakte mit zwei Quantensprüngen". *Ann Phys* 9, 273–95 (1931).
- [MHF00] S. Monneret, P. Huguet-Chantôme, and F. Flory, *J. Opt. A* 2, 188 (2000).
- [MIK03] S. Maruo, K. Ikuta, H. Korogi, *Appl. Phys. Lett.*, 82, 133 (2003).
- [Mit01] S. Mitragotri, *J Controlled Rel.* 71, 23-29 (2001).
- [MJM05] S. Matsuo, S. Juodkazis, and H. Misawa, *Appl. Phys. A.* 80, 683-685 (2005).
- [MJT⁺07] V. Mizeikis, S. Juodkazis, R. Tarozaitė, J. Juodkazyte, K. Juodkazis, and H. Misawa, *Opt. Express* 15, 8454-8464 (2007).
- [MMB⁺03] Yu. Miklyaev, D. Meisel, A. Blanco, G. von Freymann, K. Busch, W. Koch, C. Enkrich, M. Deubel, and M. Wegener, *Appl. Phys. Lett.* 82, 1284 (2003).
- [MNK97] S Maruo, O. Nakamura, S. Kawata, *Opt. Lett.*, 22,132 (1997).
- [Mor98] W. Moretz, *Laryngoscope* 108, 1-12, (1998).
- [MT04] M. Maldovan and E. L. Thomas, *Nature Materials*, 3 593-600 (2004)
- [Mur05] E. Murugasu et al., *Otology and neurotology* 26, 572-82 (2005).
- [MYT⁺02] H. Míguez, S. M. Yang, N. Tétreault. and G. A. Ozin, *Adv. Mater.*, 14, 1805 (2002).
- [NAT⁺05] A. Ngezhayo, B. Altmann, M. Steffens, H. Kolb, *J. Membr. Biol.*, **204** 137-144 (2005).
- [NB03] S. Noda and T. Baba (Eds.), *Roadmap on Photonic Crystals*, Kluwer Academic Publishers, 2003
- [NHB⁺01] M. C. Netti, A. Harris, J. J. Baumberg, D. M. Whittaker, M. B. D. Charlton, M. E. Zoorob, and G. J. Parker, *Phys. Rev. Lett.*, 86, 1526 (2001).
- [NTY⁺00] S. Noda, K. Tomoda, N. Yamamoto, and A. Chutinan, *Science* 289, 604-606 (2000).
- [NV01] D. J. Norris, Yu. A. Vlasov, *Adv. Mat.*, 13, 371-376 (2001).
- [NYI⁺99] S. Noda, N. Yamamoto, M. Imada, H. Kobayashi, M. Okano, *J. of Lightwave Technology*, 17, 1948 (1999).
- [OC06] A. Ostendorf and B. N. Chichkov, *Photonics Spectra* (2006).
- [OCA⁺07] A. Ovsianikov, B. N. Chichkov, O. Adunka, H. Pillsbury, A. Doraiswamy, R. J. Narayan, *Applied Surface Science*, 253, 6603 (2007).
- [OPO⁺07] Obata, K.; Passinger, S.; Ostendorf, A.; Chichkov, B. N., *International Conference on Applications of Lasers and Electro-Optics ICALEO*, Orlando, FL, s. 29-31 (2007).
- [OS04] G. J. Opitck, J. E. Scheffler, *Expert Review of Proteomics* 1, 57-66 (2004).
- [OSN⁺07] A. Ovsianikov, S. Schlie, A. Ngezhayo, A. Haverich, and B. N. Chichkov, *J Tissue Eng Regen Med*, 1 443-449 (2007).
- [PB07] A. Pikulin and N. Bityurin, *Phys. Rev. B* 75, 195430 (2007).

- [PCE⁺00] J. D. Pitts, P. J. Campagnola, G. A. Epling, S. L. Goodman, *Macromolecules*, 33, 151 (2000).
- [PL05] R. O. P. Potts, R. A. Lobo, *Obstetrics and Gynecology* 105, 953-961 (2005).
- [PLY⁺04] S. H. Park, T. W. Lim, D. Y. Yang, H. J. Kong, R. H. Kim, K. S. Kim and K. S. Lee, *Bull. Korean Chem. Soc.* 8, 1119 (2004).
- [PML04] M. R. Prausnitz, S. Mitragotri, R. Langer, *Nature Reviews Drug Discovery* 3, 115-124 (2004)
- [Pra04] M. R. Prausnitz, *Advanced Drug Delivery Reviews* 56, 581-587 (2004).
- [QLT⁺07] F. Qi, Y. Li, D. Tan, H. Yang, and Q. Gong, *Opt. Express* 15, 971-976 (2007).
- [RCL⁺95] D. Riehl, F. Chaput, Y. Levy, J. P. Boilot, F. Kajzar and P. A. Chollet, *Chem.Phys.Lett.* 245, 36-40 (1995).
- [RPC⁺06] C. Reinhardt, S. Passinger, B. Chichkov, C. Marquart, I. Radko, and S. Bozhevolnyi, *Optics Letters* 31, 1307 (2006).
- [Rof82] C. G. Roffey, *Photopolymerization of Surface Coatings*, New York: John Wiley & Sons, 1982.
- [Rom01] S. Romanov et al., *Phys. Rev. E*, 63 056603-5 (2001).
- [Rom07] S. Romanov et al., *Appl. Phys. Lett.*, 90 133101-3 (2007).
- [RSR⁺03] T. Roy, J. Simon, J. Ricci, E. Rekow, V. Thompson, J. Parsons, *J. Biomed Mater Res*, 66A 283-291 (2003).
- [Sak05] K. Sakoda, *Optical Properties of Photonic Crystals*, Springer, 2005.
- [Sch06] S. Schmerber et al. *European Archives of Otorhinolaryngology* 263, 347–354 (2006).
- [Sch98] K. Schwager *European Archives of Otorhinolaryngology* 255, 396–401 (1998).
- [SEO⁺03] J. Serbin, A. Egbert, A. Ostendorf, B. N. Chichkov, R. Houbertz, G. Domann, J. Schulz, C. Cronauer, L. Frohlich, M. Popall, *Opt. Lett.*, 28, 301 (2003).
- [SG02] M. Straub and M. Gu, *Opt. Lett.* 27, 1824-1826 (2002)
- [SG05] J. Serbin and M. Gu, *J. Appl. Phys.*, 98, 123101 (2005).
- [SHB⁺04] K. Schafer, J. Hales, M. Balu, K. Belfield, E. van Stryland, D. Hagan, J. Photochem. Photobiol A, 162, 497-502 (2004).
- [She84] Y. R. Shen, "The principles of nonlinear optics", Wiley, New York, 1984.
- [SJJ⁺06] K.-K. Seet, S. Juodkasis, V. Jarutis, and H. Misawa, *Appl. Phys. Lett.* 89, 024106 (2006).
- [SK00] S. Shoji and S. Kawata, *Appl. Phys. Lett.*, 76, 2668 (2000).
- [SMM⁺05] K. K. Seet, V. Mizeikis, S. Matsuo, S. Juodkasis, H. Misawa, *Adv. Mater.*, 17, 541 (2005).
- [SMM99] H. B. Sun, S. Matsuo and H. Misawa, *Appl. Phys. Lett.* 74, 786 (1999)
- [SMX⁺01] H.-B. Sun, V. Mizeikis, Y. Xu, S. Juodkasis, J.-Y. Ye, S. Matsuo, H. Misawa, *Appl. Phys. Lett.*, 79, 1 (2001).
- [SNF⁺04] M. Straub, L. H. Nguyen, A. Fazlic, M. Gu, *Opt. Mater.*, 27, 359 (2004).
- [SNO⁺07] S. Schlie, A. Ngezahayo, A. Ovsianikov, T. Fabian, H.-A. Kolb, H. Haferkamp, B. N. Chichkov, *J. Biomater. Appl.*, 22, 275-287 (2007).

- [SOC04] J. Serbin, A. Ovsianikov, and B. Chichkov, *Opt. Express* 12, 5221-5228 (2004).
- [Sot03] C. M. Sotomayor Torres (Ed.), *Alternative Lithography Unleashing the potentials of Nanotechnology*, Kluwer Academic Plenum Publishers, Chapter 8, (2003).
- [SSK03] S. Shoji, H.-B. Sun, and S. Kawata, *Appl. Phys. Lett.*, 83, 608 (2003).
- [SSW⁺05] R. K. Sivamani, B. Stoeber, G. C. Wu, H. Zhai, D. Liepmann, H. Maibach, *Skin Research and Technology* 11, 152-156 (2005).
- [Str99] C. Stupp et al. *Laryngorhinootologie* 78, 299–303 (1999).
- [SKX⁺00] H. Sun, T. Kawakami, Y. Xu, J. Ye, S. Matuso, H. Misawa, M. Miwa, and R. Kaneko, *Opt Lett* 25, 1110 (2000).
- [Sve98] O. Svelto, *Principles of Lasers*, Springer, 4th ed. 1998
- [SVK95] S. Seyfert, A. Vogt, D. Kabbeck-Kupijai, *Biomaterials*, 16, 201-207 (1995).
- [TFD⁺06] N. Tétreault, G. von Freymann, M. Deubel, M. Hermatschweiler, F. Pérez-Willard, S. John, M. Wegener, G. A. Ozin, *Adv. Mat.*, 18, 457 (2006).
- [TLQ⁺07] D. Tan, Y. Li, F. Qi, H. Yang, Q. Gong, X. Dong, and X. Duan, *Appl. Phys. Lett.* 90, 071106 (2007).
- [TRS⁺02] D. Thomann, D. R. Rines, P. K. Sorger, G. Danuser, *J. of Microscopy*, 208, 49-64 (2002).
- [TSK05] K. Takada, H.-B. Sun, and S. Kawata, *Appl. Phys. Lett.* 86, 071122 (2005)
- [TSM72] P.K. Tien, G. Smolinsky, R. J. Martin, *Applied Optics* 11, 637 (1972).
- [VVH03] S. VandeVondele, J. Voros, J. A. Hubbell, *Biotechnol. Bioeng.*, 82, 784– 790 (2003).
- [Wan99] X. Wang et al. *Otolaryngology-Head and Neck Surgery* 121, 606-609 (1999).
- [Weh94] R. Wehrs, *Otolaryngologic Clinics of North America* 27, 677-688 (1994).
- [WRZ⁺06] F. C. Wippermann, D. Radtke, U. Zeitner, J. W. Duparre, A. Tunnermann, M. Amberg, S. Sinzinger, C. Reinhardt, A. Ovsianikov, and B. N. Chichkov, *Proc. SPIE Vol. 6288, “Current Developments in lens design and optical engineering VII”*, San Diego, 14-15. 8 (2006).
- [WTY⁺03] G. P. Wang, C. Tan, Y. Yi and H. Shan, *Jour. Mod. Opt.*, 50, 2155 (2003).
- [www.MR] www.microresist.de
- [www.SJ] <http://www.stjohn.org>
© 2000-2008 The StayWell Company, 780 Township Line Road, Yardley, PA 19067.
- [www.WK] http://en.wikipedia.org/wiki/Tissue_engineering
Wikipedia® is a registered trademark of the Wikimedia Foundation
- [WXS⁺03] X. Wang, J. F. Xu, H. M. Su, Z. H. Zeng, Y. L. Chen, H. Z. Wang, Y. K. Pang, and W. Y. Tam, *Appl. Phys. Lett.* 82, 2212-2214 (2003).
- [XAB⁺03] J. Xu, S. Aubonnet, H. F. Barry, B. D. MacCraith, *Materials Letters*, 57, 4276-4281 (2003).
- [XCD⁺07] J-F. Xing, W-Q. Chen, X-Z. Dong, T. Tanaka, X-Y. Fang, X-M. Duan, and S. Kawata, *J. Photochem. Photobiol. A*, 189, 398-404 (2007)

- [XDC⁺07] J.-F. Xing, X.-Z. Dong, W.-Q. Chen, X.-M. Duan, N. Takeyasu, T. Tanaka, and S. Kawata, *Appl. Phys. Lett.* 90, 131106 (2007).
- [XFH⁺02] X. Xu, G. Friedman, K. D. Humfeld, S. A. Majetich, and S. A. Asher, *Chem. Mater.*, 14, 1249 (2002).
- [XKZ⁺96] Y. Xia, E. Kim, X.M. Zhao, J.A. Rogers, M. Prentiss and G.M. Whitesides, *Science* 273, 347–349 (1996).
- [Yab87] E. Yablonovitch, *Phys. Rev. Lett.*, 58, 2059–2062 (1987).
- [YNS97] N. Yamamoto, S. Noda, and A. Sasaki, *Jpn. J. Appl. Phys.*, 36, 1907 (1997).
- [Yok03] Yokoyama et. Al., *Appl. Phys. Lett.* 82, (2003).
- [You87] R.J. Young, *Introduction to Polymers*, Chapman & Hall 1987
- [YX02] Y. Yin, and Y. Xia, *Adv. Mater.*, 14, 605, (2002).
- [YZa04] M. Yang, and J. Zahn, *Biomedical Microdevices* 6, 177-182 (2004).
- [Zah00] T. Zahnert et al. *American Journal of Otology* 21, 322-328 (2000).
- [ZCP05] W. X. Zhou and M. B. Chan-Park, *Lab Chip*, 5, 512–518 (2005).
- [ZKB⁺02] W. Zhou, S. M. Kuebler, K. L. Braun, T. Yu, J. K. Cammack, C. K. Ober, J. W. Perry, S. R. Marder, *Science* 296, 1106-1109 (2002).
- [ZKB⁺02] W. Zhou, S. M. Kuebler, K. L. Braun, T. Yu, J. K. Cammack, C. K. Ober, J. W. Perry, S. R. Marder, *Science*, 296, 1106 (2002).
- [ZLF06] H. X. Zhang, D. Lu, M. Fallahi, *Optical Materials* 28, 992–999 (2006).
- [ZLL⁺04] H. X. Zhang, D. Lu, T. Liu, M. Mansuripur, and M. Fallahi, *Appl. Phys. Lett.* 85, 4275-4277 (2004).
- [ZLP⁺04] H. X. Zhang, D. Lu, N. Peyghambarian, M. Fallahi, J. D. Luo, B. Q. Chen, and A. K.-Y. Jen, *Opt.Lett.* 30, 117-119 (2004).
- [ZPC04] V. G. Zarnitsyn, M. R. Prausnitz, Y. A. Chizmadzhev, *Biologicheskie Membrany* 21, 355-373 (2004).

List of Own Publications:

- J. Serbin, A. Ovsianikov, B.N. Chichkov, Fabrication of woodpile structures by two-photon polymerization and investigation of their optical properties, *Opt. Express*, 12, 5221 (2004).
- F. Korte, J. Koch, J. Serbin, A. Ovsianikov, B.N. Chichkov, 3D nanostructuring with femtosecond laser pulses, *IEEE Transactions on nanotechnology*, 3, 468 (2004).
- R. J. Narayan, C. Jin, T. Patz, A. Doraiswamy, R. Modi, D. B. Chrisey, Y-Y. Su, S.J. Lin, A. Ovsianikov, and B. N. Chichkov, *Laser Processing of Advanced Biomaterials*, *Advanced Materials & Processes*, 39, April (2005).
- R. J. Narayan, C. Jin, A. Doraiswamy, I. N. Mihailescu, M. Jelinek, A. Ovsianikov, B. N. Chichkov, D. B. Chrisey, *Laser processing of advanced bioceramics*, *Advanced Engineering Materials*, 7:12, 1083 (2005).
- A. Doraiswamy, C. Jin, R.J. Narayan, P. Mageswaran, P. Mente, R. Modi, R. Auyeung, D.B. Chrisey, A. Ovsianikov, B. Chichkov, Two photon induced polymerization of organic–inorganic hybrid biomaterials for microstructured medical devices, *Acta Biomaterialia*, 2, 267 (2006).
- A. Ovsianikov, B. N. Chichkov, O. Adunka, H. Pillsbury, A. Doraiswamy, R. J. Narayan, *Rapid Prototyping of Ossicular Replacement Prostheses*, *Applied Surface Science*, 253, 6603 (2007).
- A. Ovsianikov, B. N. Chichkov, P. Mente, N. A. Monteiro-Riviere, A. Doraiswamy, R. J. Narayan, Two photon polymerization of polymer-ceramic hybrid materials for transdermal drug delivery, *International Journal of Applied Ceramic Technology*, *Int. J. Appl. Ceram. Technol.*, 4, 22 (2007)
- S. Schlie, A. Ngezhayo, A. Ovsianikov, T. Fabian, H.-A. Kolb, H. Haferkamp, B. N. Chichkov, Three-dimensional cell growth on structures fabricated from ORMOCER® by two-photon polymerization technique, *J. Biomater Appl*, 22, 275-287 (2007).
- A. Ovsianikov, A. Ostendorf, B. N. Chichkov, Three-dimensional photofabrication with femtosecond lasers for applications in photonics and biomedicine, *Applied Surface Science*, 253, 6599 (2007)
- R. Houbretz, P. Declerck, S. Passinger, A. Ovsianikov, J. Serbin, and B.N. Chichkov, Investigations on the generation of photonic crystals using two-photon polymerization (2PP) of inorganic-organic hybrid polymers with ultra-short laser pulses, *DFG / Phoc - Physica Status Solidi*, *phys. stat. sol. (a)* 204, No. 11, 3662–3675 (2007).
- A. Ovsianikov, S. Schlie, A. Ngezhayo, A. Haverich, and B. N. Chichkov, Two-photon polymerization technique for microfabrication of CAD designed three-dimensional scaffolds from commercially available photosensitive materials, *J Tissue Eng Regen Med*, 1, 443-449 (2007).
- N. Grossman, A. Ovsianikov, A. Petrov, M. Eich, B. Chichkov, Investigation of optical properties of circular spiral photonic crystals, *Opt. Express*, 15, 20, 13236 (2007)
- M. Farsari, A. Ovsianikov, M. Vamvakaki, I. Sakellari, D. Gray, B.N. Chichkov, and C. Fotakis, *Appl. Phys. A*, 93, 11–15 (2008).
- V. Dinca, E. Kasotakis, J. Catherine, A. Mourka, A. Ranella, A. Ovsianikov, B. N. Chichkov, M. Farsari, A. Mitraki, and C. Fotakis, *Directed Three-Dimensional Patterning of Self-*

Assembled Peptide Fibrils, Nanoletters, ASAP Article 10.1021/nl072798r, Nano Lett., 8, 2, 538-543 (2008).

A. Ovsianikov, J. Viertl, M. Oubaha, B. MacCraith, I. Sakellari, A. Giakoumaki, D. Gray, M. Vamvakaki, M. Farsari, C. Fotakis, and B. Chichkov, Ultra-Low Shrinkage Hybrid Photosensitive Material for Two-Photon Polymerization Microfabrication, ASC Nano, 2, 2257-2262 (2008).

A. Ovsianikov, A. Gaidukeviciute, M. Oubaha, B. MacCraith, I. Sakellari, A. Giakoumaki, D. Gray, M. Vamvakaki, M. Farsari, C. Fotakis, and B. N. Chichkov, Two-Photon Polymerization of Hybrid Sol-Gel Materials for Photonics Applications, Laser Chemistry, Article ID 493059, 7 pages (2008).

Book chapters:

A. Ovsianikov, S. Passinger, R Houbertz, and B.N. Chichkov, Three Dimensional Material Processing with Femtosecond Lasers, in: "Laser Ablation and its Applications", Phipps, Claude (Ed.) Springer Series in Optical Science 2006

A. Ovsianikov and B.N. Chichkov, Two-photon polymerization - High Resolution 3D Laser Technology and its Applications, in: "Nanoelectronics and Photonics", From Atoms to Materials, Devices, and Architectures, Korkin, Anatoli; Rosei, Federico (Eds.), Springer Series in Nanostructure Science and Technology 2008

A. Ovsianikov and B.N. Chichkov, Three-dimensional Microfabrication by Two-photon Polymerization Technique, in: Computer-Aided Tissue Engineering, Liebschner, Michael; Sun, Wei (Eds.), Springer (*in production*)

Invited Talks:

A. Ovsianikov, A. Doraiswamy, R. J. Narayan, B. N. Chichkov, Rapid prototyping of ossicular replacement prostheses. In: 5th International Conference on Photo-Excited Processes and Applications, 3.-7. September 2006, Charlottesville, Virginia USA (2007).

A. Ovsianikov, A. Ostendorf, and B. N. Chichkov, 3-D Photofabrication by Femtosecond Laser Pulses and Its Applications in Photonics and Biomedicine, CLEO/QELS and PhAST 2007, May 6-11, Baltimore USA (2007).

Other Conferences and Proceedings:

A. Ovsianikov, J. Serbin, C. Fallnich, A. Ostendorf, B. N. Chichkov, Three-dimensional micro- and nano-fabrication of photo-sensitive materials by two-photon polymerization with femtosecond laser pulses, In: 23rd International Congress on Applications of Lasers & Electro-Optics - ICALEO, 4.-7. Oktober, San Francisco. S. M105, (2005).

A. Ovsianikov, B. N. Chichkov, "Two-photon polymerization technique for bio-applications" In: Manufacturing Engineering and Materials Handling, ASME International Mechanical Engineering Congress and Exposition, Part A, 5.-11. November 2005, Orlando. P. 105-108 (2005).

A. Ovsianikov, S. Passinger, C. Reinhardt, and B.N. Chichkov, Exploring Nanostructuring Properties of Diverse Photosensitive Materials by Two-Photon Polymerization Technique, COLA 2005, The 8th International Conference on Laser Ablation, Sept. 2005, Banff Canada (2005).

- B. N. Chichkov, E. Fadeeva, J. Koch, A. Ostendorf, A. Ovsianikov, S. Passinger, and C. Reinhardt, Femtosecond laser lithography and applications, Proc. SPIE Vol. 6106, "Photon Processing in Microelectronics and Photonics V", San Jose, (2006).
- B. N. Chichkov, J. Koch, A. Ovsianikov, S. Passinger, C. Reinhardt, and J. Serbin, Direct-Write Micro- and Nanostructuring with Femtosecond Lasers, Mater. Res. Soc. Symp. Proc. Vol. 850, MM2.5.1 (2005).
- A. Doraiswamy, T. Patz, R. Narayan, B.N. Chichkov, A. Ovsianikov, R. Houbertz, R. Modi, R. Auyeung, D.B. Chrisey. Biocompatibility of CAD/CAM ORMOCER polymer scaffold structures, Mater. Res. Soc. Symp. Proc. Vol. 845, AA2.4.1 (2005).
- A. Ovsianikov, A. Doraiswamy, R. Narayan, and B. N. Chichkov, Study of Polymeric Microneedle Arrays for Drug Delivery, Mater. Res. Soc. Symp. Proc. (2006).
- F. C. Wippermann, D. Radtke, U. Zeitner, J. W. Duparre, A. Tunnermann, M. Amberg, S. Sinzinger, C. Reinhardt, A. Ovsianikov, and B. N. Chichkov, Fabrication technologies for chirped refractive microlens arrays, Proc. SPIE Vol. 6288, "Current Developments in lens design and optical engineering VII", San Diego, 14-15. 8 (2006).
- B. N. Chichkov, E. Fadeeva, J. Koch, A. Ostendorf, A. Ovsianikov, S. Passinger, and C. Reinhardt, Femtosecond laser lithography and applications, Proc. SPIE Int. Soc. Opt. Eng. 6106, 610612 (2006)
- A. Ovsianikov, A. Ostendorf, B. N. Chichkov, Three-dimensional Photofabrication with femtosecond lasers for applications in photonics and biomedicine. In: International Conference on Photo-Excited Processes and Applications, 3.–7. September 2006, Charlottesville, Virginia USA (2006).
- A. Ovsianikov, A. Doraiswamy, R. Narayan, and B. N. Chichkov, Two-photon polymerization for fabrication of biomedical devices, Proc. SPIE Int. Soc. Opt. Eng. 6465, 64650O (2007).
- C. Reinhardt, A. Ovsianikov, S. Passinger, and B. N. Chichkov, Fabrication of micromechanical and microoptical systems by two-photon polymerization, Proc. SPIE Int. Soc. Opt. Eng. 6466, 64660M (2007).
- S. Passinger, R. Kiyam, A. Ovsianikov, C. Reinhardt, and B. N. Chichkov, 3D nanomanufacturing with femtosecond lasers and applications, Proc. SPIE Int. Soc. Opt. Eng. 6591, 659104 (2007).
- A. Ovsianikov, A. Doraiswamy, R. J. Narayan, B. N. Chichkov, Rapid prototyping of ossicular replacement prostheses. In: 5th International Conference on Photo-Excited Processes and Applications, 3.–7. September 2006, Charlottesville, Virginia USA (2007).

Curriculum Vitae

Name: **Aleksandr
Ovsianikov**

Date of Birth: October 12, 1978

Place of Birth: Klaipeda, Lithuania

Nationality: Lithuanian

Address: Nanotechnology Department
Laser Zentrum Hannover e.V. (LZH)
Hollerithallee 8
D-30419 Hannover
Phone: 0511/27 88 -233
Fax: 0511/27 88 -100
E-Mail: A.Ovsianikov@lzh.de

Education:

1996 – 2000 Student at the Vilnius University
(Vilnius, Lithuania), graduated with
Bachelor of Science Degree

2001 – 2003 Student at the University of Hannover
(Hannover, Germany), graduated with
Master of Science Degree

2003 – 2008. PhD student at the Laser Zentrum
Hannover e.V.
Topic: “Investigation of Two-Photon
Polymerization Technique for
Applications in Photonics and
Biomedicine”

Academic Appointments:

10/2000 -06/2001 Scientific researcher at the Development
Department at the Laser Zentrum
Hannover e.V.

01/2004 – Scientific researcher at the
Nanotechnology Department at the Laser
Zentrum Hannover e.V.

herzlichen Dank

Thank you

Спасибо

謝謝

Merci

ありがとう

Ačiū

This last page in my thesis is dedicated to people who have made this work possible.

First of all I would like to thank my parents and my sister for backing me throughout the years of my studies. My wife Lina and daughter Urtė, who have been a great inspiration and encouragement to me during the preparation of this thesis. Many friends outside LZH whom I had to almost completely “disconnect” from during the write up period.

I would also like to express my gratitude to Prof Welling for giving me an opportunity to conduct my research project at the LZH. Prof Boris Chichkov for supervising my work, providing freedom of research, and constant flow of new “mind-blowing” ideas. I acknowledge the financial support received from “Robert-Bosch foundation” and “Freundeskreis der Leibniz Universität Hannover”.

I am grateful to Prof Ertmer for taking on the responsibilities of a referee despite his extremely occupied schedule and to Prof Michel for finding time to head the defence committee during a very busy late December season.

My special thanks goes to Roman Kiyani for mentoring my scientific endeavours, reading through drafts of the thesis and making very valuable suggestions. Andrej Stepanov for his helpful remarks during the final preparation stage.

The work on photonic crystals would be incomplete without the analysis of fabricated structures. I appreciate the possibility to use the analytical equipment at Prof Wegeners group in Karlsruhe. Especially I am grateful to Martin Hermatschweiler for his assistance and valuable discussions.

Herr Gebauer I would like to thank for his readiness and for many gigabytes of high quality images, without them my work would be hard to evaluate.

Through the years I have really enjoyed the multi-disciplinary research environment of the Nanotechnology Department at the LZH. I sincerely thank our present “femtosecond laser technologies” group - Jürgen, Martin, Lothar, Arsenij, Xiao, Kotaro, Sabrina, and Elena for their attitude and unconditional help. In the past years it was a great fun to work together with Nir, Ivan, Jacques, Mangirdas, Vytautas, Arune, Jenny, Regina, and Shaun. I have “broadened my horizons” a great deal while working together with our international collaborators Prof Roger Narayan, Dr Anand Doraiswamy, Dr Oliver Odunka, Dr Peter Mente, Sebastian Meghezi, Dr Maria Farsari, Dr Maria Vamvakaki, and Dr Mohamed Oubaha.

